VILNIUS UNIVERSITY
CENTER FOR PHYSICAL SCIENCES AND TECHNOLOGY

Laurynas
DAGYS

NMR cross-polarization dynamics in structural manifolds of functional materials

DOCTORAL DISSERTATION

Natural sciences,
Physics N 002

VILNIUS 2019

This dissertation was written between 2017 and 2019 in Vilnius University The research was supported by Research Council of Lithuania.

Academic supervisor:
Prof. Habil. Dr. Vytautas Balevičius (Vilnius University, Physical science, Physics 02P)

This doctoral dissertation will be defended in a public meeting of the Dissertation Defence Panel:
Chairman – **Prof. habil. dr. Leonas Valkūnas** (Vilnius University, Natural sciences, Physics – N 002).
Members: (members listed in alphabetical order of surnames)
Prof. dr. Darius Abramavičius (Vilnius University, Natural sciences, Physics – N 002).
Dr. Audrius Alkauskas (Center for Physical Sciences and Technology, Natural sciences, Physics – N 002).
Dr. Alytis Gruodis (Vilnius University, Natural sciences, Physics – N 002).
Prof. Dr. Janez Plavec (Slovenian NMR centre, Natural sciences, Chemistry – N 003)

The dissertation shall be defended at a public meeting of the Dissertation Defence Panel at 14 (hour)/ on 16 September 2019 in Room/meeting room A101 of the Centre for Physical Sciences and Technology

Address: Saulėtekio av. 3, LT-10257 Vilnius, Lithuania
Tel. +370 5 264 8884; e-mail office@ftmc.lt.

The text of this dissertation can be accessed at the libraries of Vilnius University and Center for Physical Sciences and Technology as well as on the website of Vilnius University: www.vu.lt/lt/naujienos/ivykiu-kalendorius

VILNIAUS UNIVERSITETAS
NACIONALINIS FIZINIŲ IR TECHNOLOGINIŲ IR MOKSLO CENTRAS

Laurynas
DAGYS

BMR kryžminės poliarizacijos dinamika funkcinių medžiagų struktūrinėje įvairovėje

DAKTARO DISERTACIJA

Gamtos mokslai,
fizika N 002

VILNIUS 2019

Disertacija rengta 2017– 2019 metais Vilniaus universitete.
Mokslinius tyrimus rėmė Lietuvos mokslo taryba.

Mokslinis vadovas:
prof. habil. dr. Vytautas Balevičius (Vilniaus universitetas, gamtos mokslai, fizika – N 002).

Gynimo taryba:
Pirmininkas – **prof. dr. habil. Leonas Valkūnas** (Vilniaus universitetas, gamtos mokslai, fizika – N 002).
Nariai:
prof. dr. Darius Abramavičius (Vilniaus universitetas, gamtos mokslai, fizika – N 002),
dr. Audrius Alkauskas (Fizinių ir Technologijos Mokslų Centras, gamtos mokslai, fizika – N 002),
dr. Alytis Gruodis (Vilniaus universitetas, , gamtos mokslai, fizika – N 002),
prof. dr. Janez Plavec (Slovėnijos BMR centras, gamtos mokslai, chemija – N 003).

Disertacija ginama viešame Gynimo tarybos posėdyje 2019 m. rugsėjo mėn. 16 d. 14 val. Nacionalinio Fizinių ir Technologijos mokslų centro A101 posėdžių salėje / auditorijoje. Adresas: Saulėtekio al. 3, LT-10257 Vilnius, Lietuva, tel. +370 5 264 8884; el. Paštas: office@ftmc.lt.

Disertaciją galima peržiūrėti Vilniaus universiteto, Fizinių ir technologijos mokslų centro bibliotekose ir VU interneto svetainėje adresu: https://www.vu.lt/naujienos/ivykiu-kalendorius

ABBREVIATIONS

Amino acids:
Ala – alanine;
Arg – arginine;
Asn – asparagine;
Cys – cysteine;
Gln – glutamine;
Glu – glutamic acid;
Gly – glycine;
His – histidine;
Ile – isoleucine;
Phe – phenylalanine;
Pro – proline;
Ser – serine;
Thr – threonine;
Tyr – tyrosine;
Val – valine;

ACP – amorphous clustered phosphate phase (CaHA);
ADP – ammonium dihydrogen phosphate;
CaHA – calcium hydroxyapatite;
CaP – calcium phosphate;
CP – cross-polarization;
CSA – chemical shift anisotropy;
DD – direct dipolar (coupling);
DFT – density functional theory;
FT – Fourier transform;
FTIR – Fourier transformed infrared (spectroscopy);
FWHM – full width at half maximum;
GFG – Glycine-Phenylalanine-Glycine (tripeptide);
GGG – Glycine-Glycine-Glycine (tripeptide);
GPG – Glycine-Proline-Glycine (tripeptide)
HETCOR – heteronuclear correlation (spectroscopy);
HH – Hartmann-Hahn;
LAB – laboratory (frame);
MAS – magic angle spinning;
NMR – nuclear magnetic resonance;
PAS – principal axis system (frame);

pHEMA – poly-(hydroxyethyl methacrylate);
pVPA – poly-(vinyl phosphonic acid);
RAFT – reversible addition-fragmentation chain-transfer;
REDOR – rotational-echo double-resonance (NMR)
RF – radio-frequency;
RTIL – room temperature ionic liquids;
SAXS – shallow angle X-ray spectroscopy;
SEM – scanning electron microscopy;
TEM – transmission electron microscopy;
XRD – X-ray diffraction (spectroscopy);

CONTENT

1. INTRODUCTION

Material research can be considered as one of the most important aspects of the functional material development. Functional materials exhibit vast distribution of applications: some of the best known applications are found in medicine, pharmacy, chemical engineering, nanotechnology, etc[1–4]. Generally, functional materials can be characterised as any material which possess native properties and functions of their own and these intrinsic properties only can be only accessed with the help of characterization tools. The rapid advance in modern synthesis and chemical engineering demands constant improvement of various characterization techniques and hence the significant part of these methods is crystallography.

Crystallography, in essence, investigates structure of matter which leads to emanating physical and chemical properties[5]. Typically, structure in solids is determined by crystal packing, order and atomic distances. Diffraction based techniques where ultra-short wavelengths are achieved with electrons or neutrons are far the most convenient tools[6,7]. However, method like electron microscopy have fundamental restrictions thus these methods are not universal. Restrictions are typically met in absence of structural long-range order (amorphous, porous media) or due to a small cross-section of events regarding light elements like hydrogen[8,9]. Moreover, if the composition of material is at the interest, spectroscopic techniques take the major advantage[10–12] and even some of them, like infrared spectroscopy are sensitive to the organisation and packing as well[10,13,14]. This means that by coupling several tools together one can consistently comprehend the overall structure and properties in a material.

Nuclear magnetic resonance (NMR) is possibly one of the most versatile spectroscopic methods. It can investigate any state of matter and can be used to determine both composition and structure. Namely, structural analysis in NMR is related to dipolar coupling of two spins which is inversely proportional to distance between them. Heteronuclear correlation, magic angle spinning, recoupling and cross-polarization (CP) techniques are the frontier experiments that are based on this interaction[8,9,15]. However, especially in solid-state, NMR unmistakably faces some obstacles that require usage of advanced experiments as well as user experience. Despite of that, the correct experimental approaches grants with complementary crystallographic information that led to a field now frequently called NMR crystallography[7,16,17]. The correct way of using CP as a crystallographic tool is the precise processing of the kinetics that contain complex dynamical features.

Many challenges can be met searching for the correct analytical description concerning in the vast diversity of structures. As quantum mechanical calculations cannot be done for a large number of particles, some basic CP models were proposed in the seventh decade to set the basic foundation to understand the complex nature of cross-polarization[18,19]. Unfortunately, these models are only good approximations for few types of structures and cannot be ubiquitous. Plenty of incorrectly performed variable contact time CP experiments are present which in many cases leads to doubtful conclusions[20]. Thus, the insightful characterization of cross-polarization in numerous structures would result in better comprehension and to improved modelling. Finally, advanced processing routines would allow to uncover more hidden variables in materials fulfilling the constant demand of complementary techniques in material research.

1.1 Goals and tasks of the work

To cope with previously mentioned challenges regarding different solid-state media, the goal of this work has been set – to develop the best approaches of CP processing through exploration of different functional materials. The originating tasks to achieve this goal are the following:

1. To employ one-dimensional ^{1}H and ^{31}P NMR techniques to characterize complex structure of calcium hydroxyapatite.
2. To apply cross-polarization method and its dynamical models for the same study.
3. To compare the accuracy of cross-polarization modelling with well exploited crystallography techniques.
4. To translate methodology to other spin systems met in organic materials.
5. To find appropriate CP models for the whole dynamical range as well as throughout a large set of structures.

1.2 Statements of the doctoral thesis

1. Composition and structural organisation in complex materials can be attained with the use of ^{1}H and ^{31}P NMR coupled with magic angle spinning.
2. Macroscopic parameters of cross-polarization dynamics can by fitted using generic CP models whereas fine features of structure can be extracted by processing initial coherent part of CP kinetics.

3. Inclusion of angularly averaged dipolar coupling using reduced Fourier-Bessel transform lead to purely distance-depending dipolar coupling distribution.
4. Cross-polarization in weakly and strongly coupled system possess significant differences and thus it must be assessed in modelling.
5. Thermal equilibration driven by the spin diffusion in abundant spin sub-system strongly affects the cross-polarization dynamics between remote spin pairs.

1.3 Scientific novelty of the work

1. Assumptions made in this work allowed to bypass the explicit Fourier–Bessel transform which allowed to include angular averaging of dipolar coupling to retrieve purely distant-depending distribution of interacting spins.
2. Developed models of CP kinetics were able to analytically describe behaviour within the whole observed dynamic range in the large variety of structures.
3. The increase of spin diffusion rate with the proton density in a large set of amino acids was observed for the first time.
4. Incorporation of apodization during processing significantly enhanced the signal-to-noise ratio of dipolar coupling spectra which revealed coupling constant of weakly coupled systems.
5. Additional assumptions regarding spin diffusion in the abundant spin bath served with perfect non-linear fitting of cross-polarization kinetics of remote spins which provided with a new way to probe fractal dimensions of structures.

1.4 Contribution of the author

The synthesis of calcium hydroxyapatites, polymer hydrogel as well as SEM and XRD measurements where done in the Chemistry department of Vilnius University. The syntheses of tripeptides were performed in Technical University of Darmstadt. An included FTIR spectra were collected by colleagues in Institute of Chemical Physics at Vilnius University. All DFT calculation present in the work and in corresponding publications are done by dr. Kęstutis Aidas. All of the NMR experimental work was done by the author with initial supervision of dr. Vytautas Klimavičius. Processing, analysis, mathematical derivations were done both independently and with a close partnership between supervisors and the author. All preparations for

publications have been the result of fluent teamwork between co-authors. The author underlines that the present work partially overlaps with the dissertation of dr. V. Klimavičius as the ideas were those shared within the whole group. However, this dissertation can be considered as the analytical extension of the previous work towards new solids.

2. OVERVIEW

2.1 Functional materials

2.1.1 Calcium hydroxyapatite

Calcium phosphate compounds is among the most used functional materials in modern medicine[21]. Calcium phosphate (CaP) is the common name of a family of minerals containing calcium cations (Ca^{2+}) together with orthophosphate (PO_3^{4-}), metaphosphate (PO_3^-), or pyrophosphate ($P_2O_4^{7-}$) anions, and sometimes hydrogen (H^+) or hydroxide (OH^-) ions. Calcium phosphates with a Ca/P atomic ratio between 1.5 and 1.67 are called apatites (e.g., hydroxyapatite or fluorapatite)[22]. Calcium hydroxyapatites can form bioactive glasses that exhibit high bioactivity and biocompatibility[23]. Several ceramic materials have been clinically applied as well. Among them, ZrO_2 and Al_2O_3 exhibit high mechanical strength and good biocompatibility but, like metals, belong to bioinert materials.

Calcium phosphates in mineral form are found in the hard tissue like bone, dentin, enamel. The mineralized tissues of the human body have long been of great scientific interest, not just because of their biological importance, but because mimicking their mechanical properties in synthetic materials could potentially provide advanced functional materials which combine, as bone tissue does, excellent strength, flexibility, resistivity, and other desirable macroscopic features[24].

The specific structural and morphological properties of CaHAs are highly sensitive to the changes in chemical composition and processing conditions[25–27]. Due to the nanocrystalline nature, various diffraction techniques have not yet given much information on the fine structural details related to apatite nanocrystals. That is because assemblies of nanoparticles give only broad diffraction patterns, similar to ones from an amorphous material[28]. However, solid-state NMR could be effective and complementary solution to this problem as it is not limited by the long-range order.

2.1.2 Ammonium dihydrogen phosphate

Ammonium dihydrogen phosphate (commonly designated as ADP) is completely different phosphate than CaHA. It is, however, technologically important material because of its unique piezoelectric, ferroelectric, dielectric, and nonlinear optical properties[29]. The ADP crystal is widely used in electro-optical modulators and acousto-optical devices[30]. Because of the complex

variety of hydrogen bonding (three centred or bifurcated bonds) ADP is an interesting system for fundamental studies of this type of interactions in crystals[31]. The crystallographic structure of ADP has been well examined in numerous X-ray (XRD) and neutron diffraction (ND) experiments[32,33]. Nevertheless, characterization of proton network is a serious challenge even for these well exploited techniques. Furthermore, the spatial contact to light atoms like hydrogen can be only detected in single crystals using ND method. Thus, the possibility to offer another crystallographic tool like NMR is the main drive why ADP was chosen as a model system for the present study in the first place.

2.1.3 Proteinogenic amino acids

Amino acids make up a family of the simplest chemical compounds. Amino acids that are naturally incorporated into proteins are called proteinogenic amino acids. Generally, there are twenty-two proteinogenic amino acids. The question why exactly this number of amino acids have been selected during evolution is being tackled even in the present day. Based on computer simulations the 20 standard amino acids represent a largely global optimum, when their relevant physico-chemical properties were compared with those of a computationally generated compound library containing 1913 alternative amino acids[34,35]. In principle, all amino acids can be incorporated into (possibly synthetic) peptides or proteins unless special chemical substructures prevent this[35].

Amino acids display remarkable metabolic and regulatory versatility. They serve as essential precursors for the synthesis of a variety of molecules with enormous importance, and also regulate key metabolic pathways and processes that are vital to the health, development, reproduction, and homeostasis of organisms[36]. Probably the most common amino acids in organisms – glycine and alanine have their own key features.

Glycine (Gly) is the simplest amino acid and only non-chiral one (excluding dehydrogenated acids). Due to the extremely short side chain it is less appropriate for helices of peptides but is well suited for turns and for example, is essential constituent of the collagen helix. Besides being incorporated into proteins, glycine is also an inhibitory neurotransmitter in the central nervous system[20,37]. Whilst glycine is, moreover, involved in oxygen production in biological systems, alanine (Ala) regulates net glucose production[36,38]. In addition to these functions, glycine and alanine can be considered as the main building blocks in proteins.

In this work attention will be focused on Gly and Ala, but other results of different proteinogenic amino acids will be present as well. Due to a quite simple structure, proteinogenic amino acids are well studied but like ADP first can serve as a good model system for further insights on spin dynamics acting in organic solids. These insights, especially regarding different chemical groups could reveal the link of behaviour with the function.

2.1.4 Peptides

Peptides are composite molecules of amino acids. Normally being oligomers or polymers, they can consist of only two or three amino acids as well. Such peptides are called bi- or tri-peptides, respectively. Peptides stand out for their chemical diversity, low impact on the environment, and ability to convey biological "messages" in sequences as short as three amino acids[39]. Many neurotransmitters, neuromodulators and hormones are peptides which interact with receptors and effect biological processes and thus playing an important role in the living organisms[40,41].

Another interesting feature of some peptides is the ability to self-assemble. This way they have a potential to be drug carriers in a variety of stable nanostructures, such as rods, tubes, nano-vesicles etc[42,43]. Moreover, their applications can be also extended to tissue engineering, biomimicry, cancer cell detection, and even vaccine adjuvants to stimulate the immune response[41, refs therein].

However, there are several restrictions regarding these applications. Studies have shown that bioactive peptides often display poor bioavailability and can be easily degraded by peptidases[38,44]. Furthermore, peptides yield high flexibility which decrease binding affinity, for example, of the drug for its receptor. Thus, solutions to control rigidity require a set of tools to tackle these features. Rigidity or freedom of motion is an element in NMR spectroscopy that is known to have a clear connection with motional averaging effects. Therefore, the reason why a few tripeptides were tested in this work was to observe a well-resolved effect of mobility throughout the molecular structure which then defines the ordering of these compounds.

2.1.5 Polymer hydrogels

Polymer hydrogels yield many potential mechanical and chemical properties which led to progresses in drug delivery, cancer treatment, biotechnology and even orthopaedics when coupled with the use of CaHA. Nanohydrogels are considered as prospective members of smart polymers.

The main property of these compounds is to absorb water and/or other biological fluids more than their weights, while remaining insoluble[45–47]. In general, polymer hydrogels are made of cross-linked polymer networks having many hydrogen-bonding partners which allows them to be swollen with water.

Furthermore, the possibility to form self-assembled and supramolecular morphologies makes organic polymers a desirable building blocks for the design of water based gels[48,49]. However, the present interest demanded the development of a number of controlled polymerization techniques, in particular those based on radical chemistry such as reversible addition-fragmentation chain-transfer (RAFT) polymerization[50,51]. In this work this technique was using to synthesize a polymer based on methacrylate group. The methacrylate group is commonly used due to its ease of a "grafting through" synthesis, commercial availability, and reactivity[52]. Moreover, materials based on amphiphilic block copolymers generally exhibit a unique behaviour stemming from hybrid properties like biocompatibility and elasticity. As these polymers are water insoluble, large amounts of water can be adsorbed into a matrix with an equilibrium water content being almost half of weight. Such polymers as polymeric gels, thin films and solid materials are applied in regenerative medicine and other emerging technologies[53, refs therein].

It is not a surprise that polymers usually have freedom of motion as well as they can assemble in various of ways. Hence, parameters like orientational order, rigidity may be used to describe polymer systems. For example, it has been observed that rigidity is of paramount importance since molecular mobility affects the crystal arrangement and packing, hence affects the overall organization[54]. Similar as for peptides, one of the arguments why polymer hydrogel was investigated is the expected higher mobility in soft material compared to typical organic compounds as well the interesting hydrogen-bonding network within the molecule. More importantly, the research of soft matter like polymers would fulfil the aim to investigate cross-polarization in a broad variety of matter providing with a complete overview of spin dynamics.

2.1.6 Ionic liquids

Typically, inorganic salts yield very high melting temperature, minimizing the number of possible chemical processing routines. However, salts having melting point at room temperature or even below form a new type of liquids called room temperature ionic liquids (RTILs)[55]. Ionic liquids make them interesting as potential solvents for the following simple and yet unique

physical properties. They are good solvents even in unusual combination of reagents, they have the potential to be highly polar yet noncoordinating solvents, they are immiscible with a number of organic solvents and they are non-volatile[56]. Such variety of properties favour the applications in diverse fields, such as synthesis, catalysis, biocatalysis, separation technology, electrochemistry, analytical chemistry, and nanotechnology[57]. RTILs can be considered as one of the most successful breakthroughs in the field of "smart" materials and multifunctional compositions. Materials are classified as being "smart" if they possess an intrinsic ability to sense and definitely to respond in a predictable way to various external stimuli[58,59].

Generally, RTILs consist of a large, unsymmetrical ion and relatively small, symmetrical halide anions. Despite the larger BF_4^- anion, it forms RTILs with imidazolium and pyridinium cations. The unique variability of the ions often allows the properties of interest to be imparted[60]. Various trials to introduce them in practical applications, such as batteries, capacitors, and electrochemical solar cells have been made as well as to have a fundamental understanding of these ionic liquids[61,62]. However, fundamental knowledge of the intrinsic properties of the RTILs are still lacking making them compelling objects in material research.

2.2 Common characterization techniques

Advances in functional material science demands for a certain set of characterization tools that determine their intrinsic properties. If these properties arise from the structure, then crystallographic techniques are applied. Properties of some materials, say, to apatites related bioglasses can strongly depend on the crystallinity and ordering. This information can be accessed employing techniques like X-ray diffraction (XRD), infrared (IR) spectroscopy, neutron scattering (NS), neutron diffraction (ND), scanning electron microscopy (SEM) and transmission electron microscopy (TEM)[63–68]. Diffraction based techniques, however, are particularly outstanding in determining lattice parameters, position of the atoms and packing of the molecules. For example, using small angle X-ray spectroscopy (SAXS) one can determine structures with resolution up to 9 nm[68]. Furthermore, the same or even better resolution (< 0.5 nm) can be achieved incorporating SEM and TEM techniques. Moreover, microscopy allows to visually inspect morphology and organisation which is especially useful investigating nano- or sub-nano structure materials and their size distribution within the sample. Then, if chemical composition is at the importance, spectroscopic techniques such as FTIR, XRD are employed. Both methods combined grants with an

effective tool to estimate the degree of crystallinity, content of doped ions or to sense surface effects[11,69]. However, in the context of porous materials (polymers, silica, etc.) may lack order for XRD as well as for FTIR may lack sensitivity at which case nitrogen adsorbtion/desorbtion can be incorporated. Measuring isotherms of the process allows to estimate pore sizes in the bulk and on the surface providing with the missing information[63–65,70]. Thus, coupling methods together allows to determine functional materials quite efficiently.

Since all experiments have their natural limits, let us underline few obstacles met in the latter examples. Firstly, most of the experiments depend on cross-section of events. For instance, diffraction and the resulting pattern strongly depends on the electron density. Therefore, mobile and light elements like hydrogen, lithium do not diffract waves well and even if they do, their diffraction pattern is masked by the presence of heavier atoms nearby. Despite that, shorter wavelengths (say neutron waves) are capable to diffract well even from hydrogen but it requires a coherent source of neutron which raises the cost. Additionally, diffraction pattern loses resolution drastically when is still the long-range order in the structure is low. Hence, in amorphous material it is impossible to detect light atoms using XRD and ND[8]. Moreover, element like hydrogen is not only light but plays a crucial role in chemistry due to hydrogen bonding. This type of bonding usually occurs in groups where hydrogen is bound to O, F, P, N or S elements. If it is strong, delocalization of the hydrogen ion significantly broadens the spatial distribution making it even more difficult to pin. Regarding infrared spectrometry, delocalisation changes vibrational frequency of the bond as well, meaning that FTIR is affected by H-bond and, therefore, can be used to investigate H-networks[11,71,72]. In the typical IR absorption spectra hydrogen bonding broadens the spectral lines consequently diminishing the resolution and thus structural analysis is not straightforward.

NMR spectroscopy in some degree can cope with previously mentioned limitations. Firstly, hydrogen nucleus is known to have the highest gyromagnetic ratio which makes it the most sensitive nucleus. Nonetheless, hydrogen does come with many broadening effects like in IR regime, but the typical resolution is better[73,74]. Generally, all nuclei with a spin can induce a signal but there are significant differences in complexity. The signal yield depends on the gyromagnetic ratio and the natural abundances of an NMR active isotope. In the matter of this work, compounds are made up from elements which all have NMR active isotopes. However only few of them are picked for investigation and reasons are the following. Since NMR signals are inheritably weak it is normal to start with the most sensitive nucleus. That is

why there are so many works related to phosphates and organics[75,76,85,77–84] that incorporate ^{1}H, ^{31}P NMR spectroscopy. And although ^{13}C, ^{15}N are not particularly sensitive isotopes they are crucial elements in peptide and protein research too[86–88] but the then signal gain has to be artificially increased by isotope labelling or using hyperpolarization methods. Secondly, to avoid overly complicated modelling, limitation of spin numbers greater than ½ has to be introduced as additional properties like quadrupolar coupling would act. Furthermore, even if such unwanted effects are typically averaged by motion in isotropic liquids, translational restrictions in solid-state makes spin dynamics to depend on multiple of things. A few examples regarding solid-state problems will be given further in the text.

Regardless low sensitivity, NMR is still one of the most versatile techniques in research as there are numerous feasible approaches. Therefore, the concept of NMR crystallography has emerged almost a decade ago, with the idea either to perform, in favourable cases, the structure determination from NMR data only, or, most often, to include NMR data in the structure evaluation process to increase success of the search, and the a accuracy of the structure[9]. Among a broad variety of characterization techniques solid-state NMR spectroscopy applying magic-angle spinning (MAS), cross-polarization (CP), heteronuclear correlation (HETCOR), etc., can be considered as the method that provides probably the most insightful view of the bulk- and surface structures as well as dynamics on the molecular and mesoscopic length scales[15,57,89–91].

Namely, CP is the main technique used in the present work. Cross-polarization mechanism rely and depend on a dipolar coupling between two interacting spins. Dipolar coupling, in its own depends on a distance ($\sim 1/r^3$), thus can be used to probe the structure. Unfortunately, plenty of incorrectly performed variable contact time CP experiments are present in the literature, like insufficient number of time domain points, non-proper processing exploiting oversimplified CP transfer models, which in many cases leads to doubtful conclusions[20]. Furthermore, when powdered materials are under investigation with MAS, one needs to include complex angular averaging which makes CP unappealing to use. This work will present developed routines to employ CP in a large variety of compounds.

3. SOLID STATE NMR SPECTROSCOPY

In this chapter a brief overview of the quantum mechanical description for understanding nuclear magnetic resonance will be presented. Only important steps will be included but more explicit details can be found in the referred literature.

3.1 Nuclear spin and magnetic resonance

Many experiments in NMR can be explained using entirely classical framework of electrodynamic. For example, consider the case where magnetic moment $\boldsymbol{M}$ is in a magnetic field $\boldsymbol{B}$, then it will experience a following torque:

$$\frac{\mathrm{d}\,\boldsymbol{M}(t)}{\mathrm{d}t} = \boldsymbol{M}(t) \times \boldsymbol{B}\,. \tag{3.1}$$

As a result, the vector $\boldsymbol{M}$ will precess around the acting magnetic field $\boldsymbol{B}$ and this process can be electrically picked up by the induction coil. At this particular point of view the role of spin couplings and chemical shift are slight reductions of an external magnetic field and consequently a change of the resonance frequencies. This can be considered as the origin of different resonant lines and their splitting.

On the other hand, in the most cases NMR phenomenon is better understood in quantum mechanical framework where spin system is expressed in terms of Hamiltonian. The resonances then can be envisaged as transitions between the eigenstates. In such case analogue for (3.1) equation is the famous Schrödinger equation:

$$\frac{\mathrm{d}}{\mathrm{d}t}\left|\psi_{spin}(t)\right\rangle \cong -\mathrm{i}\hbar\widehat{\mathcal{H}}_{spin}\left|\psi_{spin}(t)\right\rangle, \tag{3.2}$$

where ψ_{spin} is a spin state and $\widehat{\mathcal{H}}_{spin}$ is a corresponding Hamiltonian under which spins act. It contains terms that only depend on the directions of nuclear spin polarizations and this is only true if the rapid motions of electrons can be considered blurred out[92]. Generally, Hamiltonian contains information about spin interactions which further on can be divided into two parts – external and internal:

$$\widehat{\mathcal{H}}_{spin} = \widehat{\mathcal{H}}_{External} + \widehat{\mathcal{H}}_{Internal}\,; \tag{3.3}$$

$$\widehat{\mathcal{H}}_{External}(t) = -\sum_i^N \gamma_i B^0 \hat{I}_{i,z} + \widehat{\mathcal{H}}_{RF}(t)\,; \tag{3.4}$$

$$\widehat{\mathcal{H}}_{Internal} = \widehat{\mathcal{H}}_{DD} + \widehat{\mathcal{H}}_{CSA} + \widehat{\mathcal{H}}_{J} + \cdots. \tag{3.5}$$

The term “external” relate to controllable factors like external or radio-frequency (RF) magnetic fields. By convention strong external field is along z axis and hence only z projection of magnetic moment $\hat{\mu}_{i,z} = \gamma_i \hat{I}_{i,z}$ is incorporated in the first term in Eq. (3.4). Moreover, as one typically expects an ensemble of spins, the latter term must be summed over all spins. Now, the second term of (3.4) must be included when RF pulses are applied, say, during the experiment. It is worth mentioning, that RF pulses are typically perpendicular to external field of a magnet and thus contain I_x and I_y elements with additional cosine and sine functions regarding radio-frequency.

The internal part of Hamiltonian, however, consists elements that are out the experimental control like all interactions occurring between nuclear spins or between other surroundings. There are numerous possible spin interactions like dipolar coupling (DD), chemical shift anisotropy (CSA), indirect dipolar coupling also known as J-coupling (J) etc. Accordingly, they also have distinctive mathematical forms and some will be discussed in upcoming chapters.

The physical observable in NMR experiment is a transverse magnetization which induces the electrical signal. Thus, detectable state of a spin system is transverse angular momenta. Note, usually angular momentum operators $\hat{I}_x$ or $\hat{I}_y$ are termed as coherences that link different eigenstates in the Zeeman basis. This is the reason why in NMR jargon, the word “coherences” are used more commonly then “transverse magnetization”. Furthermore, in the rotating frame approximation, coherences also correspond to shift operator $\hat{I}_- = \hat{I}_x - \mathrm{i}\hat{I}_y$ meaning that coherences are transitions between two states when angular momentum of the system is increased by +1[93].

Now, consider an ensemble of *isolated spins*-1/2 where some of the spins might be parallel to magnetic field (also known as $|\alpha\rangle$ state) and other are anti-parallel ($|\beta\rangle$) but mostly it is a uniform distribution along every possible direction. Hence solving (3.2) equation for each of them is a completely inconvenient task. Therefore, in NMR a usual solution to such problem is to address an ensemble as a single entity using density operator formalism:

$$\hat{\rho} = \mathbb{N}^{-1}(|\psi_1\rangle\langle\psi_1| + |\psi_2\rangle\langle\psi_2| + \cdots) \equiv \overline{|\psi\rangle\langle\psi|} \tag{3.5}$$

which is the average over all spins in the whole ensemble. This way finding a angular momenta of interest is trivial. For example, if the polarization along x axis is at interest, then one can easily take a trace of the product between density and angular momentum operators[92]:

$$P_x \cong \mathbb{N}\,\mathrm{Tr}\{\hat{\rho}\hat{I}_x\} \tag{3.6}$$

On the other hand, since density operator is not a pure state anymore, then Hilbert space of vectors is no longer usable. The extension of Schrodinger equation (3.5) to Liouville space is known as Liouville-Neumann equation:

$$\frac{\mathrm{d}\hat{\rho}(t)}{\mathrm{d}t} = -\mathrm{i}[\hat{H}, \hat{\rho}(t)] + \hat{\hat{\Gamma}}(\hat{\rho}(t) - \hat{\rho}_{eq}) \tag{3.7}$$

Non-coherent part $\hat{\hat{\Gamma}}$ in the expression above is also commonly known as relaxation superoperator. If this equation is used in rotating frame or more importantly in doubly rotating frame, say, during cross-polarization experiment, $\hat{\hat{\Gamma}}$ can denote spin-diffusion superoperator. Such example will be present in section on cross-polarization.

To briefly emphasize on amenity in using (3.7), consider simple case of ensemble of single spins-1/2 that are oriented along strong magnetic field thus yielding angular momentum $\hat{I}_z$. As angular momentum operators share a cyclic permutation (3.8), the sudden transverse magnetic field B_1 would act upon the initial magnetization. From equation (3.9) solution follows that additional transverse field B_1 will then rotate magnetization around the its axis. Therefore, the 90° pulse corresponds to quarter rotation of initial angular momenta about active transverse field axis or to a pulse with duration $\tau^{90} = -1/4\gamma B_1$, where γ is gyromagnetic ratio and B_1 is the field strength.

$$[\hat{I}_x, \hat{I}_y] = \mathrm{i}\hat{I}_z \;\circlearrowleft \tag{3.8}$$

$$\frac{\mathrm{d}\hat{\rho}(t)}{\mathrm{d}t} = -\mathrm{i}[-\gamma B_1 \hat{I}_x, \hat{I}_z] = \gamma B_1 \hat{I}_y \longrightarrow$$

$$\longrightarrow \hat{\rho}(t) = \hat{I}_z \cos(\gamma B_1 t) - \hat{I}_y \sin(\gamma B_1 t) \tag{3.9}$$

Now, if the magnetization is already flipped by 90° NMR pulse, constant and strong magnetic field would continue acting, only this time angular momenta will precess around z axis instead with the corresponding frequency $\omega^0 = -\gamma B_0$. If then one would apply (3.6) and Fourier transformation, the result would be a single resonance peak at Larmor frequency $\omega^0 = -\gamma B^0$ (Fig. 3.1). As the same picture would result from classical point of view, it seems that quantum mechanical view is overly complicated. Nevertheless, one will find that classical electrodynamics are not capable to explain complex spin dynamics.

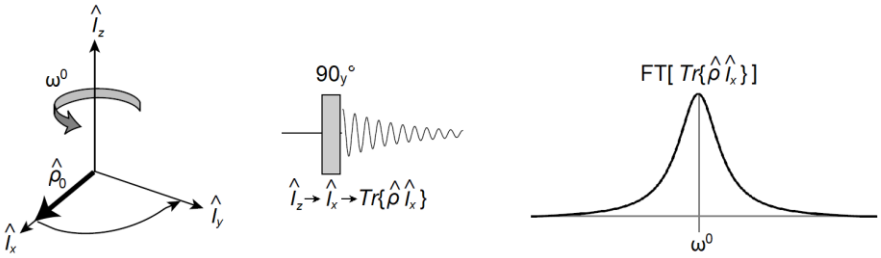

Figure 3.1. Rotation of the density operator (on the left), corresponding to induction signal (in the middle) and resonance peak (on the right). Line broadening was added for clarity. Adapted from Ref 92.

3.2 Direct dipolar coupling

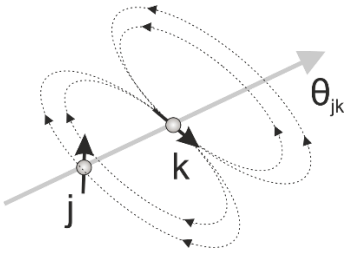

Figure 3.2. Two interacting nuclear dipoles. Exerted field lines are shown by dashed lines.

In the previous section "external" interactions which can be controlled (3.4) were illustrated. Namely, NMR employs a strong magnet and sequences of RF pulses which manipulate angular momenta of the spin system. However, what makes NMR interesting is variety of "internal" interactions that spin systems inherit. Direct dipolar (DD) coupling is perhaps the simplest interaction by nature but one of the strongest and most important. If two dipoles (imagine two bar magnet-like objects) are near to each other, exerted field lines of one dipole will affect local magnetic field for the other (Fig. 3.2). Consequently, resonance frequency of the second spin will slightly shift or in other words Hamiltonian for that spin will be perturbed. Direct dipolar interaction Hamiltonian has a following form[94]:

$$\widehat{\mathcal{H}}_{jk}^{DD} = -\frac{\mu_0}{4\pi}\frac{\gamma_j\gamma_k}{r_{jk}^3}\left(3\left(\hat{\boldsymbol{I}}_1\boldsymbol{e}_{jk}\right)\left(\hat{\boldsymbol{I}}_2\boldsymbol{e}_{jk}\right) - \hat{\boldsymbol{I}}_1\cdot\hat{\boldsymbol{I}}_2\right) \qquad (3.10)$$

where μ_0 is vacuum permeability constant, r_{jk} is the distance between two interacting spins and $\boldsymbol{e}_{\mathrm{jk}}$ is normal vector depicted in Fig. 3.2 as a grey line. Being directly linked to internuclear distance, dipolar interaction is a foundation for structural analysis in NMR spectroscopy.

The expression (3.10) is not typically expressed in Cartesian angular momentum operators because those are hard to work with, especially when it comes to describe the effect of rotations. Consecutively, spherical tensor representation is much more convenient[95]:

$$\widehat{\mathcal{H}}_{jk}^{DD} = b_{jk}\sqrt{24\pi/5}\ \sum_m (-1)^m\ Y_2^m T_2^{-m} \tag{3.11}$$

$$b_{jk} = -\frac{\mu_0}{4\pi}\frac{\gamma_j \gamma_k}{{r_{jk}}^3} \tag{3.12}$$

Term Y_2^m is a form of spherical harmonic and T_2^{-m} are products of spin operators. A complete table of the expressions of these terms can be found in referred literature. Favourably, in high magnetic field where Zeeman interaction is dominant, so-called secular approximation is used to omit terms that do not commute with a large Zeeman Hamiltonian, leaving only manifold $m = 0$. Thus, the expression for "secular" dipolar coupling Hamiltonian is the following:

$$\widehat{\mathcal{H}}_{jk}^{DD,secular} = b_{jk}\frac{3\cos^2\theta_{jk}-1}{2}\left(3\hat{I}_{1,z}\hat{I}_{2,z} - \hat{\boldsymbol{I}}_1 \cdot \hat{\boldsymbol{I}}_2\right) \tag{3.13}$$

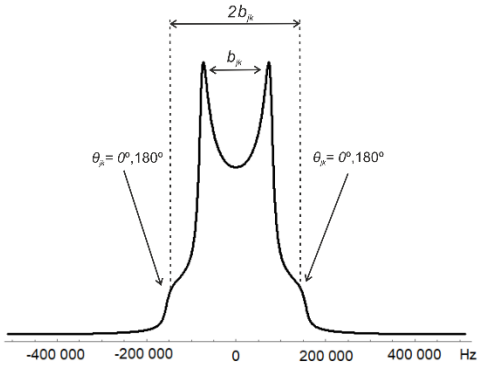

Figure 3.3. Simulated powder pattern of two coupled nuclei.

Note that Hamiltonian is now dependent on angle θ_{jk} between magnetic field and the spin pair. Henceforth, if the sample contains powder where small crystallites are randomly oriented, NMR spectrum forms so called Pake pattern (Fig. 3.3). Typically, this pattern can mask all other interaction in

NMR as the width of the pattern can be on the order of 200 kHz (see figure above). Remarkably, if spins are allowed to move like in isotropic liquids rapid motions average out (3.13) the angular part to zero allowing high resolution spectra to show up which is a great advantage of liquid state NMR spectroscopy. Nevertheless, in liquid state indirect dipolar coupling (coined as J-coupling) is present but the strength is in the order of hertz.

Now, a certain ambiguity can be found when tags like “strong coupling” or “weak coupling” are used. On contrary, in the framework of J-coupling strong coupling is assumed when coupling is equal or larger than chemical shift in which case direct dipolar would be almost always true. Therefore, since a clear convention for what strong heteronuclear coupling is does not exist, let us present convention that would be convenient for the present work.

The strongest interactions occur when nuclei are one bond away from each other. Thus, dipolar coupling value corresponding to the typical bond length will be denoted as “strong”. In similar fashion, spins will be weakly interacting if there are far apart. Therefore, “weak” interaction will correspond to spins roughly two bonds away. Obviously, threshold values will be different for different pairs of elements as they have different bond lengths as well as gyromagnetic ratios. Examples of H-P and H-C are depicted in figure 3.4 where strong and weak coupling regions are depicted as filled spaces.

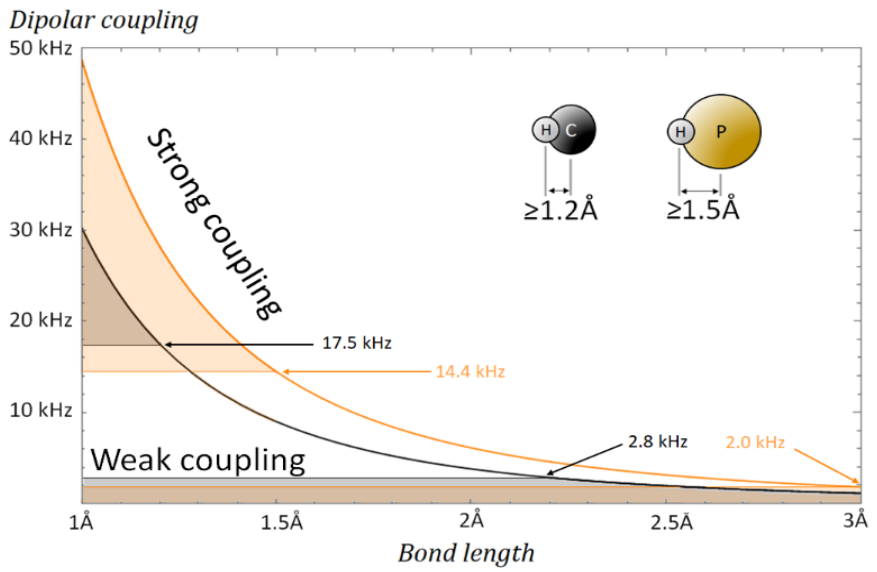

Figure 3.4. Dipolar coupling between ^{1}H-^{31}P (orange line) and ^{1}H-^{13}C (black line) with respect to distance between interacting nuclei. Filled areas illustrate regions of strong and weak coupling. Threshold values are given by arrows.

Merely, coupling will be termed as strong if the value is above 17.5 kHz for carbon-proton pair and 14.4 kHz for phosphorous-proton whereas if the value is lower than 2.8 kHz and 2.0 kHz for carbon and phosphorous, respectively, it will correspond to weak coupling. Values found between those two regions will be coined as intermediate dipolar coupling.

3.2 Chemical shift anisotropy (CSA)

The great advantages of NMR in liquid-state is spectral resolution. This is due to the fact, that molecules in liquid experience rapid tumbling and chaotic reorientations. As one shall see later, motional averaging can average out various interactions leaving only chemical shift. Chemical shift, generally, stems form electrons that cloud and shield magnetic field for the nuclei. The scale of shielding depends on the chemical group, chemical environment and therefore can be used to characterize molecules.

Naturally, electron shielding may not be constant in all orientations as in common example of the eddy currents in benzene ring which exerts opposing magnetic field in the middle but not from sides. For these reasons chemical shift (a unit of magnetic shielding) can be significantly anisotropic. Now, chemical tumbling in solid-state is mostly restricted introducing another strong interaction commonly met in solid-state NMR – chemical shift anisotropy (CSA). Despite being usually orders weaker than DD, CSA still considerably affects solid-state NMR spectra as well as other effects.

In a line with this work, ^{31}P isotope is mostly concerning but even ^{13}C has a considerable CSA if situated at carboxyl or aromatic group. Similarly, like dipolar coupling, CSA Hamiltonian has cartesian and spherical representations[94]:

$$\widehat{\mathcal{H}}_j^{CSA} = \gamma_j \hat{\boldsymbol{I}}_j \boldsymbol{\sigma}_j \boldsymbol{B} = \text{(Cartesian)} \qquad (3.14)$$
$$= \gamma_j \sum_{l=0,2} \sum_{m=-l}^{+l} (-1)^m T_l^m \sum_{m'} D^l_{m',-m} \rho_{lm'} \text{ (Spherical)}$$

Terms $D^l_{m',-m}$ and $\rho_{lm'}$ denote Wigner matrices and components of irreducible spherical tensor operator in principal axis system (PAS), respectively. Also note that $\boldsymbol{\sigma}_j$ is a tensor which in PAS simplifies to diagonal tensor only having σ_{xx} , $\sigma_{yy,}$ σ_{zz} components. Wigner matrices are then used to rotate PAS frame to laboratory (LAB) frame for a convenient analytical treatment as previously seen. Again, secular approximation allows to omit *m* = 0 terms substantially simplifying the equation. Finally, as Wigner matrices

have a convenient similarity to spherical harmonics which leads to the final Hamiltonian:

$$\widehat{\mathcal{H}}_j^{CSA,secular} = \gamma_j B_0 \hat{I}_z \left\{ \sigma_{iso} + \Delta \left[\frac{3\cos^2\theta - 1}{2} + \frac{1}{2}\eta \sin^2\theta \cos 2\beta \right] \right\} \quad (3.15)$$

where

$$\sigma_{iso} = (\sigma_{xx} + \sigma_{yy} + \sigma_{zz})\frac{1}{3} \quad (3.16)$$
$$\Delta = \sigma_{zz} - \sigma_{iso}$$
$$\eta = (\sigma_{xx} - \sigma_{yy})/\Delta$$

This time the so-called secular Hamiltonian depends on two angles if the chemical shift ellipsoid is asymmetric ($\eta \neq 0$). In the case of powder, again, crystallites and thus chemical shift ellipsoids can be oriented randomly, thus NMR spectrum will form pattern as in Fig. 3.5.

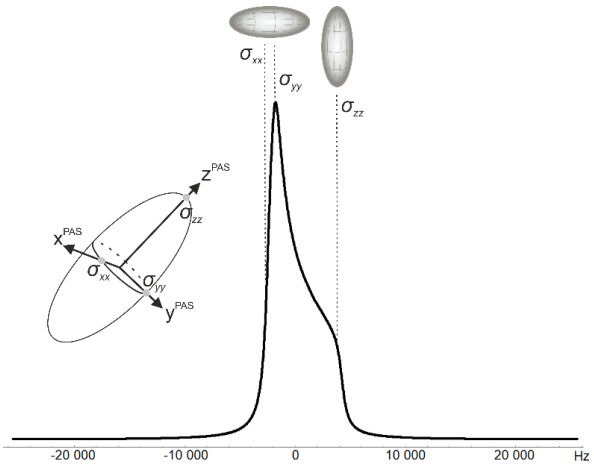

Figure 3.5. Simulated powder pattern of chemical shift anisotropy. Parameters were used those commonly found in literature of ^{31}P NMR. Chemical shift tensor presented for clarity.

Seemingly, NMR experiments in liquid-state are much more advantageous as in solid-state many interaction broadens spectral lines such that chemical shift values are hidden. To some extent it is true, however, then direct information of DD, CSA in liquids is completely lost. Only with use of solid-state NMR these interactions can be probed and, regarding this work, dipolar coupling is at interest as it contains pure spatial information of structure. The following section will present a way how to tackle problem of low resolution in solid-state yet still obtaining information of spin interactions.

3.3 High resolution in solid state. Magic Angle Spinning (MAS)

"*narrow is beautiful*" U. Haeberlen[94]

It was underlined in previous section that high resolution is the great advantage of liquid-state NMR. A great deal of resolution in solid-state NMR is lost because of present interactions like dipolar coupling, chemical shift anisotropy. Other interactions like quadrupolar, spin-rotation, J-coupling will not be discussed. As static powdered sample contain randomly oriented crystallites one would observe powder pattern in NMR spectra and that would mask fine details of chemical shift, hence high-resolution cannot be achieved. Regarding heteronuclear dipolar coupling, spins can be easily decoupled using strong RF pulses resonant to unwanted spin species but, unfortunately, interaction like homonuclear coupling or CSA cannot be decoupled that way. Furthermore, translational motion in solid-state is completely restricted, meaning that motional averaging will not average these interactions out. Note that when principal axis system is oriented at 54.74° with respect to magnetic field (see equations (3.13) or (3.15)) interaction Hamiltonians drastically reduce (or even vanish) due to a common dependency on $Y_2^0 = \sqrt{5/\pi 16}\,(3\cos^2\theta - 1)$ spherical harmonic. Such angle where these (typically) unwanted Hamiltonians get averaged is called as Magic Angle relating to a technique called Magic Angle Spinning (MAS).

Generally, MAS is an experiment where rotor containing powdered sample is spun at Magic Angle (Fig. 3.6). During MAS angle changes at the rate of rotational frequency making interaction ellipsoid as well as equations (3.13) and (3.15) time dependant. If the spinning rate is sufficiently large, time average of the Hamiltonian is reduced to its isotropic value. If interaction is stronger than MAS averaging (say $b_{jk} > \omega_{rot}$) then powder pattern splits into many spinning sidebands, roughly mimicking the powder pattern (Fig. 3.7). Conveniently, central line or isotropic value never changes its position meaning that it is trivial to obtain the chemical shift of one site and thus extremely high spinning speed are not necessary. Moreover, sidebands can be also used to fit the line-shape to acquire interaction parameters and can be more accurate than fitting static spectra. In unfortunate circumstances where many nuclear sites are present, spinning sidebands can complicate NMR spectra, hence normal experimental routine is to set MAS rate to the highest feasible value.

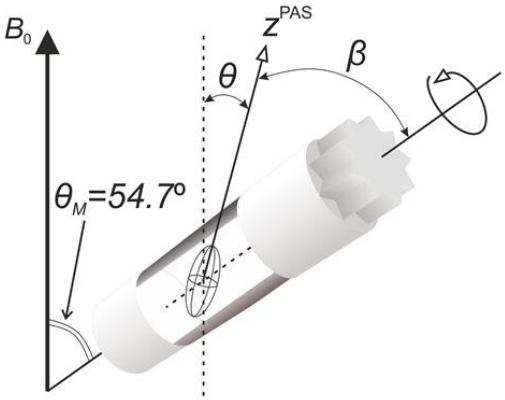

$$\langle 3\cos^2\theta - 1\rangle = \frac{1}{2}(3\cos^2\theta_M - 1)(3\cos^2\beta - 1)$$

Figure 3.6. Principle of Magic Angle Spinning (MAS). Interaction tensor is depicted as ellipsoid. Based on Ref 96.

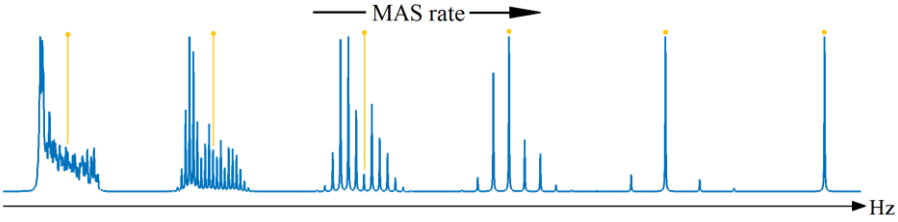

Figure 3.7. Simulations of powder pattern splitting into MAS sidebands by changing spinning rate. Yellow markings correspond to central line. For full static powder pattern see Fig. 3.5.

3.4 The experiment. Cross-polarization

Cross polarization (CP) is a common solid-state NMR experiment where polarization (*i.e.* magnetization) is transferred from one species of nuclei to another. Originally proposed by S. R. Hartmann and E. L. Hahn[97] in 1962 this method is still versatile even in modern NMR. It was developed to enhance sensitivity of a weakly magnetic nuclei like ^{13}C, ^{15}N using highly magnetic nucleus ^{1}H.

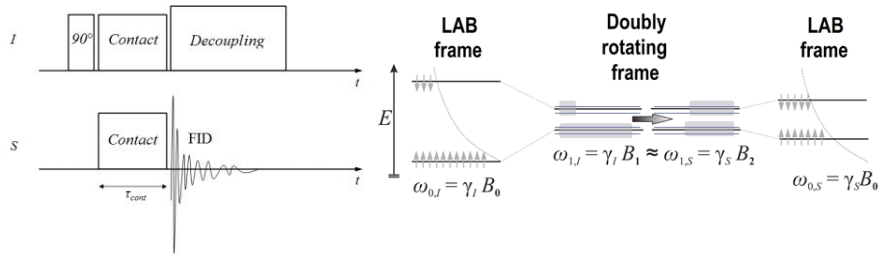

Figure 3.8. Cross-polarization NMR pulse sequence (on the left). *I* and *S* marks different resonant channels (say $I = {}^{1}H$, $S = {}^{13}C$). Simplified polarization transfer mechanism is on the right. Dashed line, grey arrows and bars all illustrate populations in the corresponding energy levels.

CP experiment scheme is trivial – after initial 90° pulse excitation for I spin species, spin-locking (or contact pulse) is simultaneously switched on at two channels (Fig. 3.8). The frequency at which spins nutate then depends on spin-locking power. Similarly, as in fixed frame, nutation frequency would correspond to energy levels in doubly rotating frame. Hence, at the exact Hartmann-Hahn (HH) condition, frequencies at which *I* and *S* spins nutate and thus energy gaps are identical ($\omega_{1,I} \approx \omega_{1,S}$). Therefore, at this so-called "contact" re-equilibration or flow of magnetization is possible. This flow would correspond to enhanced polarization of the second spin species S and "dehanced" polarization for the first one (I) as depicted in figure 3.8. Additional decoupling may be applied to obtain the highest possible resolution.

Generally, enhancement factor during CP depends on the natural isotope abundance *N* and gyromagnetic ratios γ of interacting nuclei:

$$\xi = \frac{\gamma_I}{\gamma_S} \cdot \frac{1}{1+N_S/N_I} \tag{3.17}$$

Thus, cross-polarization can be utilized between any spin-1/2 species, for example, ${}^{1}H \rightarrow {}^{13}C$, ${}^{1}H \rightarrow {}^{31}P$, ${}^{15}N \rightarrow {}^{13}C$ etc. However, CP is not always favourable like for the last example it would correspond to enhancement factor ξ = ~0.1 which means that carbon would essentially lose its polarization. Despite of unwanted signal loss in some cases, the time evolution of polarization "flow" can be valuable by the means of physical characterization in solids since polarization is transferred via dipolar interaction. This is the reason why CP kinetics can be considered important source of information.

Obviously, cross-polarization is not an instantaneous event of magnetization transfer. Typically, time duration for efficient transfer is at the order of hundreds of microseconds but it strongly depends on dipolar coupling strength and other physical parameters such as relaxation and spin diffusion.

In the semi-classical framework one can express Liouville-Neumann equation (3.7) for two interacting spins under CP conditions as it was originally realized by L. Muller[19]. Under exact HH condition Hamiltonian and $\hat{\hat{\Gamma}}$ superoperator in the doubly rotating frame has the following form:

$$\widehat{\mathcal{H}} = \omega_1\left(\hat{I}_x + \hat{S}_x\right) + \frac{b_{IS}}{2}\left(\hat{I}_y\hat{S}_y + \hat{I}_z\hat{S}_z\right) \tag{3.18}$$

$$\hat{\hat{\Gamma}}(\rho) = R\left\{\left[\hat{I}_x,\left[\hat{I}_x,\rho\right]\right] + \left[\hat{I}_y,\left[\hat{I}_y,\rho\right]\right] + \left[\hat{I}_z,\left[\hat{I}_z,\rho\right]\right]\right\} \tag{3.19}$$

Now, expression (3.19) is called isotropic spin diffusion superoperator, where R is diffusion rate. Initially, after first 90° pulse, density operator is equal to:

$$\hat{\rho}_0 = 1 - \mathcal{B}\hat{I}_x; \quad \mathcal{B} \equiv \frac{\hbar\omega_{0,I}}{\mathrm{k}T} \tag{3.20}$$

where $\mathcal{B}$ is a Boltzmann factor for I spins. Note that the density operator (3.20) only does not commute with the second term of Eq. (3.18). This means that oscillations following from Eq. (3.18) will maintain $b_{IS}/2$ frequency factor. The final solution for the magnetization along x axis for S spin is the following:

$$M(t) \equiv \mathrm{Tr}\left[\hat{\rho}(t)\hat{S}_x\right] = \frac{\mathcal{B}}{4}\left(1 - \frac{1}{2}\mathrm{e}^{-R\,t} - \frac{1}{2}\mathrm{e}^{-3R\frac{t}{2}}\cos\frac{b_{IS}\,t}{2}\right) \tag{3.21}$$

Lastly, to the simple form of the expression above relaxation mechanism must be added. During cross-polarization experiment relaxation occurs even during strong contact pulses (or so-called spin-locking pulses) and it should not be mixed with classical relaxation. Relaxation during spin-locking is called $T_{1\rho}$ longitudinal relaxation time in rotating frame. Rather pleasingly, it was shown by A. Naito that including relaxation into Eq. (3.21) only adds an additional exponent[98]:

$$M(t) = \mathrm{e}^{-t/T_{1\rho,I}}\frac{\mathcal{B}}{4}\left(1 - \frac{1}{2}\mathrm{e}^{-R\,t} - \frac{1}{2}\mathrm{e}^{-3R\frac{t}{2}}\cos\frac{b_{IS}\,t}{2}\right) \tag{3.22}$$

Note that only $T_{1\rho,I}$ for I spins is included since S spins typically relax slowly. If this is not the case, then relaxation for both spin system must be considered.

Relaxation, essentially, affects how much polarization can be transferred meanwhile coupling b_{IS} and spin diffusion R relates to time-scale and efficiency of the transfer (Fig. 3.9).

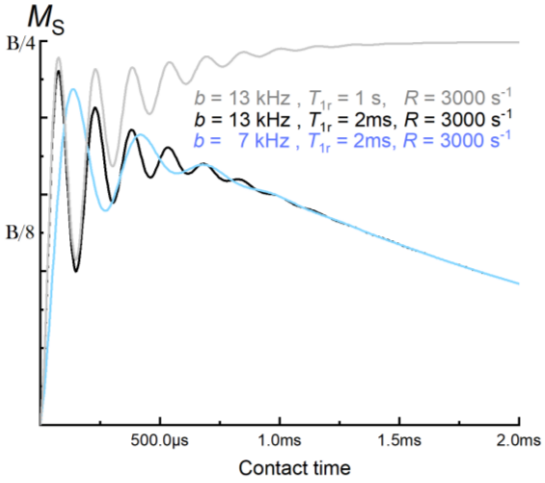

Figure 3.9. Modelled $^{1}H \rightarrow ^{13}C$ cross-polarization kinetics (3.22) using different parameters. Letter "B" denotes polarization as in (3.20).

Equation (3.22) is also known to be S-I*-I model where S-I* denotes an isolated spin pair. This approximation shown to be valid for static single crystals[18,19,99] whereas the concept of the CP kinetics can be visualized with thermodynamical block diagram (Fig. 3.10). Note, that $T_{1\rho}$ for S spin is not included in the equation (3.22) as it is usually far larger than for I spins.

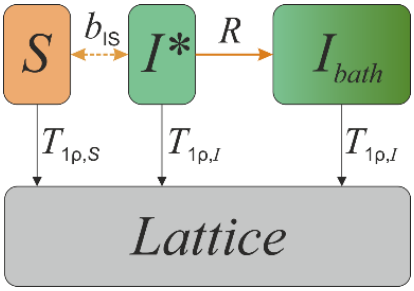

Figure 3.10. A representative block diagram for S-I*-I model of CP in isolated spin pair.

The mechanism of this model can be explained shortly. Initially, polarization starts at I* spin which exchanges polarization with S spin in oscillatory manner. Then, subsequent spin diffusion to I spin bath "drains" polarization from I* spins damping the ongoing oscillations. Lastly, overall relaxation damps the polarization in the system completely. This behaviour is shown in figure 3.9, where several parameters were varied.

For the reasons expressed before, CP can be combined with magic angle spinning to achieve high resolution spectra (Fig. 3.7) and therefore, the model for static single crystal may be inappropriate – model needs revision. Dipolar coupling strength depends on the orientation with magnetic field (see Fig. 3.3), thus mechanical sample spinning must introduce angular average for the cosine function in (3.22). The average of cosine in time, as shown by L. B. Alemany et al., can be expressed as Taylor series and thereafter function can be replaced by Gaussian function with the first order approximation:

$$\overline{\cos(b_i t/2)} \cong 1 - \frac{t^2}{2!\,T_2^2} \cong \mathrm{e}^{\frac{-t^2}{2\,T_2^2}} \tag{3.23}$$

The decay rate $1/T_2$ may be considered as a root-mean-squared average of $b_i/2$ properly weighted by the fraction of molecules with a given orientation corresponding to the oscillation frequency $b_i/2$[100], hence (3.22) becomes:

$$I(t) = I_0 \mathrm{e}^{-t/T_{1\rho,I}} \left(1 - \lambda \mathrm{e}^{-R\,t} - (1-\lambda)\mathrm{e}^{-3R\frac{t}{2}} \cdot \mathrm{e}^{\frac{-t^2}{2\,T_2^2}} \right) \tag{3.24}$$

where parameter $\lambda = 1/(n+1)$ was introduced by W. Kolodziejski regarding real case scenarios where nuclei might arrange into structure with several inequivalent S-I_n* spin pairs (with different DD couplings)[18].

To illustrate CP from pure thermodynamics point of view, consider two sub-systems having different internal spin temperature as it was depicted in figure 3.11. The term "spin temperature" was used even by S. R. Hartmann and it corresponds to population difference which is related to the Boltzmann distribution. For example, cold spin system has a large population difference and hot spin system – small population difference. Meaning, that the colder spin sub-system is, the bigger polarization is in that system. However, spin temperature can be (and at $t = 0$ is) negative or equal to zero. Then, spin-locking at exact Hartmann-Hahn condition establishes a thermal contact between two sub-systems (Fig. 3.11) thus the term "contact pulse". The

equilibration of this thermal energy can be then depicted as a flow of the polarization.

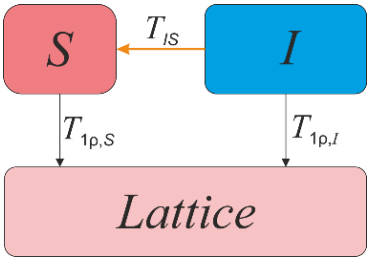

Figure 3.11. Block diagram of S-I model of thermodynamical cross-polarization.

Such flow of energy between sub-systems can be written in two differential equations which can be found in Ref 18. The solution of the differential equations is a simple biexponential process:

$$I(t) = I_0 \left(\frac{T_{1\rho}^I}{1-T_{IS}}\right)\left(\mathrm{e}^{-t/T_{1\rho}^I} - \mathrm{e}^{-t/T_{IS}}\right) \qquad (3.25)$$

where, again, $T_{1\rho}$ for S spin is neglected and, here, exchange time T_{IS} reflects the strength of the I-S and I-I dipolar couplings. The first bracket from now on will be omitted as T_{IS} is much faster than the relaxation time.

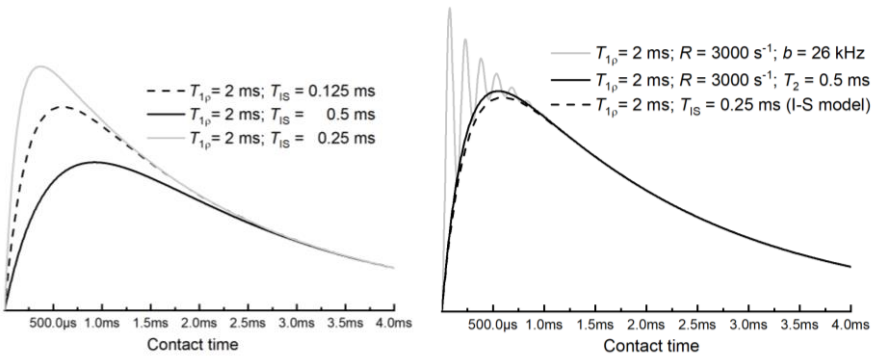

Figure 3.12. On the left – modelled CP kinetics of S-I model using (3.23), on the right – S-I*-I model. The latter was modelled using (3.22) as for static crystal and (3.24) for MAS average. Dashed line is identical in both pictures and represents I-S model.

In this section two models of CP where briefly presented: S-I*-I or so-called isolated spin pair model stemming from quantum mechanics and S-I being pure thermodynamical one. However, it is not clear which one should be used or, more importantly, whether they are not too oversimplified. Nevertheless, both models link CP kinetics to the dipolar coupling strength and other processes but rather qualitatively. Furthermore, if the discrepancy sometimes can be almost intelligible as seen on right-hand side in figure 3.12 then one needs to be careful making quantitative conclusions. These problems will be tackled in the experimental section where a large variety of CP kinetics were analysed.

3.5 2D spectroscopy. Heteronuclear correlation

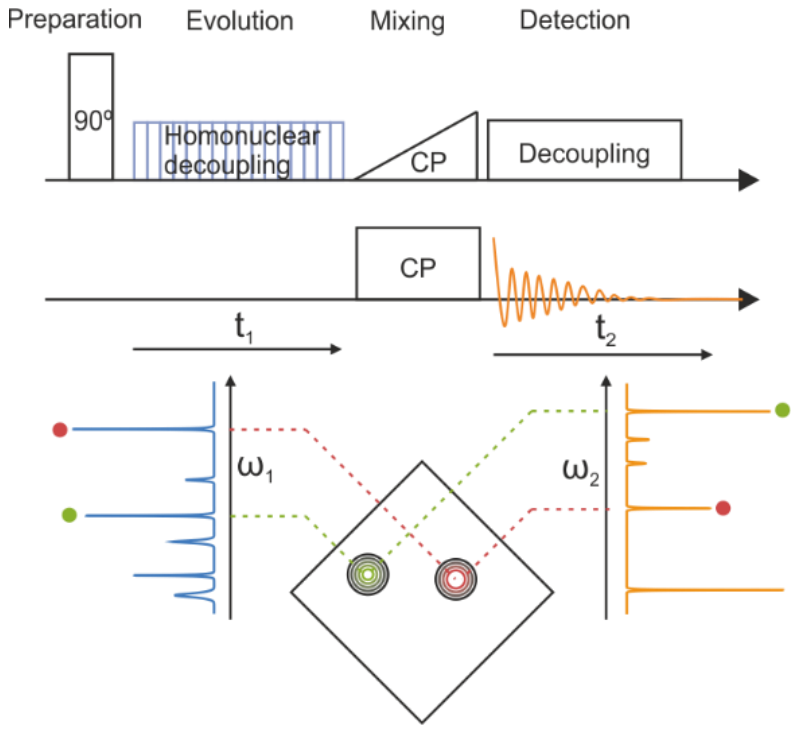

Figure 3.13. The principal scheme of frequency switched Lee-Goldburg cross-polarization heteronuclear correlation experiment.

It is not surprising, that in order to employ measurements of CP kinetics or any other technique, one needs to recognize and assign the spectral lines first. This task is not challenging if the molecular system is well explored or simple enough that the resonances can be found in catalogues in literature. However,

sometimes it is not the case and then spectral lines have to be correlated to a known reference to obtain fully defined spectrum. Correlation between different spectral lines is one of the main tasks of 2D spectroscopy.

Generally, any 2D experiment is a sequence of events: preparation, evolution, mixing and detection, respectively. In NMR spectroscopy, preparation and detection is mostly non-other than 90° pulse and FID (with optional decoupling). However, evolution and mixing are elements that provide with most diversity of methods. Let us focus on the experiment used in this work – frequency switched Lee-Goldburg cross-polarization heteronuclear correlation experiment (FSLG-CP HETCOR) (Fig. 3.13).

There are only couple of differences between the latter experiment and classic CP experiment depicted in figure 3.8. Firstly, cross-polarization contact is made by spin-locking pulses that one of which is ramped. Ramping of the pulse allows to ensure that within CP contact time Hartmann-Hahn condition where energy levels in doubly rotating frame match will be fulfilled as the energy gap is dependent on the pulse power. The pulse duration and other parameters are fixed (unlike in the CP kinetics measurement) such that I spins have enough time to transfer polarization to S spins for detection.

Secondly, the last difference to regular CP is the evolution present in HETCOR experiment. During evolution I spins (typically ^{1}H) need to evolve under chemical shift only, therefore must be decoupled from other interactions hence even from homonuclear coupling. As homonuclear coupling is strong and more symmetric regarding spin rotations this task is quite challenging. Luckily, many techniques have been developed and do not require a lot of optimization. Merely, it is done by flipping I spins by magic angle with NMR pulse and (spin-)locking them at that angle similarly to MAS technique where sample is spun mechanically. Since nutation frequencies are then in the order of 100 kHz and hence tenfold higher than those achieved with magic angle spinning homonuclear decoupling allows to preserve chemical shift information during evolution time t_1.

Performing double Fourier transformation first for detected FID (t_2 domain) and then to evolution time points results in 2D spectra. The peaks appearing in the spectrum means that *I* spins having specific chemical shift passed over their polarization to specific *S* spins during mixing time. In the present experiment spins are communicating through dipolar coupling, hence spatially nearest spins will pass their polarization most effectively or in other words they will correlate best. In the liquid-state NMR the most similar 2D experiment is known as NOESY (Nuclear Overhauser Effect Spectroscopy). Therefore, HETCOR spectra is another powerful tool for spectral assignment and even spatial characterization.

4. EXPERIMENTAL RESULTS

Experimental setup

The majority of experiments were performed in Institute of Chemical Physics at Vilnius University using Bruker AVANCE IIIHD NMR spectrometer and Bruker Ascend 400WB superconducting magnet exerting 9.41 T magnetic field at which proton resonance frequency is 400 MHz. The data was acquired using static and Magic Angle Spinning (MAS) Bruker probes. The former one is a broadband single channelled 4 mm probe capable of performing experiments in the temperature range of -150°C–+300°C. The latter 4 mm H/X CPMAS probe can withstand temperature range of -110°C–+150°C with samples spinning up to 15 kHz rate. Most of the experiments were done at room temperature under intermediate spinning frequencies (7-10 kHz). A few experiments were carried out on Bruker, Varian systems in Darmstadt-TU (Germany) and University of Southampton (UK), respectively, but were re-tested again in Vilnius University for consistency.

Cross-polarization (CP) experiments were conveyed under similar conditions for all samples. CP contact pulses were strong rectangular RF pulses (70-100 kHz) set to a single Hartmann-Hahn condition. Repetition delays were set according to pre-measurements of T_1 relaxation times using saturation recovery pulse program. CP kinetics consisted up to 1000 time points but, recorded with limit of 10 ms due to strong RF fields. Other parameters regarding CP kinetic measurement can be found in appendix (Table A1).

Results were initially analysed using built-in Bruker software *TopSpin 3.2*. Further analysis was done employing *Microcal Origin 9*, *Mathcad 15* and *MATLAB* packages. Few present simulations were done using *SpinDynamica* (published at Ref 101).

Materials

The first analysed material was calcium hydroxyapatite – $Ca_{10}(PO_4)_6(OH)_2$. It was synthesised by the aqueous sol-gel process in prof. habil. dr. A. Kareiva group at Vilnius University, Chemistry and Geosciences faculty, department of Inorganic chemistry. Calcium acetate monohydrate, $Ca(CH_3COO)_2 \cdot H_2O$ and ammonium hydrogen phosphate $(NH_4)_2HPO_4$, were selected as Ca and P sources, respectively, to obtain Ca/P molar ratio of 1.67. Another hydroxyapatite that contained amorphous clustered phosphate phase (ACP) was also synthesized in the same group. The

last nanostructured calcium hydroxyapatite (nano-CaHA) studied in this work was commercially available at Sigma Aldrich. The same vendor was available for used ionic liquid, amino acids, meso-porous silica as well as for poly-(vinyl phosphonic acid) (pVPA) polymer.

Polymer poly-(hydroxyethyl methacrylate) (pHEMA), however, was synthesised in prof. dr. R. Makuška group at Vilnius University, department of Organic chemistry. HEMA was polymerized in the presence of 4-((butylthio)carbonothioyl)thio)-4-cyanopentanoic acid as a RAFT chain transfer agent and 4,4-azobis(4-cyanovaleric acid). All acids were commercially available as well.

Likewise, commercially available was ammonium dihydrogen phosphate $NH_4H_2PO_4$ (ADP) which was purchased from Reachem Slovakia in 99 % purity and was used as a model compound. Lastly, all tripeptides investigated in this work were made in TU-Darmstadt by the members of prof. dr. G. Buntkowsky group.

4.1 Characterization by 1D spectroscopy

The initial ideas behind this work stem from the structural and composition analysis of phosphate materials, particularly, calcium hydroxyapatite (CaHA). Calcium hydroxyapatite as described in the last subsection were synthesized via trivial sol-gel route using different complexing agents that allowed to control crystallinity of the compound. Not surprisingly, the largest morphological difference was met is in the case of amorphous clustered phosphate phase containing (ACP) and nano-structured apatite[11,12,21].

First of all, the synthesis products were characterized by scanning electron microscopy (SEM) and energy-dispersive X-ray analysis using a Helios NanoLab 650 scanning electron microscope coupled with an energy-dispersive X-ray spectrometry system[102]. The XRD spectra can be found in appendix (Fig. A2). The characterization was needed to know which samples yield amorphous or well-structured morphologies.

Before initial works, it was not yet known what are the most crucial factors that influence the structural organization of the synthesis products. However, both ACP-CaHA and nano-CaHA can be compared with respect to the presence of structural manifolds of hydroxyl groups by means of ^{1}H NMR spectroscopy and later reinforced by FTIR spectroscopy (Fig. 4.2).

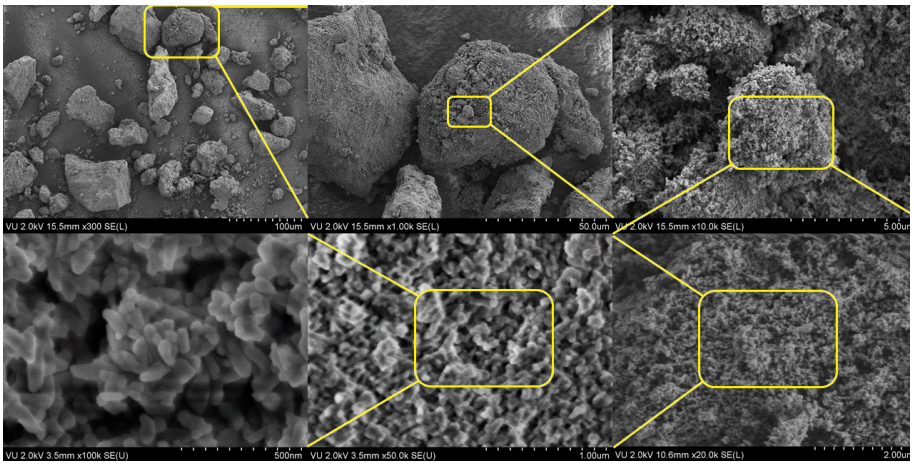

Figure 4.1. SEM image of nano-structured calcium hydroxyapatite.

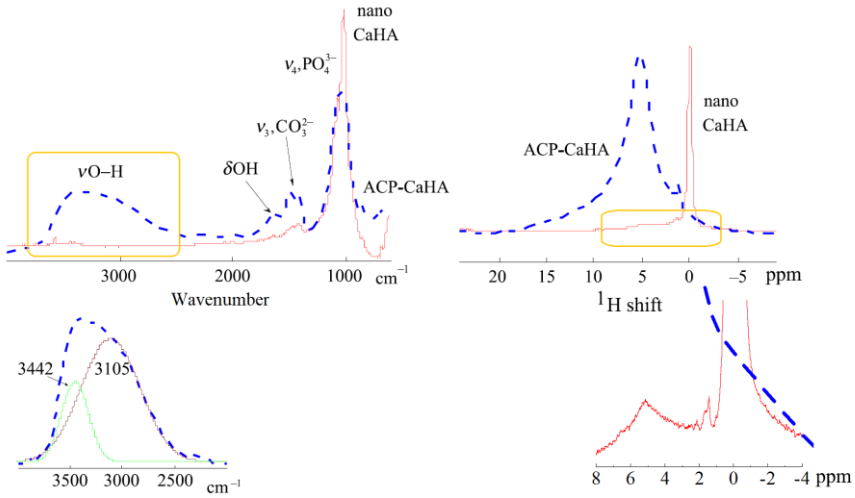

Figure 4.2. The comparison of FTIR and ^{1}H MAS (10 kHz) NMR spectra of nano-structured (nano-CaHA) and containing amorphous clustered phosphate phase (ACP-CaHA) calcium hydroxyapatite. Yellow boxes mark zoomed-in areas bellow. FTIR peaks are assigned following the ref [11].

The ratio between areas of 5 ppm peak *versus* 0 ppm peak (in NMR spectrum) is 0.14:1 which indicate that amount of structural -OH group in the nano-CaHA is significantly higher than the amount of adsorbed water. This can be approved by the presence of small sharp peak at 3572 cm^{-1} (in FTIR spectra) which corresponds to “free” -OH groups that are typically masked by broad feature as seen in ACP-CaHA FTIR spectra. The large broadening of

water signal in both NMR and FTIR spectra arises due to higher degree of freedom which adsorbed water possess and, moreover, these water molecules can chemically exchange with -OH groups on the surface, thus averaging out the 0 ppm peak in NMR spectrum. The large band at 3200 cm^{-1} can be decomposed into two overlapped peaks at 3442±2 cm^{-1} and 3105±4 cm^{-1}. The first corresponds to the stretching mode of structural -OH while the other to the stretching of the water in H-network. Another characteristic δOH band at 1645 cm^{-1} is also present meaning that the quantity of adsorbed water is indeed high[11,97]. These spectra indicate that the ratio between adsorbed water and structural -OH groups in phosphate are 3.4:1 and 0.14:1 for ACP-CaHA and nano-CaHA, respectively.

As phosphates obviously contain phosphorus it is trivial to employ ^{31}P NMR as is it often done for some closely relates systems[69,103]. Typically, ^{31}P spectra is said to arise from PO_4^{3-} groups and the broadening of the peak is due to amorphous phosphate located at the surfaces or at grain boundaries of HA nano-platelets. Furthermore, the signal shapes in both CaP and gel/CaP are typically found to be asymmetric and significantly broader, demonstrating structural inhomogeneities, which can include the presence of an additional phase difference from pure crystalline HA. The larger linewidth is clearly seen in the Fig. 4.3 for ACP-CaHA.

In the NMR studies of structuring effects, it can be assumed that the presence of various non-uniformities (short-range disorder, heterogeneities, etc) in nano- and mesoscopic scales enhances the Gauss contribution of signals, whereas the Lorentz contribution is originated from uniform spin interactions and dynamics. Now, random processes like motion or reorientation can be described in terms of correlation function $C(\tau)\sim\exp(-k\,\tau)$, where k is a rate constant. Fourier transform of this equation is nothing else than Lorentz function and this is also known as homogeneous broadening. Homogeneous broadening is known to be harder to supress using magic angle spinning[104].

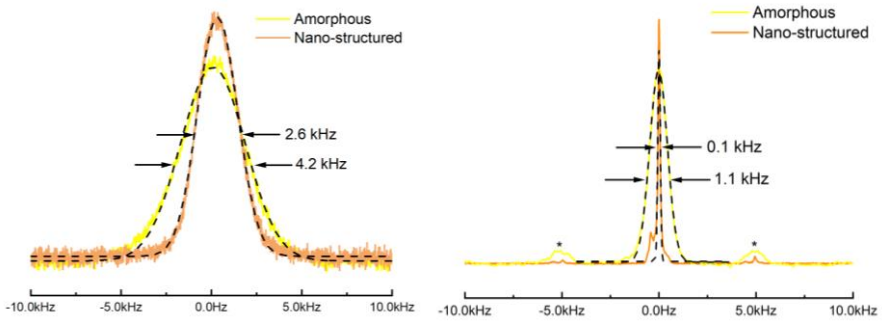

Figure 4.3. 90° pulse signals of ^{31}P in static (on the left) sample and under MAS (on the right). Dashed line indicates good coincidence with the Gaussian shape where widths are shown for each peak. Asterisks denote spinning sidebands at 5 kHz.

Furthermore, rotor-synchronized MAS linewidth ($\Delta\nu_{1/2}$) also depends on the strength of anisotropic spin interactions. Strength will be expressed in units of hertz as commonly done in NMR spectroscopy by a parameter ν_{an}. In the fast spinning regime, the linewidth $\Delta\nu_{1/2}$ can be expressed as

$$\Delta\nu_{1/2} = \frac{\pi\nu_{an}^2}{2\nu_{MAS}(16\pi^2 + x^2)^2} \times [-16\pi^2(e^{-x} - 1 - x) + x^2(e^{-x} - 1 + x)] \quad (4.1)$$

here $x = k/\nu_{MAS}$[104]. In the regime close to the maximum broadening, where $2\pi\nu_{MAS}/k \approx 0.55$, this equation can be simplified:

$$\Delta\nu_{1/2} = \frac{k\pi\nu_{an}^2}{2k^2 + 32\pi^2\nu_{MAS}^2} \quad (4.2)$$

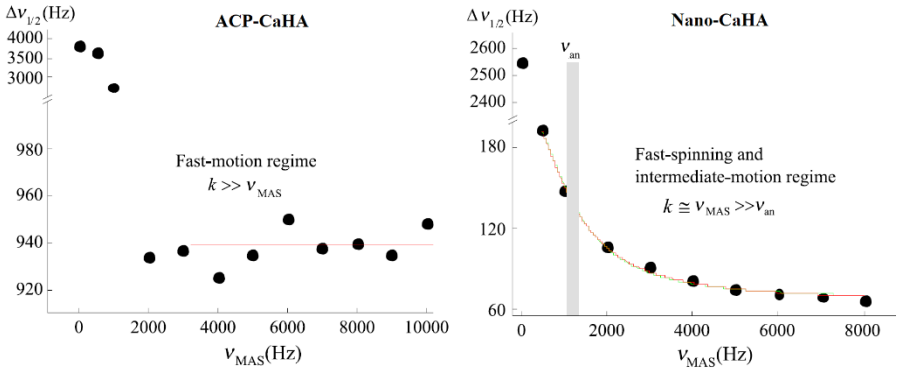

Figure 4.4. Linewidth of the ^{31}P NMR peak *versus* MAS rate in the case of ACP-CaHA and nano-CaHA. Grey bar marks ν_{an} where motional averaging starts to be efficient. More details in the text.

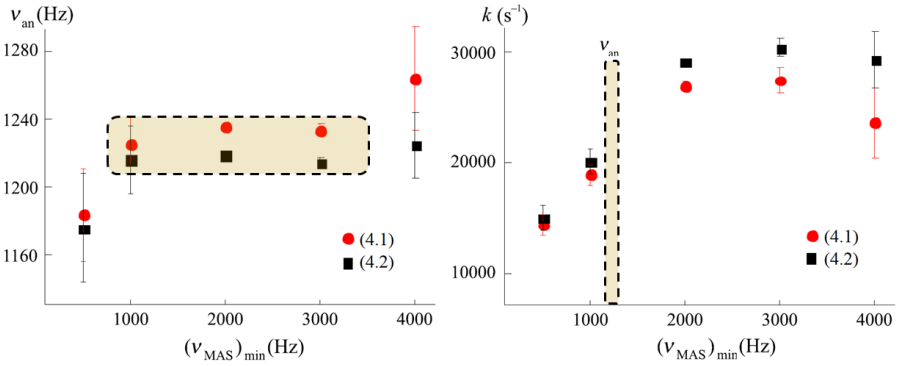

Figure 4.5. On the left – magnitude of the inhomogeneous anisotropic broadening ν_{an}, on the right – random reorientation rate constant k. Both parameters were calculated fitting results of nano-CaHA with (4.1) and (4.2) (see Fig. 4.4). More details are in the text.

Now, the Magic Angle Spinning averaging is clearly different in amorphous material than nano-structured one (Fig. 4.4). The most noticeable difference is that ACP-CaHA ^{31}P NMR linewidth drops down rapidly to a constant width when sample is spinning above ~2000 Hz rate. According to equations (4.1) and (4.2) linewidth can only be invariant of MAS rate if $k >> 4\pi\nu_{MAS}$. It suggests that fast spin motion does takes place ACP-CaHA reinforcing, again, the evidence of the large amount of mobile adsorbed water molecules. Contrastingly, in the nano-structure apatite NMR linewidth strongly depends on the spinning frequency. That allows to evaluate

parameters k and ν_{an} using previously mentioned equations. However, these expressions are only valid in the fast spinning regime. For this purpose, the fitting was done several times excluding slow MAS rate points leaving some minimal value of $(\nu_{MAS})_{min}$. The fitting results are shown in figure 4.5. The obtained fitted values of ν_{an} =1220±20 Hz and k = ~30000 s^{-1} for nano-CaHA indeed indicate a very slow dynamical motion since 2 kHz MAS rate already is larger than the strength of anisotropic spin interactions

The time-scales of the random processes can be checked using relaxation measurements. This is based on the fact that relaxation is induced by random fluctuations. Without going to deep into Redfield theory of relaxation, one can consider that these fluctuations can be defined with a memory function and corresponding correlation time. The Fourier transform of auto-correlation function (if mono-exponential behaviour is assumed) is a Lorentz spectral density function:

$$J(\omega) = \frac{\tau}{1+\omega^2\tau^2} \tag{4.3}$$

where τ is a correlation time for any random process. As the time-scale decreases (meaning faster motion) spectral density function flattens (Fig. 4.6) and for slow events it will be sharp. For simplicity let us assume that fluctuations at Larmor frequency are the most relevant. The reason is trivial – fluctuations that resonate with the system will be most effective to drive it to thermal equilibrium. Therefore, if faster motions have relatively flat spectral density, it will drive system to equilibrium faster as the spectral density at Larmor frequency is higher.

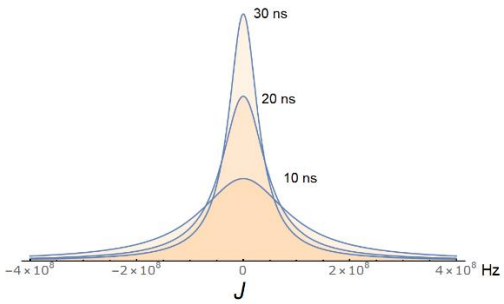

Figure 4.6. Spectral density function $J(\omega)$ with different correlation times.

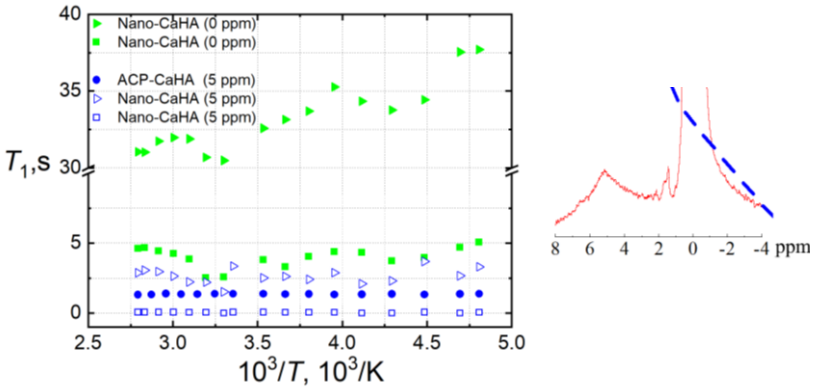

Figure 4.7. Dependencies of ^{1}H longitudinal relaxation time to temperature in CaHA samples. Nano-structured CaHA seemed to have biexponential relaxation, hence two components for single peak were defined. Also note, that ACP-CaHA does not have pronounced 0 ppm peak and hence only one label. Inset is taken from figure 4.2 for clarity. Experiment were carried out using saturation recovery pulse sequence with 16 delay points for the fitting.

As it is seen in the figure 4.7, amorphous hydroxyapatite has relatively shorter T_1 relaxation time than nano-CaHA. The reason is that the relaxation is originating from the large amount of adsorbed water which is can be also partially seen in the case of nanostructured material. The dominating signal in nano-CaHA is that from structural -OH groups which relax significantly slower. Along with the statements of the last paragraph, this means that adsorbed water experiences faster random reorientations. If these reorientations are already rapid, the changes in temperature will inflict much of a change in correlation time. Perhaps, this is why T_1 for the -OH groups depend on temperature more as seen in figure 4.7. Biexponential behaviour of relaxation in the case of nano-CaHA could be linked to again to the fact that the quantity of adsorbed water is small. This means that relaxation is not dominated by homonuclear interaction between hydrogen atoms as it is expected in a neat water. Then considerable influence of heteronuclear coupling could lead to biexponential process. Obviously, last statements would require further experimental background which will not be given as it would be out of the scope of this work.

Conclusions of section 4.1

- FTIR and NMR peak assesment indicate large quantity of adsorbed surface water in amorphous calcium hydroxyapatite, whereas in the case of nano-structured apatite -OH structural groups are dominant.
- Fast motion of random reorientations in the amorphous CaHA was confirmed by MAS effect and by spin-relaxation time measurements.
- One-dimensional NMR spectroscopy can provide with the information about the composition and dynamical time-scales occurring in structures.

4.2 Cross-polarization kinetics in CaHA

Previously it was shown that some information can be obtained using 1D spectroscopy. Information relating to structural composition and dynamical time-scales is important, especially if the crystallinity directly depend on the complexing agents used. However, pure crystallographic parameters like order and packing cannot be tackled using only previously used techniques. The following section will exploit the possibility of using cross-polarization instead of the common experiments like XRD or ND.

4.2.1 Towards dipolar coupling distribution

Due to a proper instrumental setting, high data point density measurements of $^{1}H \rightarrow ^{31}P$ CP kinetics have been carried out for two previously described calcium hydroxyapatites having different morphological structure: amorphous and nano-structured (figures 4.8 and 4.9). It is important to note that commercially available CaHA seemingly had nano-structured morphology as one of the synthesized ones, therefore, identical name (nano-CaHA) will be maintained. Each experimental curve contains up to 500 equidistance points over contact time range of 50 μs to 10 ms. Such high data point density reduces the excess degrees of freedom in the nonlinear curve fitting procedure targeting χ^2 flow toward the "true" (i.e., global) minimum on the multiparameter surface. Here χ^2 is the sum of weighted squares of deviations of the chosen theoretical model curve from the experimental points. High point density also makes more rigorous decision possible concerning the validity of the hypothetic models as well as allows more fitting parameters to be used unambiguously.

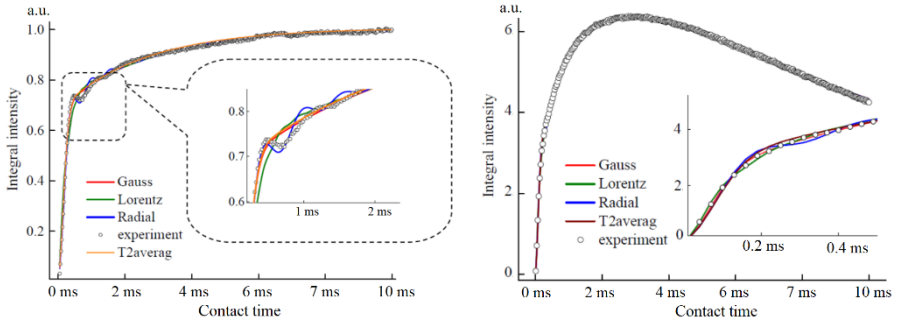

Figure 4.8. $^{1}H \rightarrow ^{31}P$ CP kinetics (peak integral *versus* variable contact time) in the static nano-CaHA (on the left) and ACP-CaHA (on the right). The fitting was carried out using Eq. (4.6) taking $P(b/2)$ to be Gauss, Lorentz, and Radial functions and using T2-averaging (Eq. 3.24). The fit parameters are given in Table 1.

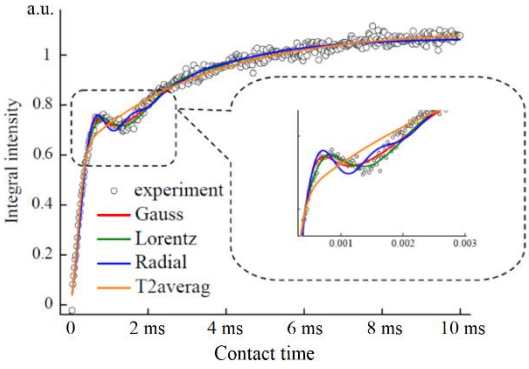

Figure 4.9. $^{1}H \rightarrow ^{31}P$ CP-MAS (9 kHz) kinetics in nano-CaHA. The fitting was done using different spin coupling distribution profiles as in Fig. 4.8. The fit parameters are presented in Table 1.

The CP kinetics observed in the nano-CaHA exhibit blurred oscillation of intensity in the short contact time range, whereas it is completely absent in ACP-CaHA (figures 4.8 and 4.9). In order to describe this phenomenon, one can consult subsection 3.4 where two distinct CP models were presented. Isolated spin pair model (also known as S-I*-I model) predicts that S-I* spin pair or cluster of inequivalent pairs exchange polarization in an oscillatory manner which mimics the energy exchange between a pair of coupled pendulums (see Eq. 3.22). These oscillations are then damped by the subsequent spin-diffusion to a large *I* spin reservoir.

In addition to spin diffusion, another source of incoherence has to accounted for. Namely, equation (3.22) (or isolated spin pair approximation) is only viable in a perfect single crystal which is not the case in complex solid like CaHA. The CP kinetic data for complex solids is an average over the whole distribution of dipolar splitting b that depends on the spatial parameters (internuclear distance (r_{jk}) and orientation in the magnetic field (θ)):

$$b = -\frac{\mu_0}{4\pi}\frac{\gamma_j\gamma_k}{{r_{jk}}^3}\frac{3\cos^2\theta-1}{2} = b_{jk}\frac{3\cos^2\theta-1}{2} \tag{4.4}$$

Here the difference between b and to b_{jk} constant is that b depends on angle θ on contrast to b_{jk}. Dipolar splitting b, in other words, is a part in the Hamiltonian (3.13) which is responsible for forming Pake pattern in a spectrum (figures 3.3 and 4.10) whereas b_{jk} for the size of splitting. The cosine in Eq. (3.22) then should be averaged over all possible b values weighted by the fraction of spin pairs with a set of spatial parameters that corresponds to the oscillation frequency $b_i/2$:

$$\overline{\cos\left(\frac{2\pi\, b\, t}{2}\right)} = \sum P\left(\frac{b_i}{2}\right)\cos\left(\frac{2\pi\, b_i\, t}{2}\right) \tag{4.5}$$

where the normalized spin coupling distribution profile $P(b/2)$ is introduced. Its shape for disordered solids is complex. To a good approximation, $P(b/2)$ can be considered as the envelope of the superposition of Pake singularities from the pairs of spins having different internuclear distances (Fig 4.10).

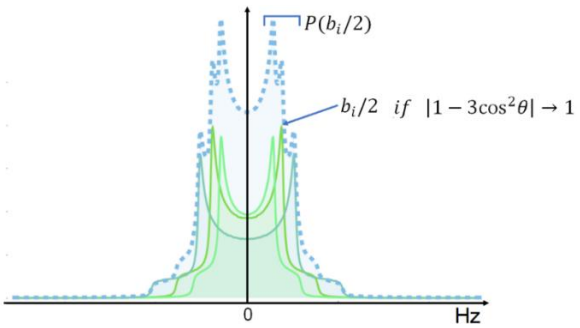

Figure 4.10. Simulated dipolar coupling spectra for three slightly different spin pairs. Spin coupling distribution profile $P(b/2)$ for disordered solids would correspond to the “fine” structure on the edge of the total (blue) Pake pattern.

The exact shape of $P(b/2)$ is generally unknown. Moreover, due to dipolar coupling inverse cubic dependency to internuclear distance r_{jk}, this shape also is different at different length scales. Despite this uncertainty, in many cases ^{31}P NMR signals appear as being Gauss function or Voigt shape dominated by Gauss contribution[11,102]. Thus, for simplicity, to illustrate b averaging consider Gauss function where width w reflects the extent of the overall spin coupling distribution or the disorder of dipolar coupling. The examples are shown in figure 4.11 where curves where modelled using cosine average instead of Gauss function in (3.24):

$$I(t) = I_0 \mathrm{e}^{-t/T_{1\rho,I}} \left(1 - \lambda \mathrm{e}^{-R\,t} - (1-\lambda)\mathrm{e}^{-3R\frac{t}{2}} \sum P\left(\frac{b_i}{2}\right) \cos\left(\frac{2\pi\, b_i\, t}{2}\right)\right) \quad (4.6)$$

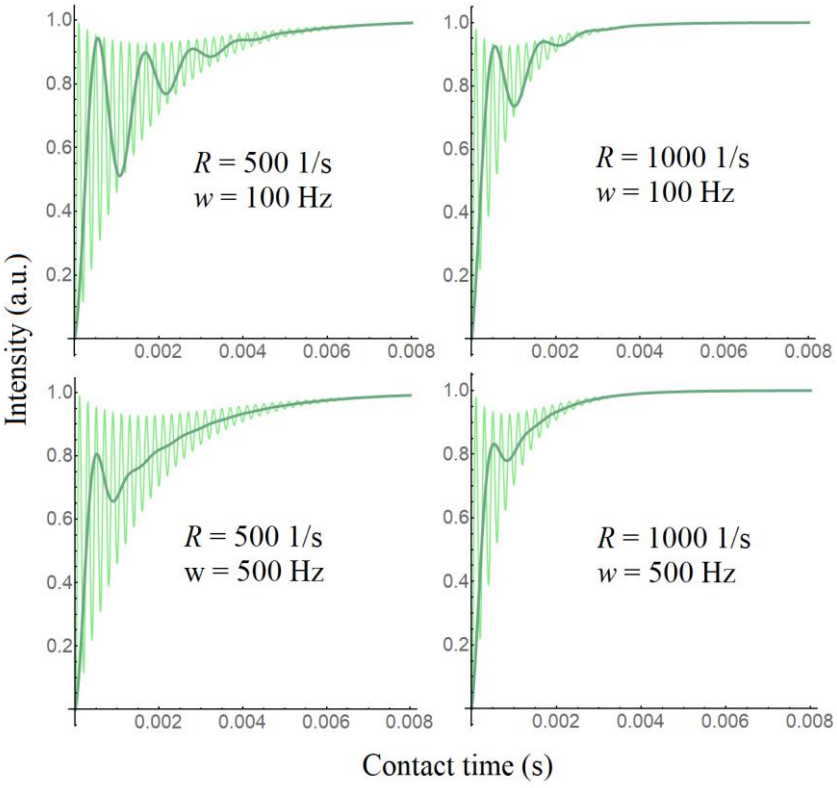

Figure 4.11. Averaging of oscillations in CP kinetics upon change of structural disorder (w) and spin-diffusion rate (R). Green lines in the background represent CP kinetics as described in equation (3.22) while b = 10 kHz. Bold green lines were modelled using Gaussian $P(b/2)$ distribution (Eq. (4.6)) centred at b = 1.8 kHz and $T_{1\rho} \to \infty$ is fixed in all cases.

The effect upon changing the Gaussian width and spin diffusion rate is seen in the picture above. At the first glace it looks like both parameters only damp the initial oscillation but, actually, there is a slight difference in responses to these changes. Thus, both elements (w and R) can be distinguished and revealed if convenient processing is applied.

Essentially, only difference of the expression above and (3.24) is that cosine average is in its explicit from. If then one would assume complete disorder, short CP contact time or very weak couplings, this average would approach and become a Gauss function. As the subsequent equation (3.24) is characterized by Gaussian width, this function will be called T_2-average, where T_2 is the time constant of Gauss decay. This limit is perhaps the most often used for the processing of experimental CP kinetic data in the cases where it was deduced that the S-I*-I model[18,105] was to be more appropriate, compared to the thermodynamic one (S-I model), for example, as in refs 102,106,107. It is important to address that notation T_2 itself has a physical meaning. As Gauss decay value characterizes ^{31}P-^{1}H dipolar coupling it can be approximately equal to spin-spin relaxation time. And indeed, for the static samples the full widths at half-maximum (FWHM) obtained by the fitting ^{31}P line-shape corelates to the T_2 of the Gaussian distribution. This is achieved after CSA contribution is removed mainly when DD interaction dominates. Fitting the CP kinetic curves with function (3.24) shown that the "uncertainty" relation FWHM$\cdot T_2 = 0.355$ is close to the exact 0.375 value for the "true" Gauss function.

As previously seen in figures 4.8 and 4.9, various $P(b/2)$ shapes were tested. Some of them, like Lorentz and Gauss functions are a common spectral line-shapes but radial profile was specially developed for this purpose. It is based on atomic distribution in polycrystalline and amorphous systems. Namely, the atomic radial distribution function $g(r)$ contains several sharp peaks close to the centre ($r = 0$) that relate to the first- and the second coordination shells (Fig. 4.12). Going further from the centre, the number of atoms increases as dr slice is proportional to $4\pi g(t)r^2\mathrm{d}r$ (see Fig. 4.12 left side). In the long-range, function density function $g(r) \rightarrow 1$ because of uniform distribution, thus overall number of atoms is asymptotically equal to $N(r) \sim r^2$. Using (3.12) relationship one can find that radial distribution profile is long-range limit is $P_R(r) \sim b^{-2/3}$. Therefore, all mentioned distribution profiles: Radial (R), Gauss (G), Lorentz (L) and T_2-average, were used with equation (4.6) to fit CP data for two CaHA samples.

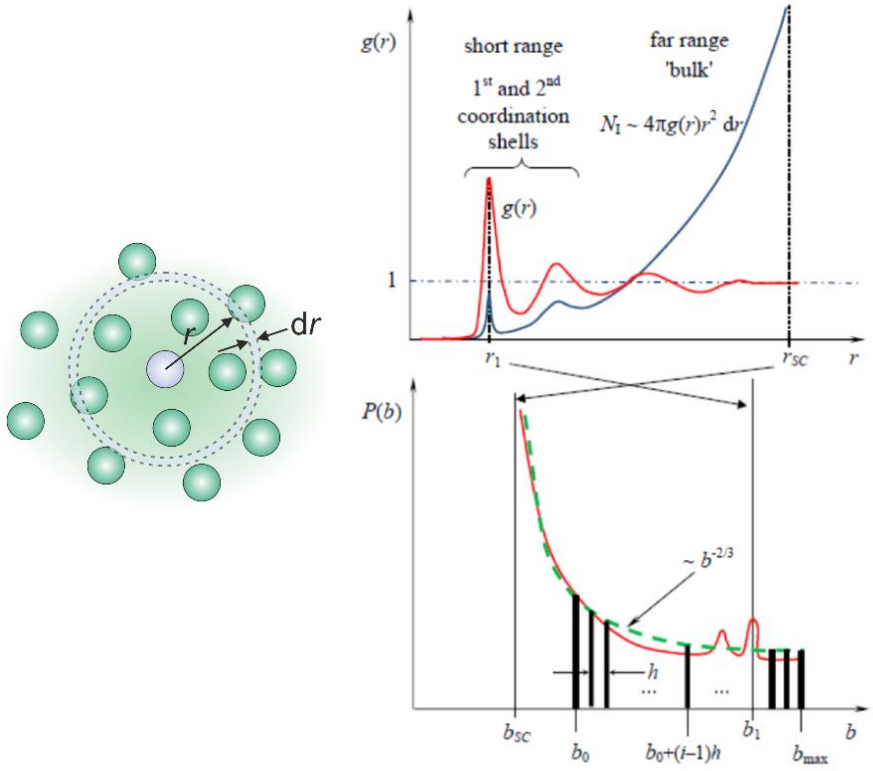

Figure 4.12. Explanation of radial distribution. The optimal step for discrete treatment h and the spin coupling extent (from b_{SC} to b_{max}) were determined in each case adjusting them during the curve fitting routine (see Table 1). More comments in the text.

Table 1. Fit parameter of CP kinetic curves shown in figures 4.7-4.8.

Nano-structured calcium hydroxyapatite								
	Static sample				MAS, 9 kHz			
$P(b)$	R	G	L	T_2-av.	R	G	L	T_2-av.
λ	0.39	0.30	0.39	0.33	0.61	0.60	0.60	0.47
R_{diff}, 1/s	455	385	455	400	476	455	455	313
b_0, Hz		0	320			800	885	
w, Hz		1920	1290			850	590	
T_2, ms				0.24				0.28
b_{max}, Hz	3500				2200			
b_{min}, Hz	330				740			
$T_{1\rho}$	∞							
χ^2, ‰	7	14	7	8	18	16	15	20

Amorphous calcium hydroxyapatite								
	Static sample				MAS, 5 kHz			
$P(b)$	R	G	L	T_2-av	R	G	L	T_2-av
λ	0.69	0.64	0.65	0.69	0.8	0.73	0.75	0.70
R_{diff}, 1/s	769	715	715	715	1111	1111	1111	1000
b_0, Hz		0	0			0	0	
w, Hz		4600	2500			2500	1400	
T_2, ms				0.12				0.34
b_{max}, Hz	7600				2400			
b_{min}, Hz	470				540			
$T_{1\infty}$	0.015 s				0.011 s			
χ^2, ‰	7	5	6	7	4	3	3	3

Nearly perfect global fit was achieved in all cases ($R^2 \sim 0.993-0.999$ and $(<\chi^2>)^{1/2}/I_{max} \sim 0.3-1.6\%$, see Table 1) independently on the spin coupling distribution profiles used. Results also underline some essential differences of amorphous and nano-structured material. Firstly, in addition to random reorientations, spin diffusion in ACP-CaHA is more rapid than in nano-CaHA as well. It means that bulk of adsorbed water provides with a large network of hydrogen nuclei which could increase the diffusion rate. Thus, adsorbed water can play an important role in changing the dynamics observed in structure.

It can be seen that some fitting parameters change with different magic angle spinning rate as well. Particularly, parameters w, T_2, b_{max}, b_{min} that relate coherent oscillations during CP to disorder suggest that magic angle spinning reduces disorder. Furthermore, parameter $\lambda = 1/(1+N)$ (where N is number of non-equivalent spin pairs) increases, meaning that CP kinetics are governed by fewer spin pairs. This is an important observation of which emphasize on MAS effect during cross-polarization experiment.

The fitting parameters generally describes structural properties of the apatites, nonetheless, detailed structural information is hidden in initial period of 2 ms where the CP oscillations are seen. The exact frequency distribution of these oscillation in unknown and hence using general functions could not give a precise measure. It means that the information concerning the short-range order (first and second coordination shells, Figure 4.10) is lost if any of R, G, and L profiles or the overall T_2 averaging (Eq. (3.33)) are applied. This becomes particularly obvious in the case of the radial distribution function $R(b) \sim b^{-2/3}$ that was derived taking $g(r) \to 1$, $r \to \infty$. The steepness of R, G, and L are similar at $b \to 0$, that is, moving to the far range. Therefore, it was not surprising that for each studied system the values of "bulk" parameters (λ, R_{diff}, and $T_{1\rho}$) that were determined by the global fitting are practically the

same (Table 1). Furthermore, parameter λ steps over the value of 0.5 which is rationally impossible. Henceforth, further revision is required.

4.2.2 Inverse calculation to dipolar coupling distribution

The problem of misalignment of non-linear fit to the first few tens of microseconds in CP wherein oscillations are the most pronounced was nicely solved with cut-off averaging first introduced in ref 102 and explicitly described in the dissertation of V.Klimavičius[108]. Nevertheless, the main idea of the cut-off averaging is one of the most crucial ones in the present work. The challenge is to find the exact $P(b/2)$ profile which would allow to reproduce a distribution of interacting spins at the short- and moderate internuclear distances. If this is achieved, the precise information about the spatial distribution of interacting spins (when protons surround ^{31}P nuclei) can be trivially calculated by the reverse recalculation from b-variable to the distances (r) using relationship (3.12). However, this approach forces to reconstruct the strategy of the processing of CP kinetics curves in the opposite direction.

Firstly, one has to recognize that the explicit cosine average (4.5) is nothing more than the real part of discrete Fourier transformation:

$$\overline{\cos\left(\frac{2\pi\, b\, t}{2}\right)} = \frac{\sum P\left(\frac{b_i}{2}\right)\cos\left(\frac{2\pi\, b_i\, t}{2}\right)}{\sum P\left(\frac{b_i}{2}\right)} \rightarrow \frac{1}{Norm}\sum P\left(\frac{b_i}{2}\right)\cos\left(\frac{2\pi\, b_i\, t}{2}\right) \equiv \mathrm{Re}\left\{\widehat{FT}\left[P\left(\frac{b}{2}\right)\right]\right\} \tag{4.7}$$

This means that coherent part of CP kinetics is accessible via Fourier transform of cosine average. Thus, if other global parameters can be fitted using generic profiles of $P(b)$, real profile can be extracted from the fitting parameters using the following routine:

$$P\left(\frac{b}{2}\right) \sim \left|\widehat{FT}^{-1}\frac{1-\lambda f_1 - I(t)/I_0 f_3}{(1-\lambda) f_2}\right| \tag{4.8}$$

where $f_1 = \exp(-R\, t)$, $f_2 = \exp(-1.5\, R\, t)$, and $f_3 = \exp(-t/\, T_{1\rho})$. Meaning that suppression of all other fitting parameters introduces a possibility to estimate the true profile. Hence, the functions f_1,f_2,f_3 are easily calculated after the fitting procedure and then used in Eq. (4.8). It is important to mention, that in the cases where magic angle spinning is applied, the true dipolar coupling

constant is rescaled by factor depending on the Hartmann-Hahn (HH) condition used[109,110]. If MAS is coupled with CP, classical ($\omega_{1,I} \approx \omega_{1,S}$) condition for contact splits into manifolds of sidebands ($\omega_{1I} - \omega_{1S} = n\,\omega_{MAS}$, see Fig. 4.16). It the present work, all experiments were carried out at the same $n = \pm 1$ condition which results in scaling factor of $\sqrt{2}$. The results of processing ACP-CaHA and nano-CaHA CP kinetics with with Eq. (4.8) and relationship (3.12) is shown in figure 4.13.

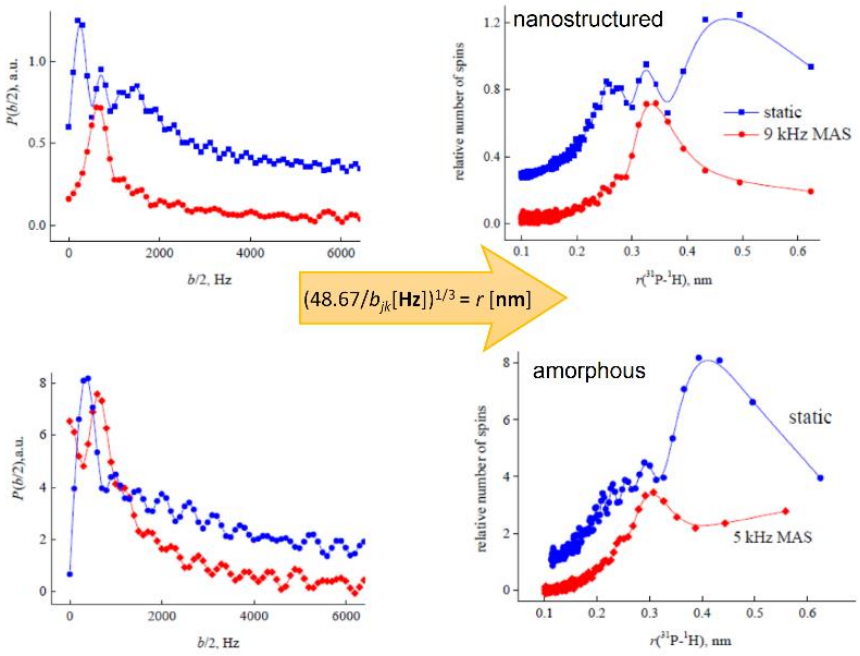

Figure 4.13. Calculated $P(b)$ function and corresponding spatial distribution of protons surrounding ^{31}P nuclei in nano- and ACP-CaHA. The $b/2$ axis for magic angle spinning results had to be rescaled by factor $\sqrt{2}$ due to a specific Hartmann-Hahn condition.

The spatial distribution profiles consist of three maxima at 0.24−0.27, 0.30−0.34, and at ca. 0.5 nm. The differences are seen in their relative heights and in the resolution of the peaks. Particularly interesting is the clear presence of the peak at 0.24−0.27 nm in nano-CaHA (Fig. 4.13). The distances of 0.21−0.25 nm are typical for P−O−H structures that are found in some related systems like calcium phosphate gelatine nanocomposites[107], sol−gel derived SnO_2 nanoparticles capped by phosphonic acids[110], and potassium- and ammonium dihydrogen phosphates (KDP and ADP)[32]. In CaHA, the protons are not part of the phosphate group and thus such short P···H contacts should

not be met. In pure crystalline CaHA, each P atom has two protons distanced at 0.385 nm and further two at 0.42 nm, while others are more than 0.6 nm away. Nevertheless, the observations using FTIR and NMR techniques suggest or even confirm the presence of hydrogen phosphate units in the nanostructured samples. Thus, the analysis becomes harder because the spectral manifestation of hydrogen phosphate groups are often hidden under other features. For example, the FTIR band of HPO_4^{2-} at ca. 540 cm^{-1} is commonly found to be strongly overlapped by the intensive modes of PO_4^{3-} in the regular "apatitic" environment[111]. The signals of HPO_4^{2-} in NMR spectra, that is, ^1H at ~11 ppm[112] and ^{31}P at ca. 0.45−1.3 ppm[111], look like the shoulders of the strong central dominant peaks from the bulk. Hence, in all these cases for HPO_4^{2-} signal/band to be resolved, one requires rather precise band separation procedures with an *a priori* certainty that this band is present. Even more clearly the presence of HPO_4^{2-} can be extracted using 2D HETCOR experiments[112]. Also, note the possible presence $^{31}P-^1H$ spin pairs with the closest distance 0.22−0.25 nm has been found in calcium phosphate gelatine nanocomposites, where it has been deduced from the simulation of CP kinetics[111].

The P−O−H structural motifs with P·H distances of 0.2−0.25 nm are present mainly on the surface layer that is not seen in XRD because of its disordered nature[113]. Therefore, the fact that the peak at 0.24−0.27 nm is clearly resolved in the spatial distribution profile of the nano-CaHA sample and hardly noticeable in the case of amorph-CaHA is easily understood by taking into account the differences in surface organization in nanostructured and amorphous materials. Amorphous material, on the other hand, consist a large amount of adsorbed water and seen in the figure 4.2. Hence it could be that large feature at ~0.4 nm (Fig. 4.13) is originating from the large H-bond network of adsorbed water. Although, it may be also deviations of -OH groups with sequent displacements of corresponding oxygen atoms that lead to the appearance of distances typical for H-bonds. Thus, discussion on either of the last statements will be left open.

Another important aspect is the employment of magic angle spinning as it has a clear effect of the obtained spatial distributions of interacting spin pairs. It follows that ^{31}P interactions with the protons on the surface layers (the peak at 0.24−0.27 nm) or with remote protons ($r_{P\text{-}H} > 0.5$ nm) are affected by MAS most dramatically. It is again worth to note parameter λ or otherwise the number of interacting spin pairs N decreases from 1.9 to 0.7 going from static to rotating nano-CaHA sample. This means that if the spin diffusion is slow enough and oscillations are not damped substantially isolated spin pair approximation becomes more appropriate. As a result, the dominant dipolar

coupling can be found either by calculating Fourier transformation of the CP curves or using equation (3.22).

Unfortunately, few sources of error of the present processing strategy have to be considered. Namely, the equation (3.22) is a model of isolated spin pair, but for the one that is at the single orientation with respect to the external magnetic field. On the other hand, this discrepancy was covered already when it was assumed that mostly the edges of Pake pattern correspond to coherent cross-polarization and thus appears in the dipolar coupling distribution. Unfortunately, this means that the result of the current processing route is not going to be a full cosine average, although the difference might not be significant. The goal of pure distance-depending distribution demands for the processing route were angular averaging effects are incorporated. Thus, the CP models must be revised.

Conclusions of section 4.2

- The high point density in the cross-polarization measurements for the nano-structured (nano-CaHA) and amorphous clustered phosphate phase containing calcium hydroxyapatite (ACP-CaHA) revealed structural features and differences within sub-nano scales.

- Fitting parameters like spin diffusion, relaxation rate, spin cluster size found to be almost invariant to spatial distribution profile. This allowed to extract the coherent part of cross-polarization and inverse-calculate dipolar coupling distribution. The use of radial function suppresses long-range order effects.

- Characteristic internuclear distances $r(^{1}H\text{-}^{31}P)$ were deduced for the nano-CaHA and ACP-CaHA. The absence of distance at *ca.* 0.26 nm in ACP-CaHA reflects the main difference in surface morphology between nano-structured and amorphous material.

- It has been demonstrated that magic angle spinning averages out long-range spin couples originated from adsorbed water network and disordered surface groups. This means that magic angle spinning probes local and short-range CP dynamics and reduces cluster size of interacting spins.

4.3 Angular averaging under magic angle spinning

It was demonstrated in the previous section how spatial distribution of the interacting spin pairs can be calculated by supressing fitting parameters from the CP kinetic curves and then performing Fourier transformation for extracted function. It was also shown how this leads to the fine structural details. Despite of that, the reasonable concern of the processing precision was recognised. The previously used processing approach rests on assumption that dominating dipolar coupling during cross-polarization is the one corresponding to the edges of Pake pattern (see Fig. 3.3). It is true that dipolar splitting is dominated by peaks appearing at $b_{jk}/2$, but nevertheless other values are present as well. This can lead to loss of information during processing of CP kinetic curves. Therefore, employed CP model must take into account dipolar coupling angular averaging.

Favourably, ammonium dihydrogen phosphate (ADP) is a compound that is well explored with XRD and ND techniques, hence the spatial distribution of different atom pairs is well known. In the present section the crystal structure will used to compare results obtained with two different CP processing routes to check precision of the developed method.

It is not surprising that the problem of using equation (3.22) for rotating solids has been already met and addressed. Therefore, it is better to begin with a model equation that already accounts for the angular averaging in the powdered material that is spun in magic angle. Cross-polarization kinetics then is characterized by the following equation[109,114]:

$$I(t) = \frac{1}{2}\left[\mathrm{e}^{\frac{-t}{T_{1\rho}}} - \mathrm{e}^{-k_1 t} g(t)\right] + \left(\frac{\langle S\rangle_{qe}}{\omega_{0,\mathrm{I}}} - \frac{1}{2}\right)\left[\mathrm{e}^{\frac{-t}{T_{1\rho}}} - \mathrm{e}^{-k_2 t}\right] \tag{4.9}$$

Here $\omega_{0,\mathrm{I}}$ is the Larmor frequency of I spins, S_{qe} is the quasi-equilibrium polarization of S spin inside the extended spin-system S–$\mathrm{I_N}$ that can be expressed by

$$\langle S\rangle_{qe} = \frac{N}{N+1}\omega_{0,\mathrm{I}} \tag{4.10}$$

In perfect isolated spin pair where $N = 1$ half of polarization is transferred to the S nuclei, and thus second term of (4.9) varnishes. The exponents with factor $T_{1\rho}$ and, similarly, exponents with factors k_1, k_2 correspond to spin diffusion in I spin reservoir. Essentially, polarization in quasi-equilibrium can reach up to full polarization of I spins ($N = \infty$) when there is a large quantity

of weakly coupled spins. Finally, function $g(t)$ expresses the angular average over all possible orientations and the CP behaviour in isolate spin pair:

$$g(t) = 1/2 \int_0^{\pi} \cos\left(\frac{2\pi b t}{2}\right) \sin(\theta)\, \mathrm{d}\theta \tag{4.11}$$

Note that integral above does not take into account spatial distribution, in other words it is an angular average for single b_{jk} value. Nevertheless, using previous assumptions of disorder, weak coupling it is trivial to conclude that this function to this limit approach gaussian function (3.23). Thus, additionally inserting (4.10) to (4.9) gives the following expression:

$$I(t) = \left[e^{\frac{-t}{T_{1\rho}}} - e^{-k_1 t} \cdot e^{\frac{-t^2}{2 T_2^2}} \right] + \left(\frac{N-1}{N+1}\right) \left[e^{\frac{-t}{T_{1\rho}}} - e^{-k_2 t} \right] \tag{4.12}$$

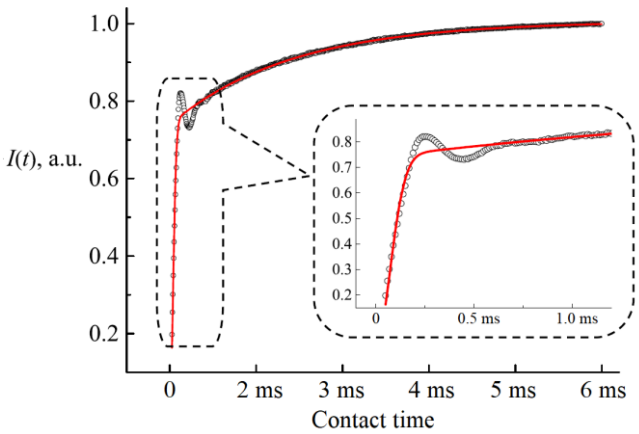

Figure 4.14. $^1H \rightarrow {}^{31}P$ CP-MAS kinetics in powdered ADP (7 kHz MAS, HH matching condition n = -1, room temperature). Fitting parameters of Eq. (4.12) are k_1=539±7 s^{-1}, (N-1)/(N+1) = 0.362±0.002, T_2 = 7.65±0.05, $T_{1\rho} \rightarrow \infty$, k_1 = 3/2 k_2 was kept fixed.

Non-linear fitting of previous function to CP data acquired for ammonium dihydrogen phosphate (ADP) gives a perfect global fit over all experimental points up to 10 ms. The ratio $k_1 = 3/2\ k_2$ was kept fixed as to assume isotropic spin diffusion (see Eq. (3.22))[19]. If the ratio is let to variate, unfortunately, the values of these parameters then are determined with the margins of error up to ±100%, without any significant improvement in χ^2 values. This means either the experimental data set was not ample to reveal the deviations from

the isotropic model or the isotropic spin-diffusion model is indeed adequate for the studied system.

It was already seen that fitting the global parameters gives good fitting results but fine details of initial oscillations in the CP are lost. Nevertheless, similar to equation (4.8) it is possible to leave only coherent oscillation in the CP kinetics:

$$I_{osc}(t) = \frac{f_3}{f_1} + \frac{N-1}{N+1}\left(\frac{f_3}{f_1} - f_1^{-1/3}\right) - \frac{I(t)}{f_1} \qquad (4.13)$$

where $f_1 = \exp(-k_1 t)$ is spin diffusion term, $f_3 = \exp(-t/T_{1\rho})$ term that relate to spin-lattice relaxation in rotating frame and parameter N is the number of inequivalent spin pairs which is also addressed as spin cluster. After omitting the global parameters, the left-over coherent part is shown in figure below.

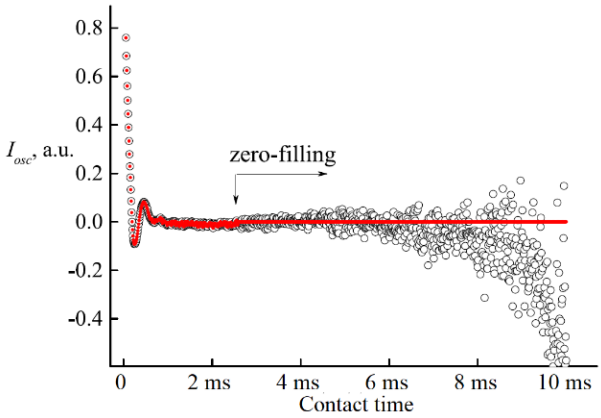

Figure 4.15. CP oscillatory term extracted using (4.13) with the fit parameters given in the caption of Fig. 4.14. The part with increasing noise was treated with zero filling.

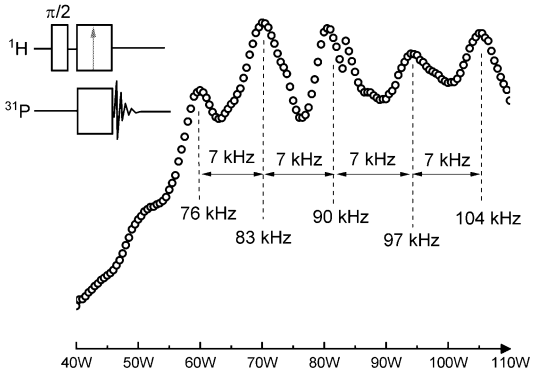

Figure 4.16. Hartmann-Hahn matching profile for $^{1}H \rightarrow ^{31}P$ CP-MAS. Inset shows variable parameter which is power of a pulse. It corresponds to a specific nutation frequency that is given below each maximum. Maxima are located at MAS (7 kHz) sidebands where the middle (90 kHz) is $n = 0$ matching condition.

Now, coherences appearing in CP time evolution (4.13) is a product not only of angular averaging but spatial average as well. Thereupon, full average can be written using equation (4.11):

$$I_{osc}(t) = \int_0^{\infty} \mathrm{d}b_{jk}\, P(b_{jk}) \int_0^{\pi} \cos\left(\frac{bt}{2}\right) \sin(\theta)\, \mathrm{d}\theta \qquad (4.14)$$

Angular part of the expression above is a periodic function due to magic angle spinning. Further on, as MAS splits Hartmann-Hahn matching into sidebands (Fig. 4.16), angular average will be different for each Fourier component of time dependant dipolar coupling. The reason why all experiments were performed under $n = \pm 1$ condition is that typically matching is best resolved in this condition (see figure above). Function $g(t)$ for $n = \pm 1$ Hartmann-Hahn condition is an angular average of $n = \pm 1$ Fourier component of dipolar coupling. Function has an integral form that can be expressed in Bessel functions of first kind:

$$g_{\pm 1}(t) = 1/2 \int_0^{\pi} \cos\left(\frac{\pi b_{jk} t}{\sqrt{2}} \sin 2\theta\right) \sin(\theta)\, \mathrm{d}\theta = J_0\left(\frac{\pi b_{jk} t}{\sqrt{2}}\right) + 2 \sum_{k=1}^{\infty} \left[\frac{1}{1-4(2k)^2} J_{2k}\left(\frac{\pi b_{jk} t}{\sqrt{2}}\right)\right] \qquad (4.15)$$

Note that index of the function now indicates the HH matching condition used. The table of $g(t)$ function can be found in ref 114.

To cope with the complexity of the expression above during processing would be a difficult task. To avoid overcomplicating the problem few assumptions can be made. Firstly, second term of the right-hand side in equation (4.15) decays rapidly because of the pre-factor in the summation and thus can be omitted. This only results in miniscule change (Fig. 4.17) which would be within margin of experimental accuracy.

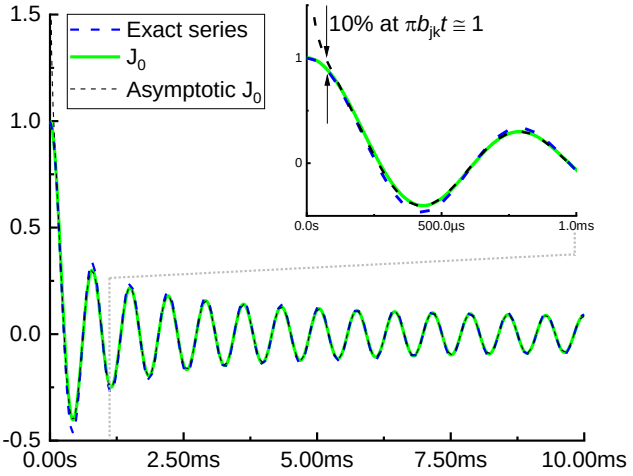

Figure 4.17. Exact series of Bessel function as in (4.15) and comparison to singular J_0 term and asymptotic $J_0(x)$, where $x = \frac{\pi b_{jk} t}{\sqrt{2}}$ and $b_{jk} = 4000$ Hz.

Therefore, neglecting higher order in the series gives a simplified spatial and angular average:

$$I_{osc}(t) = \int_0^\infty \mathrm{d}b_{jk}\, P(b_{jk}) J_0\left(\frac{\pi b_{jk} t}{\sqrt{2}}\right) = \int_0^\infty \mathrm{d}x\, \frac{P(b_{jk})}{b_{jk}} b_{jk}\, J_0\left(\frac{\pi b_{jk} t}{\sqrt{2}}\right) \qquad (4.16)$$

The right-hand side is rewritten to resemble Hankel transformation which can be used to find the profile $P(b_{jk})$ that no longer depends on angular effect, only on spatial parameter r_{jk}:

$$P(b_{jk}) \sim b_{jk} \int_0^\infty I_{osc}(t)\, J_0\left(\frac{\pi b_{jk} t}{\sqrt{2}}\right) t \mathrm{d}t \qquad (4.17)$$

The last important simplification is the use of asymptotic Bessel function. Asymptotically J_0 function is equal to hyperbolic cosine. However, as seen in figure 4.17 now mismatch with the whole series in the initial time steps.

Despite of that, asymptotic J_0 function aligns with the exact series when $\pi b_{jk} t \approx 1$ and under typical circumstances it corresponds to the first 100 μs. This means that this approximation is not valid for few initial data points of the recorded CP kinetics and also when the coupling is very weak. Hence, if few points of the data can be ignored then applying asymptotic J_0 leads to a following expression:

$$P(b_{jk}) \sim b_{jk} \int_0^\infty I_{osc}(t) \frac{\cos\left(\frac{\pi b_{jk} t}{\sqrt{2}} - \frac{\pi}{4}\right)}{\sqrt{\frac{\pi b_{jk} t}{\sqrt{2}}}} t \mathrm{d}t \tag{4.18}$$

Now, it is important to recognize, similarly as in (4.7), that this expression is linked to the real part of Fourier integral. After reordering variables and excluding constants from previous integral one would finally get to:

$$P\left(\frac{\frac{b_{jk}}{\sqrt{2}}}{2}\right) \sim \sqrt{b_{jk}} \int_0^\infty [I_{osc}(t)\sqrt{t}] \cos\left(2\pi \frac{\frac{b_{jk}}{\sqrt{2}} t}{2}\right) \mathrm{d}t \rightarrow \sqrt{b_{jk}}\, Re\{\widehat{FT}[I_{osc}(t)\sqrt{t}]\} \tag{4.19}$$

It means that purely spatial distribution can be obtained by applying Fourier transformation for $I_{osc}(t)\sqrt{t}$ with a proper rescaling. Again, dipolar coupling has to be rescaled additionally depending on the HH matching condition. Particularly, a factor of $\sqrt{2}$ is applied for $n = \pm 1$ which slightly simplifies the argument of function P rescaling in the previous equation[109].

The results of this processing of experimental CP-MAS kinetics (Fig. 4.14) including the recalculation of $P(b_{jk})$ from b_{jk}-variable to internuclear distances using (3.12) are presented in figure 4.18. To illustrate the sense of effectiveness of the developed treatment a comparison to a direct Fourier transformation of the CP kinetics was done. Interestingly, distribution obtain by direct Fourier transformation is similar to the radial function presented in the previous subsection (Fig 4.12). Nevertheless, the fine morphological details cannot be resolved using only straightforward Fourier transformation.

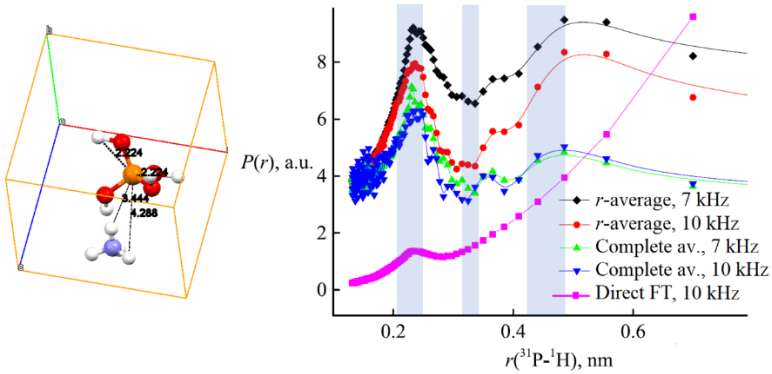

Figure 4.18. On the left – crystal cell of ADP and 3 characteristic P-H distances[115]. On the right – spatial distribution of protons surrounding ^{31}P nuclei in the powdered ADP at 7 and 10 kHz MAS obtained via different processing routes. Complete averaging is one presented in this section where spatial distribution takes into account orientations and distances, *r*-average, however, only accounts for the edge of Pake pattern (Fig. 4.10). The former approach was presented in the previous section. Pink line is a direct Fourier transformation of the CP kinetics, and transparent bars depict XRD and ND data.

The spatial distribution profiles consist of 3 maxima at 0.234-0.239 nm, 0.357-0.376 nm and at 0.476-0.507 nm depending on the processing route. These distances can be compared with existing crystallographic data (see Table 2). Typical P-O-H distances in other phosphate compounds like CaHA or phosphonic acids is ~0.21-0.25 nm[22,28,102,107]. The shortest distance can be told to be the most precise for the following reasons: (i) this peak is best resolved even without additional processing since (ii) it relates to the strongest coupled spin pair (b_{jk} ~4 kHz) and hence $\pi b_{jk} t \geq 1$ is valid for all data points.

Table 2. Maxima position in [nm] of the spatial distributions of protons surrounding ^{31}P in powdered ADP and a comparison with ND and XRD data.

Method	Peak 1	Peak 2	Peak 3
7 kHz MAS, r-average	0.239	0.376	0.507
10 kHz MAS, r-average	0.237	0.376	0.507
7 kHz MAS, complete av.	0.234	0.364	0.476
10 kHz MAS, complete av.	0.236	0.357	0.479
Neutron diffraction [115,116]	0.219-0.22	0.330-0.344	0.476-0.444
X-ray diffraction [31,32,116]	0.235-0.244	0.329-0.335	0.430-0.441

The shortest peak obtained from the processing of the $^{1}H \rightarrow ^{31}P$ CP kinetics has value between ND and XRD data values, whereas those for more remote protons are slightly larger. It is clearly seen in the Fig. 4.18 that resolution and intensity of remote spin maxima is worse. However, it can be stated that complete averaging slightly increases the resolution of spatial resolution of the remote spins. These results could be considered as a certain step towards crystallography because using the present method one directly measures radial distribution between interacting spins. Techniques like ND and XRD do not provide radial distribution of such atom pairs and thus distances are estimated. Therefore, CP is not only precise, but it is complementary solution to many crystallographic problems.

Since ammonium dihydrogen phosphate is a model system, it can be useful to track the performance of the used CP technique in variable conditions, say, temperature. Therefore, measurements at different temperatures were performed using magic angle spinning rate of 7 kHz. Obviously, temperature dependent parameters like repetition delay was changed accordingly as well. The results are shown in figure 4.19.

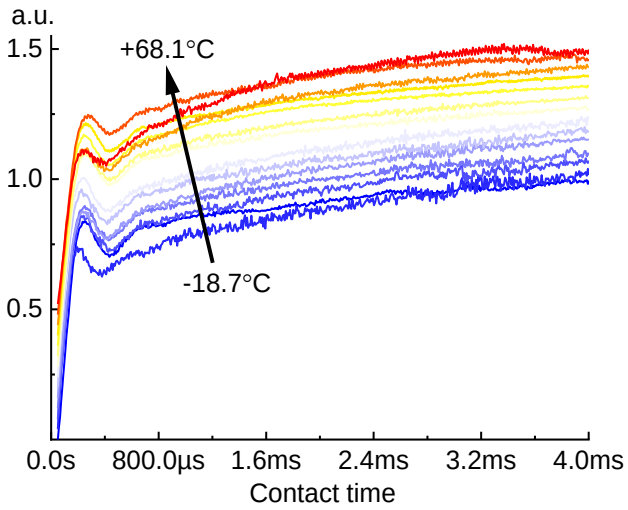

Figure 4.19. $^{1}H \rightarrow ^{31}P$ CP-MAS kinetics in powdered ADP (7 kHz MAS, Hartmann-Hahn matching condition $n = \pm 1$) in the temperature range from −18.7°C to +68.1°C. Temperature was calibrated using lead nitrate sample. Slight offset for curves was set for clarity.

Just from visual inspection of CP kinetics depicted in the figure above it seems that changing temperature does not have a large effect on cross-polarization

kinetics. Nevertheless, as processing of the CP kinetics can detect even miniscule change, it is worth to extract spatial distribution. The results indicate a change of the distance between ^{31}P and ^{1}H under changing temperature (Fig. 4.20).

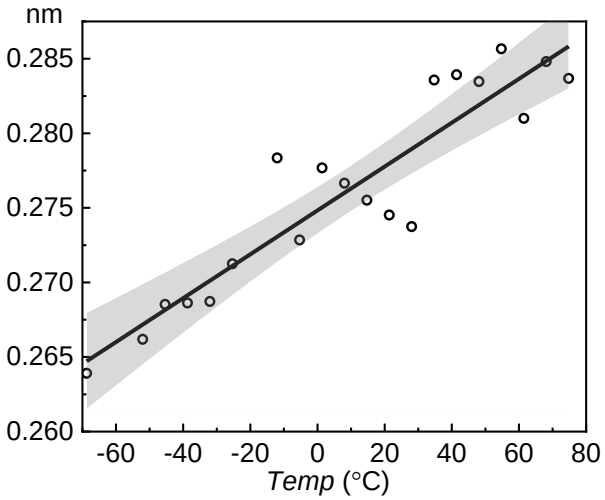

Figure 4.20. The impact of temperature change to internuclear distance ^{31}P-^{1}H. Each point acquired after processing of the CP kinetics and fitting Gauss function to the distribution maximum. Temperature was calibrated using lead nitrate sample. Grey area depicts 98% confidence band of linear fitting.

Linear fitting predicts that internuclear distance depends on temperature with a rate of 0.147±0.014 Å/100K. However, it is hard to state that since it gets into the polemic in ref 115, where variation of the P–O distance was discussed, however, rejected suggesting that the results of the earlier XRD studies were not sufficiently accurate for valid comparison at different temperatures. The inclusion of crystallographic data from more recent works has brought not too much clarity. The values of the essential P---H distances analyzed in the present work taken from the experiments carried out in the range from room temperature down to 152 K are irregularly spread within ~0.1 Å as those from ND as well as XRD (Table 2).

Additionally, non-linear fit (4.12) over all kinetic curves provided with the effective spin cluster size N and spin diffusion k_1 (k_1=3/2k_2). Spin cluster size was found to be 2-4 and k_1 about 500 1/s with only a slight dependency to temperature. Thus, no significant changes in ADP structures are expected.

It important to comment that even if the processing of the CP kinetics accounts for spatial and angular averaging, profiles depicted in Fig. 4.18 will never be "true" distributions. The main reason is that spin diffusion and relaxation will always lead to decaying CP oscillations. This is the origin of the natural linewidth. Even after taking into account ~500 1/s spin diffusion rate and relaxation, the homogeneous broadening in the obtained distributions is be still considerably large. It could be then linked to thermal motion or thermal ellipsoid of the atoms in the lattice where position of light atoms is a large distribution. However, it only reinforces the fact that true distribution would be hidden by broadening effects. Despite of this rather semantic obstacle, the term "distribution" will be maintained throughout the work, since it is the most descriptive way to relate apparent maxima in the acquired intensity *vs.* spatial coordinate plots. It is also useful to remember, that in spectroscopy or microscopy broadening effects always occur, thus, all distributions are also superposition of maxima with natural linewidths associated with them.

As pointed out previously the presented results can be considered as a certain step developing NMR crystallography for complex solids, however, moving not via the traditional analysis of chemical shifts and spin coupling tensors, but in a complementary way through the kinetics of CP transfer. In future this method can be useful creating the series of novel materials via control of their structural details in the sub-nano scale as well as monitoring and correlating the short-range order effects with macroscopic properties, like, strength, flexibility, and phase behavior.

Conclusions of section 4.3

- Spatial and angular average was performed using Hankel-Fourier transform, which granted with purely-spatial distribution of cross-polarization partners ($r(^{1}H\text{-}^{31}P)$).

- The obtained spatial distribution contacts in ammonium dihydrogen phosphate are within good agreement to those found in crystallographic database. Thus, the method has sufficient precision to supply with complementary crystallographic information.

4.4 CP in organic materials

In many aspects, CP and spin equilibration processes demand to consider spin systems as open or not exactly closed quantum systems. These equilibration processes could vary depending on the spin system. Organic materials are interesting systems for they yield large variety of chemical groups as building blocks. Carbons and protons are the main available CP partners in most of organic molecular systems. The large differences in the polarization transfer kinetics between adjacent (directly bonded) $^{13}C-^{1}H$ pairs and from remote protons have been observed before[18,117]. This is challenging as it requires further developments in the theoretical spin coupling models. The following sections will discuss CP dynamics in various organic compounds in the following way. First, with respect to figure 3.24, where coupling regions are denoted, strong coupling cases will be analyzed first. Then, intermediate coupling and weak coupling examples will be presented.

4.4.1 Adjacent and strongly coupled spins

Glycine (Fig 4.21) is a very suitable and promising test-system for these purposes. It is one of the simplest compounds containing two very distinct chemical groups with very different $^{13}C-^{1}H$ coupling. The CH_2 group is the first one. The CP kinetics is governed by the strong interaction between ^{13}C and two adjacent protons. The second subsystem can be identified around the carboxyl carbon (COOH, or COO^- in the zwitterionic form). Its extent, in other words − spin cluster size, is not clearly defined. Thus, the CP process can cover the interactions only with closest intramolecular protons. As a result, behaviour under CP should be different. Therefore, it is worth to elucidate on these features.

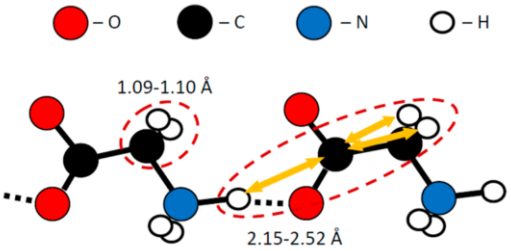

Figure 4.21. Essential internuclear distances between C and H atoms in crystalline α-glycine according to the neutron diffraction data (refs in 20).

Glycine, like ADP was extensively analysed with ND and XRD techniques, therefore the internuclear distances are well known. In the gas phase glycine exists as a neutral molecule (NH_2CH_2COOH), whereas in aqueous solution at normal pH as a zwitterion ($NH_3^+CH_2COO^-$)[118]. The crystallographic structure and geometry of glycine has been well examined by X-ray (XRD) and neutron diffraction (ND) experiments[20]. In the solid state it exhibits three polymorphic forms with relative stabilities: $\gamma > \alpha > \beta$. The three glycine polymorphs differ in the packing of the zwitterions. The essential internuclear distances between C and H atoms are summarized and presented in Figure 4.21. These are necessary to analyse the spin coupling. This mapping is based on ND data. The importance of ND lies in the accurate determination of hydrogen positions.

The experimental $^1H \rightarrow ^{13}C$ CP-MAS kinetic curves for the CH_2 spin system (Fig. 4.22) were processed applying Eq. (4.12) with the constraint of isotropic spin-diffusion ($k_1/k_2 = 3/2$) and Eq. (3.24) (further called the λ-model). The results of fitting are given in Table 3.

Now, recall equation (4.12) which can be slightly rewritten as

$$I(t) = I_0 \mathrm{e}^{-t/T_{1\rho}} \frac{N-1}{2N} \left[1 + \frac{N-1}{2N} \mathrm{e}^{-k_2 t - t/T_{1\rho}} - \frac{N+1}{2N} \mathrm{e}^{-k_1 t - t/T_{1\rho}} \cdot \mathrm{e}^{\frac{-t^2}{2T_2^2}} \right] \quad (4.20)$$

The reason for this rearrangement is the following. Let's assume that k_1, $k_2 >> 1/T_{1\rho}$ and $N/(N - 1)$ is a normalization factor. Then one will obtain equation (3.24) where parameter λ is different:

$$\lambda = \frac{N-1}{2N} \quad (4.21)$$

Note that this is different than original $\lambda = 1/(N + 1)$. For infinite spin-clusters ($N \rightarrow \infty$) the new λ parameter reaches its maximal value of ½ and provides an additional constraint on the fitting of CP kinetic curves. Thus, it is not surprising that parameter values obtained applying both (3.24) and (4.12) models gives identical parameters. Therefore, both equations share common features like parameter (4.21) if the isotropic spin diffusion is assumed.

It is gratifying to state that very realistic values of the spin-cluster size (N) have been obtained for all used MAS rates without any constraint on the flow of the nonlinear curve fitting ($\chi^2 \rightarrow$ *minimum*). The deduced values $N \leq 3$ (Table 3) can be recognized as the "effective" number of spins I (protons) interacting with the CH_2 carbon, namely – two adjacent protons and a certain contribution from the remote protons in glycine molecule.

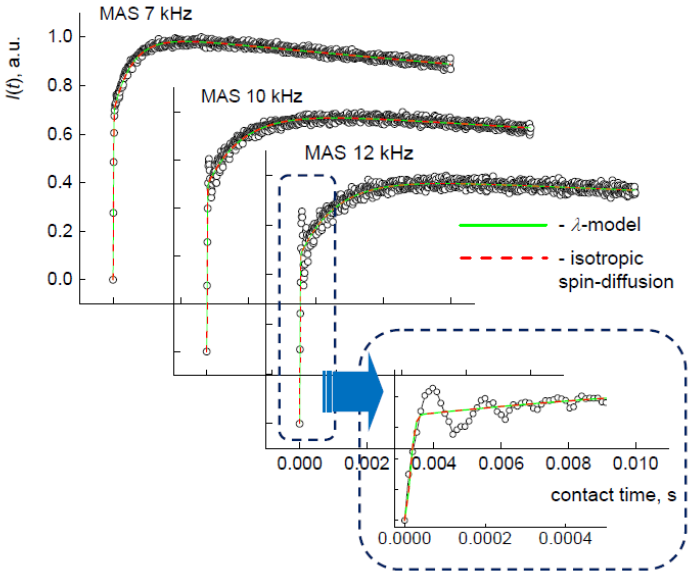

Figure 4.22 Experimental $^{1}H \rightarrow ^{13}C$ CP-MAS kinetic curves of glycine CH_2 spin system at various MAS rates. The last curve was fitted with the isotropic spin-diffusion model and λ-model (equations (4.12) and (3.24), respectively). The fitted parameters are given in Table 3. A "smoothing" of the coherent oscillatory behaviour due to a Gaussian decay approach for $g_n(t)$ is shown in the inset (short contact time, <0.5 ms). More comments are given in the text.

Table 3. Fit parameters of $^{1}H \rightarrow ^{13}C$ CP-MAS kinetics for CH_2 spin system. Obtained using isotropic spin diffusion and λ-models (eq. (4.12) and (3.24)) as in first row and the second, respectively.

***MAS rate*, kHz**	**7**	**10**	**12**
N	2.93±0.05 3.22±0.05	2.83±0.05 2.87±0.05	2.87±0.07 2.30±0.04
λ	0.330±0.003 0.33±0.003	0.323±0.003 0.325±0.003	0.326±0.004 0.282±0.004
k_2, s^{-1}	1790±30 1730±20	900±20 950±20	920±30 900±30
T_{dif}, ms	0.56±0.01 0.58±0.01	1.12±0.03 1.06±0.03	1.09±0.04 1.11±0.04
T_2, μs	12.8±0.2 12.3±0.2	13.1±0.3 12.4±0.3	12.8±0.4 12.7±0.4
$T_{1\rho}$, s	0.073±0.001 0.077±0.001	0.114±0.005 0.16±0.01	0.16±0.01 0.25±0.03
χ^2	$8.7 \cdot 10^{-5}$ $8.0 \cdot 10^{-5}$	$2.0 \cdot 10^{-4}$ $2.4 \cdot 10^{-4}$	$3.9 \cdot 10^{-4}$ $3.8 \cdot 10^{-4}$

The non-linear curve fitting was carried out setting the function $g_n(t)$ as a Gaussian decay. As already presented, this is a good approximation for long contact times and serves a good tool from global parameter fit. Its application for the whole CP kinetic curve leads to a certain loss – it partially "smoothes" the coherent oscillatory behavior of the CP intensity in the initial stage of polarization transfer (short contact time, < 0.5 ms, see the inset in figure 4.22). However, this situation can be exploited separating the pure coherent contribution to CP from the incoherent one. It is reasonable to assume that the fitting residuals are mainly originated from the rest of the coherent contribution that survives after the incoherent part is subtracted. The Fourier transform over the CP intensities $I(t)$ acquired at 12 kHz MAS and over the corresponding residuals are shown in figure 4.23.

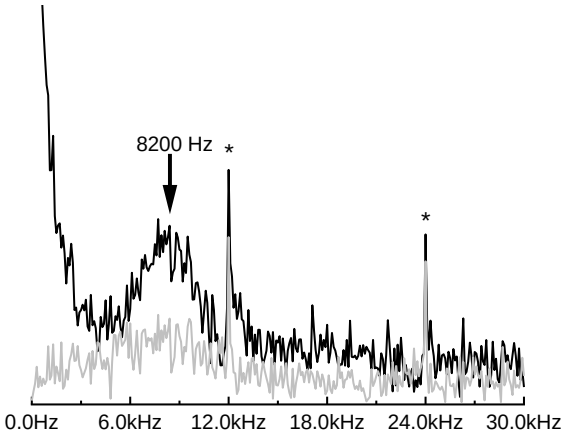

Figure 4.23. Direct Fourier transform of the CP kinetics (black line) and of the fitting residuals (grey line). The peaks related to periodic quasi-equilibrium observed at multiples of the MAS frequency (12 kHz and 24 kHz) are marked by asterisks.

The strong narrow peaks were observed at multiples of the MAS frequency (12 and 24 kHz). Such peaks have been observed in other systems (ferrocene, alanine) and considered as the confirmation of the existence of a periodic quasi-equilibrium state[99]. This state is expected to have a lifetime related to $T_{1\rho}$, which is indeed much longer than the time scale of spin-diffusion for CH_2 in glycine (see $1/k_2$ or T_{dif} in Table 3). Hence, the Fourier transformations nicely confirm the coherent nature of the quasi-equilibrium states – the subtraction of incoherent contribution practically does not influence on the intensities of peaks at 12 and 24 kHz, whereas the other intensities in the distribution of b around ~8200 Hz were significantly reduced.

The broad contour at ~8200 Hz characterizes the strength of $^{13}C–^{1}H$ dipolar coupling and the degree of local order due to the internal motion in glycine molecule. The local order parameter $\langle S \rangle$ is defined as the ratio of the experimental dipolar coupling constant and the calculated rigid limit dipolar coupling constant[119]. In the present case the coupling constant b_{jk} was determined to be ~23.2 kHz (2×8200 Hz, rescaled by the factor of $\sqrt{2}$ due to HH matching condition $n = \pm 1$[109]) is roughly equal to the static constant 23.0 ± 0.3 kHz for the rigid C–H bond (where $r_{C–H} \sim 1.09–1.10$ Å). Hence, the local order parameter $\langle S \rangle \approx 1.0$. This value fits well to those measured in alanine at room temperature and glycine at −45°C (0.98 and 1.03, respectively)[119].

However, it should be noted that the precise determination of the local order parameter ⟨*S*⟩ meets some serious difficulties. This is because the *b* values obtained processing CP kinetics are strongly affected by several factors. The influence of the MAS rate and the presence of water as contaminant is shown in figure 4.24. No features of dipolar coupling are seen in the *b*- distribution at the spinning rate of 7 kHz. The broad contour due to $^{13}C–^{1}H$ couplings appears at ~7200 Hz using 10 kHz MAS, and it shifts to 8200 Hz as the spinning rate reaches 12 kHz.

This effect can be explained by decimation of spin interactions upon MAS[21]. It was shown in section 4.3 (see Fig. 4.4) that MAS technique fails to suppress anisotropic spin interactions fully, if rapid internal dynamics is present in the spin system. The line intensities and widths upon MAS become dependent on the spin interaction strength, the time scale of the motion and the spinning rate. The static *b*-distribution is formed overlapping all possible contributions from spin interactions in the system. The broad contour appears as the weakest spin interactions with the most remote protons are suppressed. This component is centered at *b* ~0 Hz. It looks that for glycine it happens at ~10 kHz MAS rate (Fig. 4.24). The further increase of the MAS rate (up to ~12 kHz) leads to the suppression of "intermediate" contributions, e.g. from NH_3^+ protons, characterized by the dipolar coupling $0 < b < 1200$ Hz. The maximum of resulting contour shifts then to the position typical for the "frozen" C–H bond at ~8200 Hz, and thus the "true" local order parameter ⟨S⟩ ≈ 1.0 was deduced.

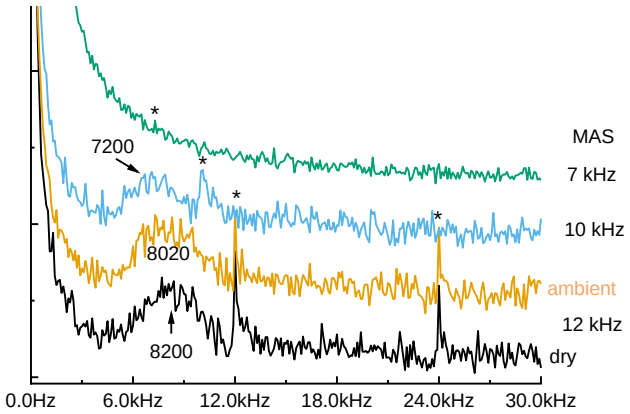

Figure 4.24. The MAS rate and the presence of water as the factors that influence the observed dipolar splitting after FT of the CP kinetics.

The influence of contaminant water is not crucial as it is smaller than the effect of overlapping couplings. It was evaluated comparing the results obtained for the samples prepared under ambient conditions and additionally dried under vacuum (degassing + heating). The *b* value for the center of the contour ~8020 Hz for the sample prepared under ambient conditions (Fig. 4.24) would cause a slightly corrupt picture of the local ordering ($\langle S \rangle \approx 0.98$).

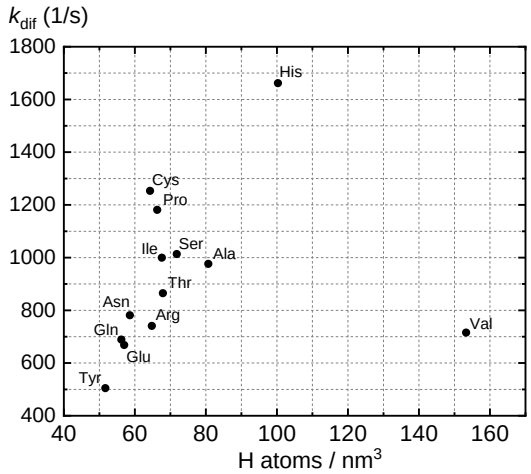

Figure 4.25. Spin diffusion rate k_{dif} *versus* the density of hydrogen atoms in different amino acids. Crystal packing was calculated using crystallographic data[120,121,130,122–129].

Perhaps the knowledge of order parameters in neat amino acids is not particularly important but it grants with *a priori* information designing other molecules or even in the research of proteins where amino acids can be related to special functional parts. However, fitting parameters can give some additional insight. It was apparent in the Table 3 that isolated-spin pair model (Eq. (4.12)) is valid for adjacent spins with strong coupling. The fitting parameters are quite unique for each molecule, but some tendencies can be found.

Spin diffusion, for example is a process that is also related to the dipolar coupling but between nuclei of the same species. The shorter are distances to each *I* spin (in present case proton), the faster is spin diffusion. Thus, increasing the density of hydrogen in the structure should increase the spin diffusion. This is what the figure 4.25 elucidates. Hydrogen atom density was calculated for each amino acid from chemical formula and crystal packing obtained in XRD and ND crystallographic database. With an exception of

valine (Val) it was observed that spin diffusion tends to increase with the higher density of abundant ^{1}H spins. The overall spin diffusion rate k_{dif} was calculated by taking an average of all k_2 parameters (Eq. 4.12) for all of chemical sites except weakly coupled carboxyl. To reduce number of variables isotropic spin diffusion (k_1=3/2k_2) was assumed.

The explanation why a point corresponding to valine is out of track is the following. The molecule of valine has two methyl groups, and, in fact, these groups make up 67% of all hydrogen atoms in it. This means that majority of ^{1}H nuclei in valine experience rapid reorientation due to methyl group rotation. This is a transition to the next subsection were effect of motional average will be discussed. As spin-diffusion in I spin bath is specified by the effective dipolar I-I coupling, it will be strongly affected by rapid rotations too. Despite scattering of the data points, the tendency (Fig. 4.25) to the best knowledge has been experimentally observed for the first time.

4.4.2 Methyl group in amino acids. Apodization and intermediate coupling regime

Organic solids are made of packed molecules, hence distances between atoms in short-range are defined by bond-lengths. Bond-lengths under normal conditions do not vary much, meaning that spatial distribution of atoms is not that interesting. However, depending on shape, size and other properties, molecules may yield addition freedom for some reorientations. Therefore, motional averaging can introduce rescaling of the measured dipolar coupling. It is not surprising, that such effect is used to probe molecular structures like, for example, proteins and their internal order relating to mobility[119]. Unfortunately, in the framework of cross-polarization, it means that initial oscillations in the kinetics will have lower frequency and due to spin diffusion will be less resolved. Hence, processing options to enhance these frequencies would be very welcome.

Alanine is a molecule as simple as glycine but it has additional methyl group. Hence, alanine is compound where three distinct chemical groups are present were dipolar coupling coupling is strong, weak and intermediate. This is illustrated in figure 4.26 where three distinct CP kinetics are shown. The reasoning why methyl group is intermediately couple will be soon given.

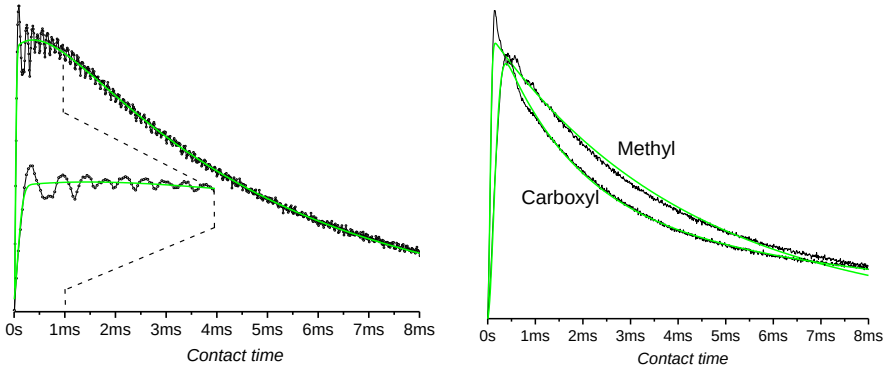

Figure 4.26. $^{1}H \rightarrow ^{13}C$ cross-polarization kinetics at the $n = 1$ Hartmann-Hahn condition. On the left-hand side – CP transfer to C_α and a zoom to emphasize on the oscillations, on the left – CP build-up curves in methyl and carboxyl groups. Green lines represent global fit using equation 4.12.

Obviously, it is not hard to find dipolar coupling of strongly coupled spin pair as ^{1}H-$^{13}C_\alpha$ even by straight forward Fourier transform on the CP kinetic curve. The result would be similar to figure 4.24 where small maximum is seen at the foot of a broad 0 Hz feature originating from exponential decay. Due to this feature maxima stemming from the methyl and carboxyl groups are hidden after direct FT. This can be seen in figure 4.29.

Now, it is good to start from the section 4.3 where special processing is applied to extract only oscillatory (coherent) part of the CP, moreover, depending only on spatial distribution. Also, it has been concluded that one can use Eq. (4.12) as a proper model to fit global spin system parameters allowing to decimate them. The global fit is depicted as a green line in figure 4.26. Subtraction of all fitting parameters using Eq. (4.8) results in residuals shown in figure 4.27.

Note, how signal-to-noise ratio increases drastically with time. This is a side product of Eq. (4.8) because decayed exponents become fractions of infinitesimal number, meaning that outcome will diverge to infinity. With the example of ADP (Fig. 4.14) it was demonstrated how this problem can be addressed with a common treatment of zero filling.

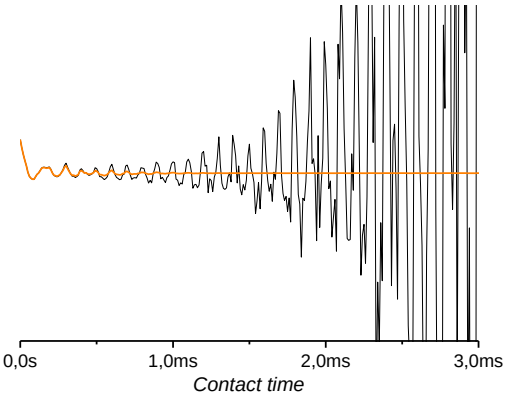

Figure 4.27. Oscillatory term ($I_{osc}(t)$) after extraction using global fit (Eq. 4.12) and Eq. 4.8. Orange line depicts the same term affected by apodization function.

It involves deleting elements from certain point where oscillations have decayed and adding zeroes. Zero filling essentially increases resolution as it reduces the amount of noise used in the data processing. Yet another common technique in the field, especially dealing with signal-to-noise ratio, is apodization. It is done by multiplying raw data points with a function, typically, Gaussian, to enhance points at the beginning and to suppress the ending where most of the noise is expected. Remember that zero filling is also a type of apodization function where the function can be considered square. The effect of apodization on I_{osc} is shown in figure 4.28.

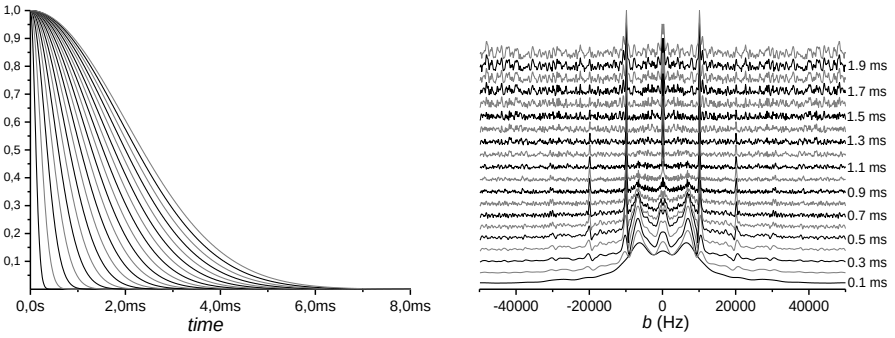

Figure 4.28. Apodization function with variable Gaussian width (on the left) applied for data points seen in Fig. 4.27. The multiple Fourier transforms of the outcome – on the left. The example is the CP of H-C_α spin pair.

Not surprisingly, very short Gaussian function results in a loss of resolution and information whereas too long Gaussian decay will include most of the noise of the data. Thus, interactive processing must be used, where the user needs to define the best achievable outcome. This process adds rather "draggy" aspect for the whole processing route but taking into account modern computing speeds it can be done quickly. The achieved resolution is best underlined with a comparison to a direct Fourier transformation of the cross-polarization kinetic curves in figure 4.29.

Naturally, least surprising is the result where the strongly coupled spin pair (H-C_α) under CP yield such strong oscillation that the frequency can be obtained even after straightforward Fourier transform of the CP kinetics. Despite of that, using the current processing routine the broad 0 Hz feature is supressed almost completely hence the resolution of the dipolar splitting spectra is enhanced. Even more welcome result is the apparent dipolar splitting for the intermediately (methyl) and weakly coupled (carboxyl) groups (see Fig. 4.29). Using a straightforward FT for these kinetics does not give any information about the dipolar coupling, whereas using present technique one can see well resolved splitting. Thus, apodization of the I_{osc} term not only increases the resolution but significantly improves the quality of the technique.

However, note of warning has to be made. Using CP models to fit parameters for further processing sometimes may lead into residuals (for example, see Fig. 4.27) that may look like oscillations where actually they are not. Applying FT to them would unmistakably result in some peaks that are artefacts instead of being real. All of the dipolar splittings shown in Fig. 4.29, however, can considered real since oscillatory behaviour can be seen without any processing in the "raw" kinetics of alanine. Nevertheless, one has to be cautious interpreting dipolar spectra for weakly coupled system where complex modelling may result in oscillatory-looking residuals.

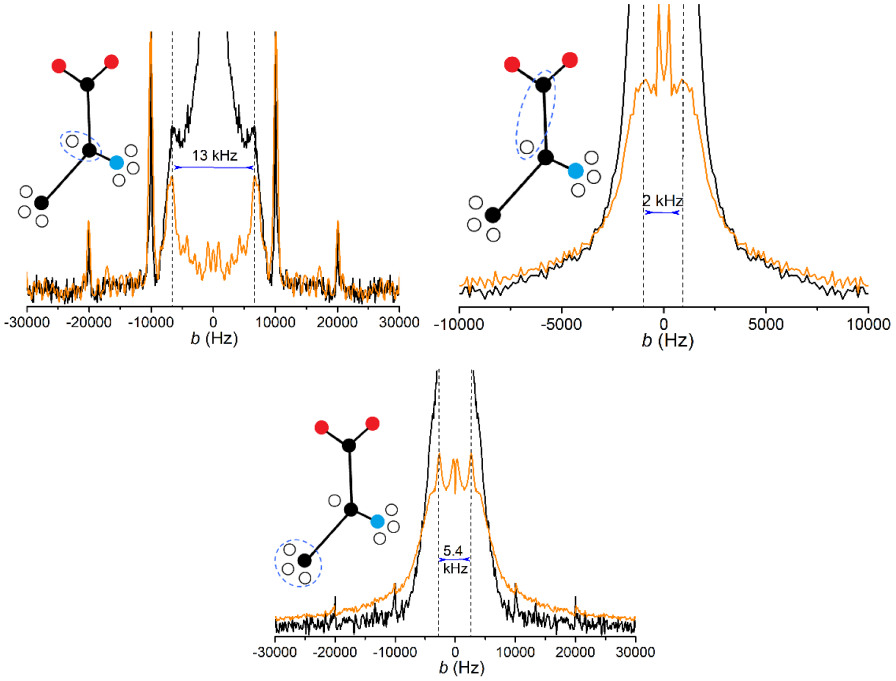

Figure 4.29. The comparison between obtained *b*-spectra using direct Fourier transformation of CP kinetics (black line) and Fourier transformation of processed I_{osc}(t) multiplied by apodization function (orange line). Blue circles and lines indicate spin pair and dipolar splitting in that pair.

This processing routine was tested on various amino acids which led to the same conclusions as before although a special attention to a methyl group must be given. It has been observed using the presented processing routine that dipolar splitting for methyl group is almost invariant (figures 4.29 and 4.30). Note that these patterns would not be achieved without using apodization function. This observation leads to interesting to an insight

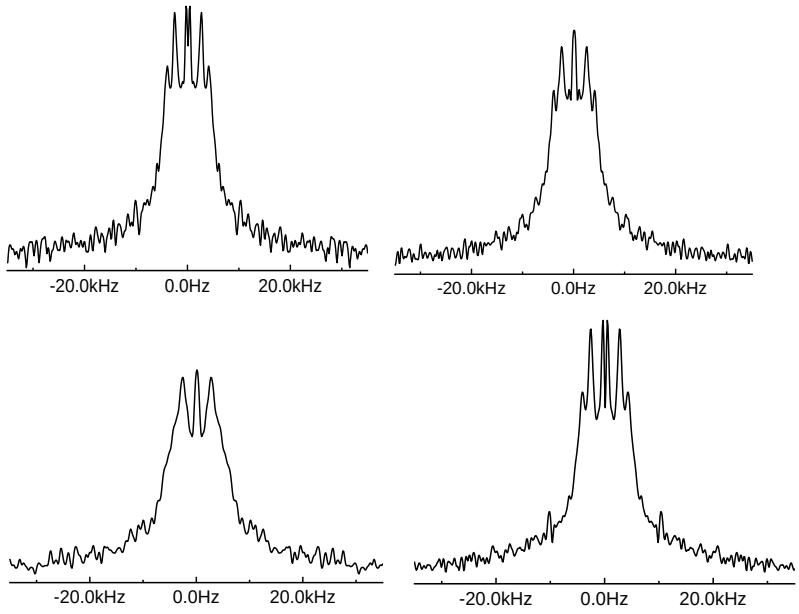

Figure 4.30. The dipolar coupling of the methyl group spectrum calculated using presented processing route in various amino acids. Top – L-valine, bottom left – L-isoleucine, bottom right – L-threonine.

It has been mentioned already that organic compounds (although not necessarily) often yield some freedom to motion that introduce consequent averaging effects. This parameter could be easily linked to another also known as order parameter. Orientational order parameter is an time average of non-restricted reorientations that can be expressed in the following way[119,131]:

$$\langle S \rangle = \frac{b_{CH}}{b_{rigid}} = \langle P_2(\cos \alpha) \rangle \tag{4.22}$$

where α is the angle of the instantaneous orientation of the dipole-dipole coupling tensor with respect to the "symmetry axis of fast motion". However, freedom of motion in methyl group is slightly different. At room temperature three hydrogen atoms are usually allowed to rapidly undergo fast rotation around the C-C bond axis. Therefore, ^{1}H-^{13}C spin pair mimics a rotation in the angle of tetrahedral angle 109.5°. Then the order parameter according to Eq. (4.22) is ⟨S⟩ = 0.33 meaning that the observed dipolar coupling value would be the real (rigid) dipolar coupling b_{jk} multiplied by factor of 0.33. Therefore, as the splitting patterns are quite similar it can be stated, that C-H bond length is indeed quite constant.

Now, one needs to recall figure 4.24 where various effects on dipolar splitting was observed. Not going into details, one needs to account that observed dipolar coupling may be shifted due to various effects like ambient water, insufficient MAS spinning rate. Hence, the true internal standard would allow to ignore this uncertainty. Thus, assuming that C-H bond length and tetrahedral angle are almost invariant, methyl groups can be used as an internal standard to measure dipolar coupling within a molecule to probe mobility excluding unwanted effects, say, due to insufficient MAS. A comparison with and without using methyl groups as an internal standard is shown in the Table 4.

Table 4. Local order parameters in different chemical groups of amino acids obtained by using methyl group as a standard (upper row) and using ratio with typical dipolar coupling of 23 kHz (lower row).

Amino acid	⟨S⟩			
	Methyl groups	C_α	C_β	C_γ
L-Ala	0.33 0.32	0.86 0.83		
L-Val	0.33 0.32	0.91 0.87	0.97 0.93	
L-Thr	0.33 0.33	0.80 0.79	0.86 0.84	
L-Ile	0.33 0.32	0.88 0.85	0.83 0.81	0.90 0.88

Fixing methyl group order parameter to ⟨S⟩ = 0.333 gives slightly elevated values for the other groups in amino acids. Lower values obtained by using standard dipolar coupling constant of 23 kHz indicates that results may be affected by insufficient spinning speeds or ambient water contamination (see Fig. 4.24). Therefore, larger values may be more believable bearing in mind that small molecules like alanine, glycine typically form rigid structures.

It has been extensively shown that under rapid reorientations *i.e.* freedom to motion, dipolar coupling is averaged by the factor which is commonly associated as order parameter. This section will exploit few examples where such averaging could be expected. Normally discorded, flexible structures go into category of so-called soft solids. Solids also tend to lose rigidity if the when bigger molecules pack.

For this reason, few tripeptides were analysed. In order to avoid unwanted effects due to water or insufficient spinning, two tripeptides – GGG (glycylglycylglycine), GFG (Glycine-Phenylalanine-Glycine) where packed in the glovebox and spun at the rate of 12 kHz. Then CP kinetics under usual conditions were measured (HH match $n = \pm 1$, high RF) and Fourier transforms of these kinetic curves were made without additional processing. Additional processing was not required since dipolar coupling was still found to be strong.

Firstly, glycine being the simplest amino acids can form the simplest tripeptide GGG. The results in figure 4.31 can be compared to the results of neat glycine in figure 4.23. Remember, that to get b_{CH} from Fig. 4.23, one needs to multiply 8200 Hz by factor of 2 and $\sqrt{2}$ due to HH matching condition of $n = 1$. This would give value of 23.2 kHz and it can be compared to those that obtained from GGG CP kinetics.

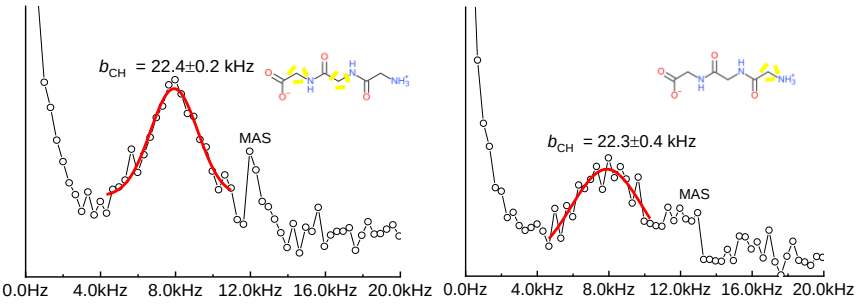

Figure 4.31. The dipolar coupling peaks of GGG tripeptide after direct Fourier transformation of CP kinetics at $n = 1$ Hartmann-Hahn condition. Sites associated with the maxima are marked in yellow. Assignments were based on data from Spectral Database for Organic Compounds (SDBS).

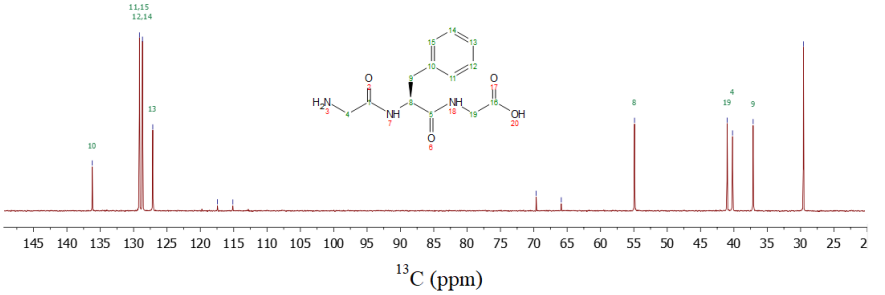

Figure 4.32. The ^{13}C NMR peaks assignment of tripeptide GlyPheGly. The data acquired and processed by M. Brodrecht (TU-Darmstadt).

It is clear, that the order parameter $\langle S \rangle > 0.9$ indicates that this molecule is still considerably rigid as reorientations are restricted. Although, order parameter for the end of the peptide is a bit lower but the deference is still at the order of the error margins. This result is not surprising as GGG is still considerably small molecule without any special groups.

On contrary, the case for GFG peptide where the middle monomer of glycine is changed to phenylalanine, is rather different. Before CP experiment, the peak assignment was used which was based on liquid-state NMR measurements done in TU-Darmstadt, Germany (see Fig. 4.32). The high resolution seen above is obviously not achievable in solid-state due to broadening effects described in 3 chapter. Due to broadening many peaks will overlap such that individual chemical shift of the site will be hidden. The consequence is that peaks are then associated with the several sites. This is why in the figure 4.33 dipolar coupling spectra are corresponding to several spectral sites.

The dipolar splitting values obtained in the tripeptide GFG sample (Fig. 4.33) imply interesting properties of the aromatic groups. The order parameter $\langle S \rangle$ drops from 0.92 to 0.86 from the end of the molecule to the middle, and it even reaches 0.51 in the aromatic ring. Therefore, freedom to random can induce reorientations to other sites if the origin of reorientation is not rotation. This insight and way of probing could be a promising tool designing functional molecules. Unfortunately, method does not allow to sense the origin of reorientations and it has to be done using *a priori* knowledge or logical assumptions like for rotating methyl group. The lack of rigidity (or rather flexibility) can be associated with flexible groups that are most commonly found in polymer systems.

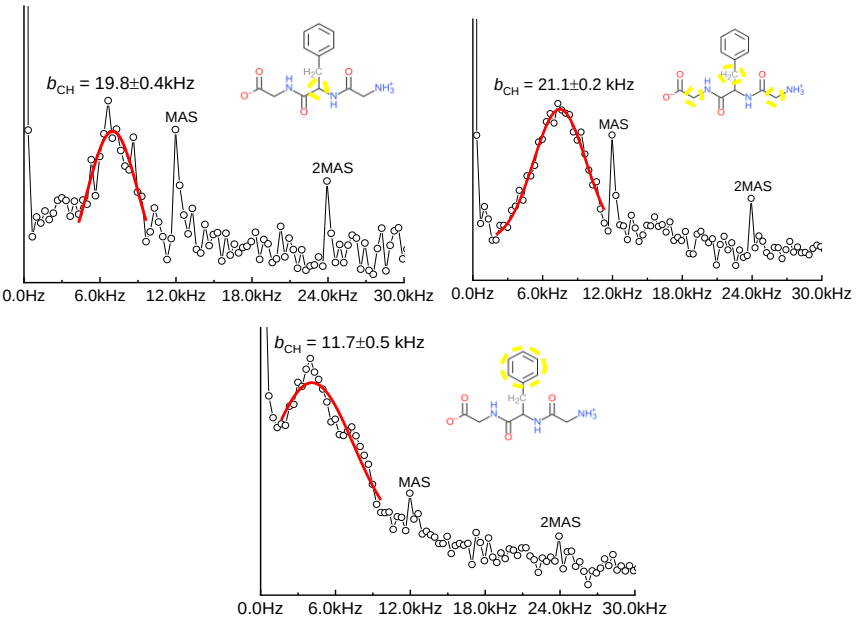

Figure 4.33. The dipolar coupling peaks of GFG tripeptide after direct Fourier transformation of CP kinetics at n = 1 Hartmann-Hahn condition. Sites asociated with the maxima are marked in yellow.

Therefore, investigations were also carried out on a polymer system, namely poly-(2-hydroxyethyl methacrylate) (pHEMA). The ^{13}C signals in the neat pHEMA were identified employing 2D ^{1}H–^{13}C HETCOR spectrum and confirmed by DFT results (Fig. 4.34). On contrary to GFG tripeptide, lines seen NMR spectra corresponded to each chemical site. However, the assignment had to be done using heteronuclear correlation technique (see section 3.5). Additionally, DFT calculations were used to confirm the assignment.

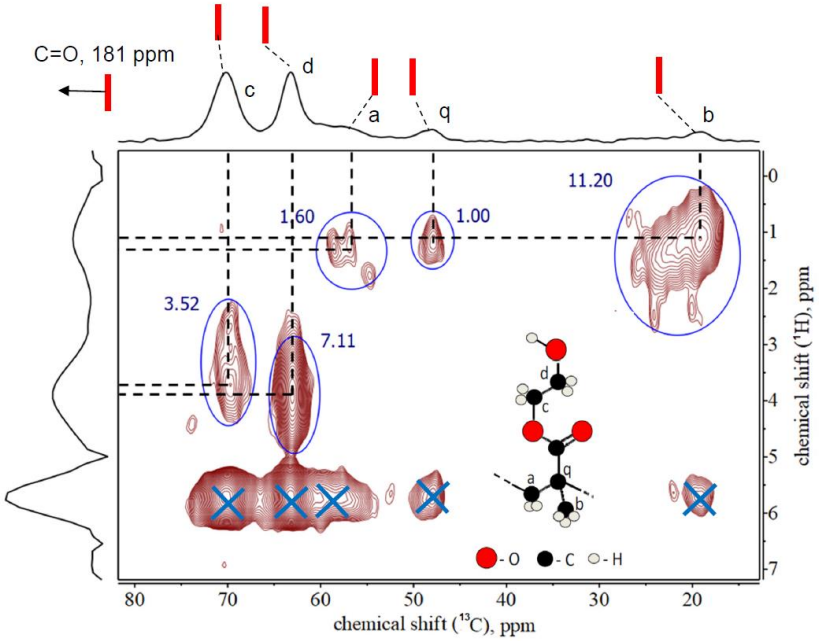

Figure 4.34. ^{1}H–^{13}C CP-MAS FSLG HETCOR spectrum of neat pHEMA at T = 293 K, MAS rate 10 kHz and contact time 70 μs. The relative values of the integral intensities (the numbers on 2D map nearby each peaks) indicate a good connection between methyl (b), quaternary (q) and (a) carbon sites via ^{1}H–^{13}C dipolar coupling, and on contrary – the side chain sites (c and d) correlate strongly only with each other. The DFT calculated ^{13}C chemical shifts are shown by the vertical bars. The experimental and calculated carbonyl signals (179 and 181 ppm, respectively) are out of scale. The lock magnetization artifacts due to Lee-Goldbourg decoupling are marked by crosses. More comments are given in text.

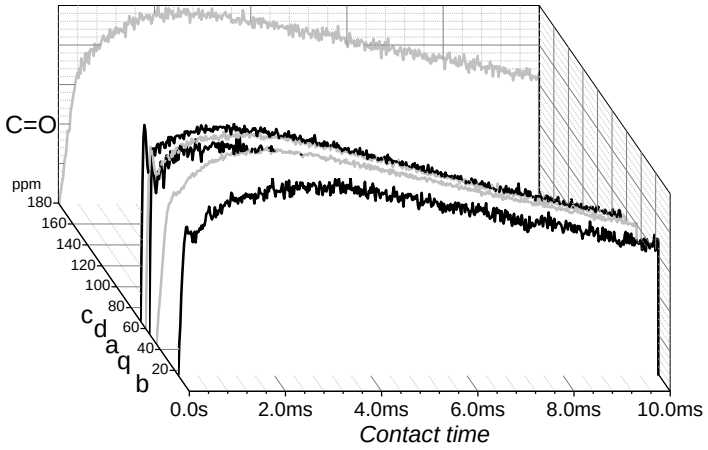

Figure 4.35. $^{1}H \rightarrow ^{13}C$ CP-MAS kinetics in pHEMA. The sample spun at 10 kHz at room temperature. Site notations are taken from Fig. 4.34 and used aside each curve.

Cross-polarization kinetics regarding every peak are depicted in figure above. The initial oscillations were found not to be well defined, therefore, the best processing route with apodization was applied which presumably would lead to the best resolution in the dipolar splitting spectra. The calculated dipolar coupling spectra are shown in figure 4.36. Experimental conditions in this experiment were similar those at figure 4.24 where splitting was measured to me 7200 Hz which was clearly not realistic because the sample was packed in ambient air and was spun at 10 kHz. Thus, this is why an idea of using methyl group (see previous section) might be useful. If the methyl group is allowed to spin around C_3 axis where the dipolar tensor mimics spinning around 70.5° angle, the order parameter $\langle S \rangle$ should be equal to 0.333. Meaning that true dipolar splitting for C-H bond of 23 kHz is multiplied by this factor. Then observed dipolar coupling constant should be around 7.7 kHz and not at 7.5 kHz as it is observed in the case of pHEMA polymer. Thus, instead of using external reference of 23 kHz as a reference, one can use methyl group as an internal reference. Internal standard then corrects the order parameter values.

The corrected order parameter values indicate that CH_2 group on the backbone of the polymer is relatively rigid ($\langle S \rangle$ =0.87) and groups in the sidechain are "soft" – $\langle S \rangle$ is equal to 0.78 and 0.49 for the c and d site, respectively (see inset of Fig. 4.34).

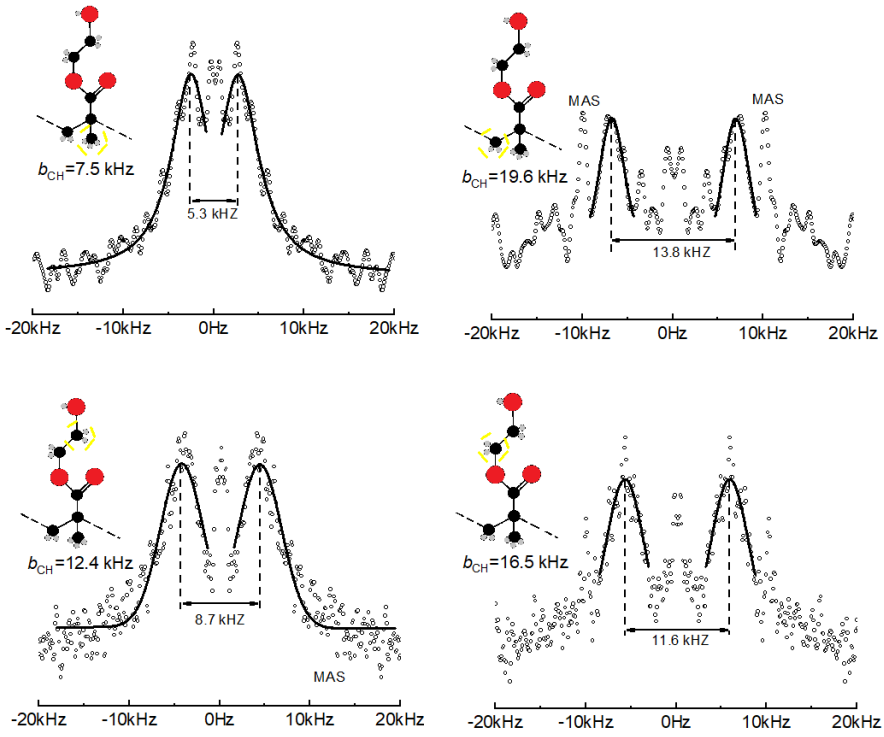

Figure 4.36. Dipolar coupling spectra of pHEMA chemical groups after processing CP kinetics and apodization. Chemical, splitting and dipolar coupling values are written at each spectra.

To visualize how orientational order parameter can be perceived, consider vector r_{CH} connecting two nuclei together. The simplified visualization can be done if the internal motion of this vector is modelled as a restricted diffusion or reorientation in a cone with angle θ (Fig. 4.37). This freedom of motion can originate from large amplitude of vibrations as depicted below or low energetic barrier for reorientations to occur.

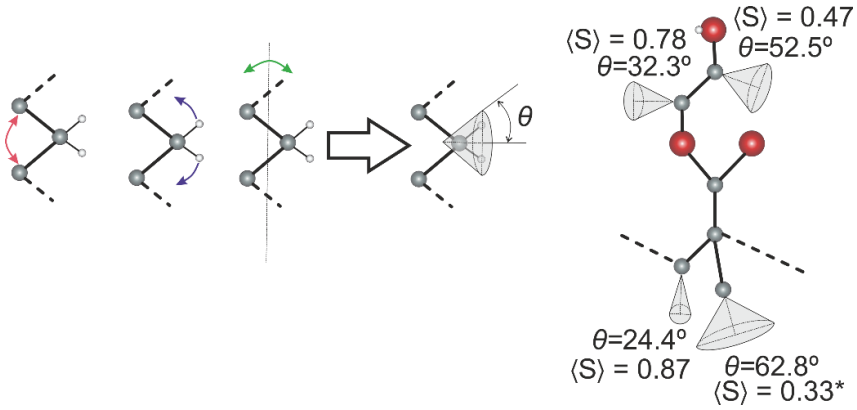

Figure 4.37. On the right – the internal molecular motion modeled as restricted diffusion of the internuclear vector $r_{CH}(t)$ in a cone. On the left – the visualization of the local disorder for a - d sites in pHEMA. *Order parameter for methyl group has been considered invariant and therefore fixed.

Using this visualization order parameter then evaluates to:

$$\langle S \rangle = \cos\theta_0 \, (1 + \cos\theta_0) \, /2 \tag{4.23}$$

where θ_0 is a semi-angle of the cone (see Fig. 4.37). The larger the angle of the diffusion relating cone, the smaller the order parameter. Note again, this visualization is not equivalent to a rotation around the angle, meaning that cone with magic angle (54.7°) will not result in order parameter of zero. Zero, in this case, would correspond the case where diffusion or reorientations happen in all directions (180°).

Thus, if no rotations of the chemical bond are expected one can bear in mind this visualization where order parameter is linked to an amplitude of non-restricted vibration. As pHEMA is one of the hydrogel forming polymers it is expected that monomer side-chains involved into hydrogen bonding network will effectively have more freedom to motion and hence lower order parameter. Therefore, these results are in good agreement with the expectations. By all means, dipolar couplings in comparison to rubber materials are extremely small and thus instead of CP, REDOR technique would provide far more better results. Despite of that, these results only show that CP is a very versatile tool when dipolar coupling are at the orders of kilohertz.

4.4.4 Weakly coupled systems. Probe of fractal dimensionality?

For general understanding of CP in weakly coupled systems it is useful to retract to the simple system of glycine, which has been already analyzed. The processing of experimental data for the next chemical group (COO^-) of glycine was found to be much more complex. It was first noted that the experimental $^1H \rightarrow ^{13}C$ CP-MAS kinetic curves for COO^- carbon (figure 4.38) appeared to be strongly depending on the repetition delay (D1). This effect was negligible in the case of CH_2 carbon. The general tendency was deduced: the higher MAS rate, the longer D1 was necessary in order the ahieve "stationary", i.e. independent on D1, CP kinetics. In the case where MAS rate is 10 kHz it happens at D1 ~ 3.5 - 5 s, whereas for 12 kHz MAS even D1 = 20 s was not enough to reach the stationary regime. It means that a much longer delay is required. This makes the duration of CP experiment infeasibly long.

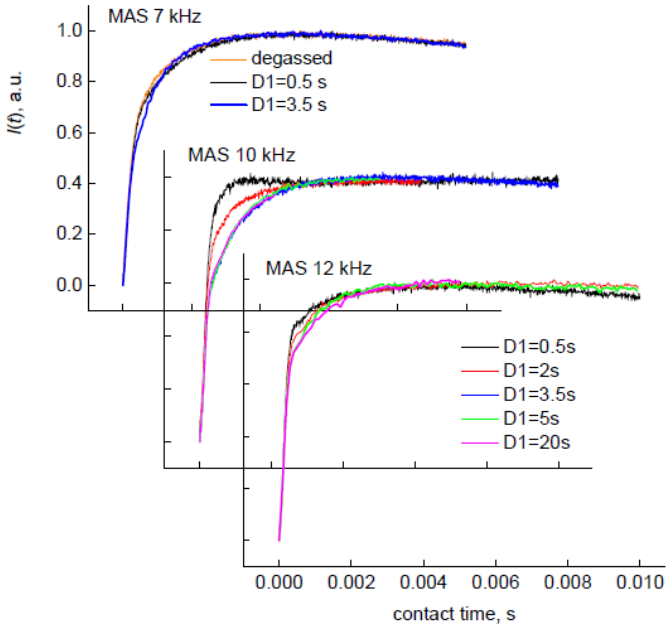

Figure 4.38. The experimental $^1H \rightarrow ^{13}C$ CP-MAS kinetic curves for COO^- carbon measured at different repetition delays (D1).

Therefore the CP kinetics measured at 10 kHz MAS and D1 = 5 s (Figure 4.39) was chosen for the detailed consideration. Moreover, the CP kinetic curve was truncated at a contact time of 5 ms, i.e. just before the CP intensities start to decrease (figures 4.22 and 4.38). This was done because the spin-lattice relaxation constant $T_{1\rho}$ has to be included in the theoretical models in

order to reproduce the decrease of $I(t)$ at longer contact times (5 - 10 ms). The $T_{1\rho}$ values vary in the range of 0.07 - 0.25 s (Table 3). The applied truncation allowed to set $T_{1\rho} \rightarrow \infty$ and thus to reduced the number of variable parameters in the non-linear curve fitting.

Table 5. The fitted parameters of $^{1}H \rightarrow ^{13}C$ CP-MAS kinetics for COO^{-} carbon in glycine obtained for truncated curves (contact times ≤ 5 ms) using different models; $T_{1\rho} \rightarrow \infty$ was set because of kinetics truncation in all cases.

MAS rate	**7 kHz**	**10 kHz**	**12 kHz**
Model 1	1-exp (Eq. (4.24)); $T_{IS} = 1/(2W_{IS})$)		
T_{IS}, μs	540 ± 10	460 ± 10	*
R^2/χ^2	0.984/6.2·10^{-4}	0.965/1·10^{-3}	
Model 2	λ-model (eq (3.24))		
λ	0.712 ± 0.007	0.598 ± 0.006	0.43 ± 0.01
T_{dif}, μs	810 ± 10	860 ± 10	1180 ± 20
T_2, μs	140 ± 30	120 ± 20	130 ± 3
R^2/χ^2	0.999/3·10^{-5}	0.998/4·10^{-5}	0.9997/5·10^{-5}
Model 3	Isotropic spin-diffusion (Eq. (4.12); $k_1/k_2 = 3/2$)		
N	∞	∞	*
k_2, s^{-1}	890 ± 25	950 ± 20	
T_2, μs	220 ± 70	140 ± 30	
R^2/χ^2	0.991/3.3·10^{-4}	0.995/1.5·10^{-4}	
Model 4	Anisotropic spin-diffusion (Eq. (4.12); k_1 and k_2 are independent; $1/T_2 \rightarrow 0$)		
	$k_1 > k_2$		
N	∞	∞	*

k_1, s^{-1}	4200 ± 200	2600 ± 400	
k_2, s^{-1}	980 ± 20	950 ± 20	
R^2/χ^2	0.997/1.1·10^{-4}	0.995/1.4·10^{-4}	
	$k_1 << k_2$		
N	4.0 ± 0.7	15 ± 11	*
k_1, s^{-1}	1130 ± 30	1070 ± 50	
k_2, s^{-1}	5100 ± 300	6200 ± 500	
R^2/χ^2	0.998/7·10^{-5}	0.995/1.6·10^{-4}	
Model 5	Thermal equilibration (Eq. (4.9) + Eq. (4.28), accepting $g(t) \approx 1$, $k_T = k_2$, $\alpha = 1$ (fixed))		
N	1.8 ± 0.1	5.0 ± 0.5	*
k_1, s^{-1}	1360 ± 30	1160 ± 25	
k_2, s^{-1}	27300 ± 1500	16500 ± 500	
R^2/χ^2	0.995/1.9·10^{-4}	0.997/9·10^{-5}	
Model 6	Thermal equilibration (Eq. (4.9) + Eq. (4.28), accepting $g(t) \approx 1$, $k_T = k_2$, α varying))		
N	2.44 ± 0.2	7.3 ± 1.5	*
k_1, s^{-1}	1230 ± 20	1110 ± 30	
k_2, s^{-1}	29800 ± 1300	18000 ± 700	
α	0.7 (fixed)	0.73 ± 0.03	
R^2/χ^2	0.984/6.27·10^{-4}	0.998/6·10^{-5}	

*– as the relaxed (stationary) regime (independent on D1) was not achieved using 12 kHz MAS, the processing of this CP kinetic data using other models was not carried out (see comment in text).

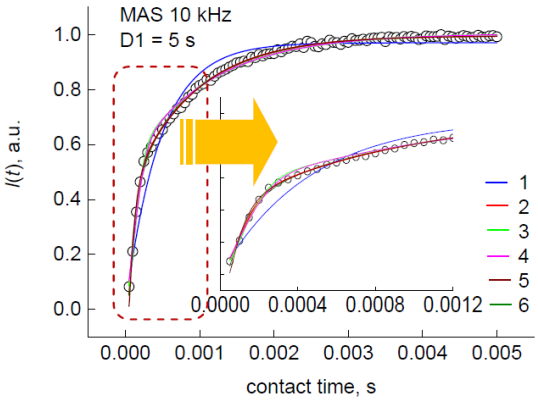

Figure 4.39. The experimental $^{1}H \rightarrow {}^{13}C$ CP-MAS kinetic curves for COO^{-} carbon at 10 kHz MAS (circles) processed applying various CP models (solid lines). The numbering of models (1- 6) and the fit parameter values are given in Table 5.

A quite interesting tendency, viz. $N \rightarrow \infty$, was revealed applying the isotropic spin-diffusion model (Eq. (4.12), with $k_1/k_2 = 3/2$) for the CP kinetics at 7 and 10 kHz MAS rates (Table 5). This would mean that in the case of CP transfer from the remote spins the spin-cluster $S–I_N$ becomes infinite in size. However, the model of isotropic spin-diffusion is inadequate for the present spin-system because it produces some significant non-randomly distributed residuals at the contact time below 1 ms (figures 4.39 and 4.40). This is also reflected by the R^2 and χ^2 values (Table 5). The physical reasons for such failures may lie in the weakness of the coupling between ^{13}C spin and remote protons. According to the structural data of glycine (Fig. 4.21), the largest $^{1}H–{}^{13}C$ coupling constant for COO^{-} carbon should not exceed $b_{CH} = 3000$ Hz. Furthermore, even this spin-coupling can be reduced by H-bonding and internal dynamics of some molecular segments in glycine. It was shown in ref [132] that, if the spin-diffusion rates are of the same order or larger than the I–S couplings, the system is dominated by the homonuclear (I–I) interactions. The transfer of polarization from the I spins to the S spin can be described then by the single exponential increase up to $\langle S \rangle_{qe}$:

$$\langle S_z \rangle(t) = \langle S \rangle_{qe}(1 - e^{-2W_{IS}t}) \qquad (4.24)$$

where W_{IS} is the transfer rate constant that is related to the dominant heteronuclear coupling b_{0eff}, viz. $W_{IS} \sim b_{0eff}^2$. Equation (4.24) was successfully

applied by S. Hediger to describe the CP kinetics in a powder sample of adamantane[132]. The latter system exists at room temperature in the solid phase with orientational disorder (plastic crystal), i.e. the crystalline material with fast 3D-rotational motion of the molecules. Therefore, all intramolecular dipolar couplings are averaged to zero. The CP transfer occurs via intermolecular couplings. This model was also applied for the processing of CP kinetics for COO^- carbon. One could easily note that Eq. (4.20) is equivalent to the classical model (Eq. (3.23)), if $T_{1\rho} \to \infty$ and $T_{IS} = 1/(2W_{IS})$. Thus, further this approach was called as "1-exp" model. Unfortunately, the results of the fitting using Eq. (4.24) were even worse than those obtained in the above cases of isotropic spin-diffusion and λ- models (Table 5). The large non-random residuals (up to 5 - 15 %) are seen at the contact time below 2 ms (figures 4.39 and 4.40). Hence, both models (1-exp and isotropic spin-diffusion) look to be mathematically almost equivalent. The following explanation of such contiguity can be given.

In the case of $k_1 = 3k_2/2 >> 1/T_{1\rho}$ (and this is certainly valid in present context) the thermal equilibrium (Eq. (4.10)) is reached because $N \to \infty$, and thus Eq. (4.12) returns to Eq. (3.22). Furthermore, as the spin-coupling in the present system is weak (say, $b_{CH} \sim 3000$ Hz), the frequencies of the oscillation in equation (3.22) are distributed roughly in the range 0 – 1000 Hz. The dipolar distribution would be rather narrow such that $T_2 \to \infty$. Hence, for the initial stage of CP, i.e. at short contact time, the term $\cos(b \cdot t/2)$ can be roughly set to 1 and then the approximation of $g(t) \to 1$ should be valid. Under these conditions, isolated spin pair CP model (Eq. (4.12)) can be essentially reduced to:

$$I(t) = 2I_0\left\{1 - \frac{1}{2}\left(e^{-k_1 t} + e^{-k_2 t}\right)\right\} \tag{4.25}$$

It is also likely that two exponents in the expression above could merge into one during the non-linear fitting if the spin diffusion rates are similar. This would result in the following result:

$$\frac{1}{2}\left(e^{-k_1 t} + e^{-k_2 t}\right) \to e^{-ak_2 t} \tag{4.26}$$

where a is the factor introduced in the sense of rescaling of the "true" spin diffusion rate $k_2 = 1/T_{dif}$. It depends on the experimental database and the precision, the time scale as well as on the values of k_2 and k_1. In previous sections it was shown that the isotropic constraint $k_1/k_2 = 3/2$ is valid, the two- and single exponential decay functions (Eq. (4.23)) are practically

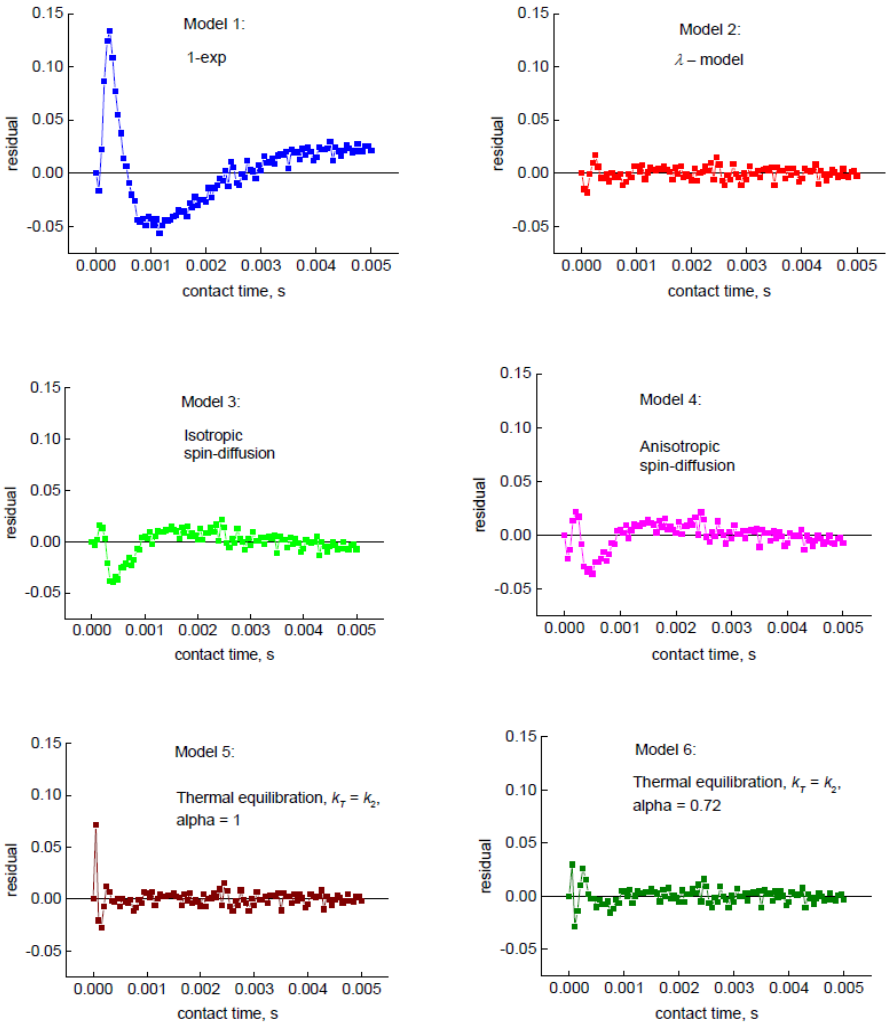

Figure 4.40. The residuals (the differences between experimental and theoretically calculated values of CP intensity using various models (Table 5)) for COO^- spin system at the MAS rate of 10 kHz and the repetition delay of 5s.

undistinguishable for many regimes of CP kinetics, even when relatively huge data set acquired with very high precision are used. The isotropic spin-diffusion and the "1-exp "model become equivalent. As two models converge into each otther, the CP rate constants $1/T_{IS}$ and $1/T_{dif}$ used in those equations are then related by:

$$\frac{1}{T_{\mathrm{IS}}}(=2W_{\mathrm{IS}}) \rightarrow a\,k_2 \;=\; \frac{a}{T_{dif}} \qquad (4.27)$$

However, the results of fitting (figures 4.39 and 4.40) have shown that the single exponential increase was improper to describe the CP kinetics in this spin system. It suggests that ratio of $k_1/k_2 = 3/2$ should not be constrained and allowed to vary freely during the non-linear fitting. This means that anisotropic spin diffusion can be a plausible model. This idea was successful for the CP kinetics over a long contact time in the single crystal ferrocene where $k_1 = 3\,k_2$ ratio deduced. And indeed, the theoretical CP curves calculated using the anisotropic spin-diffusion model (Eq. (4.12), taking $1/T_2 \rightarrow 0$) better fits to the experimental data in comparison with the models of isotropic spin-diffusion or single exponential increase (Table 5 and Fig. 4.40). It is very important to note that the flow $\chi^2 \rightarrow$ *minimum* has converged into two minima in the χ^2 space, depending on the initial (0th order) values of the fitting. The first minimum corresponds to the case when the CP transfer would cover the infinite ^{13}C–^{1}H spin-cluster ($N \rightarrow \infty$), as it was in the case of isotropic diffusion. However, the factor between k_1 and k_2, instead of 3/2, was found to be within 2.7-4.0, depending on the MAS rate (Table 5). Nevertheless, these results look to be rather doubtful because of too high values of k_1 (~2600-4200 s^{-1}) bearing in mind that the coupling between ^{13}C spin and remote protons is very weak. The second minimum on χ^2 surface is more interesting. It corresponds to the ^{13}C–^{1}H spin-clusters of finite size characterized by N from 4 to 15. However, the values $k_1 << k_2$ look very

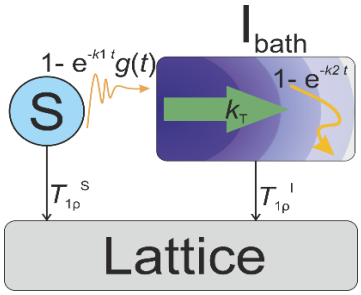

Figure 4.41. Schematic representation of the theoretical model that includes the thermal equilibration in the reservoir of the abundant spins.

surprising and to the best knowledge never met in the literature before. The obtained k_1 values are acceptable for weak coupling whereas k_2 values where surprisingly high and, perhaps, relates to a deep physical meaning. Namely, this indicated that a strong dipolar coupling should be present in the reservoir

of the abundant spins. Thus, this points towards the importance of ^{1}H–^{1}H couplings therein which probably drive polarization equilibration processes.

Following the last thought that two equilibration processes has distinctively different timescales, slightly altered model can be proposed. It can be depicted in block diagram (Fig. 4.41). It is based on some ideas present in the thesis of S. Hediger.

The maximum polarization that the spin S can attain in the quasi-equilibrium state is the thermal equilibrium value given by equation (4.10). For finite *N* values the thermal equilibrium can be reached only in the open spin systems. However, nearly nothing is known about the rate and path of this process. Therefore, to involve the thermal equilibration the equation (4.10) is modified with

$$\langle S\rangle_{qe} = \frac{N}{N+1}\omega_{0I}(1-\exp(-k_T\,t)^{\alpha}) \tag{4.28}$$

Here k_T is the rate constant of thermal equilibration and α is the additional variable parameter introduced to prove the possibility of the non-Debye type process[133].

In order to reduce the number of variable parameters, assumption $k_T \approx k_2$ was made, i.e. the rates of thermal equilibration and spin-diffusion in the I spin bath (Fig. 4.41) are practically the same. Despite it looks rather rough (see Fig. 4.40) , the best fit of experimental data and theory was obtained using this approach (Table 5). Hence, the anisotropic spin-diffusion model coupled with the thermal equilibration in the proton bath was found to be the most proper to describe the CP kinetics in weakly coupled system containing remote spins. Concerning non-Debye response – the interpretation of apparent $\alpha \approx 0.7$ at the MAS rate of 10 kHz (Table 5) raises the following question of whether this parameter has a physical meaning.

In order to address spin diffusion and thermal equilibration in the abundant spin system more carefully, the new advances in quantum mechanical description of cross-polarization may be included. It has been demonstrated that spin-diffusion superoperator can be divided into two terms[134]:

$$\hat{\hat{\Gamma}}(\rho) = R_{dp}\left[\hat{I}_z,\left[\hat{I}_z,\rho\right]\right] + R_{df}\left\{\left[\hat{I}_x,\left[\hat{I}_x,\rho\right]\right] + \left[\hat{I}_y,\left[\hat{I}_y,\rho\right]\right]\right\} \tag{4.29}$$

where R_{dp} and R_{df} are rate constants. This allows to fathom into the physical essence of spin diffusion processes much deeper. The rate constant R_{dp} is associated with the flip-flop term (comonly designated as $\hat{I}^1_-\hat{I}^2_+ + \hat{I}^1_+\hat{I}^2_-$

operator) term of the homonuclear (I–I*) dipolar Hamiltonian whereas R_{df} characterizes the rate of thermal equilibration with the bath. The effect of R_{dp} can be associated with a process, where the environment "observes" the system breaking its coherences driving the system to the internal quasi-equilibrium[134]. It has to be noted that R_{dp} and R_{df} contain the different sources of anisotropy of the I–I* system-environment interaction. Therefore, previously used rate constants k_1 and k_2, these can be related with R_{dp} and R_{df} as $k_1 = R_{df} + R_{dp}/2$ and $k_2 = R_{df}$. The most often used approximation (isotropic spin diffusion) considers $R_{dp} = R_{df}$ and thus $k_1 = 3k_2/2$ can be again proved.

The rate constant k_2 in Eq. (4.28) has then to incorporate the rate of equilibration with the bath R_{df} driven by the spin diffusion due to differences in spin temperatures as well as the rate of thermal motion induced by micro-gradients of the sample temperature set during each experiment. These gradients may certainly appear in a high-power pulsing CP experiments. The effect observed on the CP kinetic curves in glycine can be noted here as indicative, namely, where the experimental $^{1}H \rightarrow {}^{13}C$ CP-MAS kinetic curves for the remote spin system (COO^{-} carbon) appeared to be strongly depending on the repetition delay (D1). Furthermore, it can be supposed that for weakly coupled systems of remote spins $k_T >> R_{df}$, thus the rate constant k_2 in Eq. (4.28) can be replaced by k_T as it was done following phenomenological assumptions.

Now, the parameter α is related to parameter $D_p = 3\alpha$ called fractal dimension[133]. Thus, it would follow that stretched exponent approach provides with the additional parameter. Obviously, making such a strong statement requires more experiment support. The correct approach is to test system with known fractal dimension. One of the possible candidates is calcium hydroxyapatite which has been already analysed. It was shown by M. Yashima that protons in CaHA diffuse in almost linear fashion (see figure in ref 135). This would mean that spin diffusion of *I* spins or thermal equilibration of protons should sense lower dimensionality. In addition to that, similar system of poly-(vinyl phosphonic acid) (pVPA) was used as well as hydrogen atoms in this polymer are arranged in single line. The combined equation of the model which was already used in Table 5 is the following:

$$I(t) = \mathrm{e}^{\frac{-t}{T_{1\rho}}} - \mathrm{e}^{-k_1 t} + \left(\frac{N-1}{N+1}\right)(1 - \exp(-k_2\, t)^{\alpha})\left[\mathrm{e}^{\frac{-t}{T_{1\rho}}} - \mathrm{e}^{-k_2 t}\right] \quad (4.30)$$

The fitting results for all investigated weakly coupled systems are presented in the Table 6 where comparison between models is made. Note that $^{1}H \rightarrow {}^{31}P$

CP kinetics in cases of CaHA and pVPA were analysed instead of $^{1}H \rightarrow ^{13}C$ CP like in the most of the results.

Table 6. The fit parameters of CP-MAS kinetics for the studied materials obtained using the models of isotropic spin diffusion and anisotropic spin diffusion with thermal equilibration. Fractal dimensionality is marked green.

Part 1

	CaHA (static)	CaHA (MAS)	pVPA	pHEMA
Isotropic spin diffusion (Eq. (4.12))				
N	∞	∞	∞	∞
k_2, s^{-1}	1380 ±30	1370 ±10	4320 ±30	1010 ±20 (q) 90 ±40 (C=O)
T_2, μs	∞	∞	∞	79 ±1 210 ±5
$T_{1\rho}$, s	0.020 ±0.001	0.012 ±0.001	0.0027 ±0.0001	0.014 ±0.001
R^2/χ^2	0.938/$1.2\cdot10^{-3}$	0.994/$1.9\cdot10^{-4}$	0.997/$2.4\cdot10^{-4}$	0.991–0.968 $(2\text{-}8)\cdot10^{-4}$
Anisotropic spin diffusion with thermal equilibration (Eq. (4.29)), α = 1				
N	∞	∞	∞	
k_1, s^{-1}	680 ± 50	810 ±40	2440 ±30	
k_2, s^{-1}	10900 ±300	6450 ±110	18720 ±120	
$T_{1\rho}$, s	0.017 ±0.001	0.011 ±0.001	0.0026 ±0.0001	
R^2/χ^2	0.954/$9.1\cdot10^{-4}$	0.983/$5.0\cdot10^{-4}$	0.999/$9.0\cdot10^{-5}$	
Anisotropic spin diffusion with thermal equilibration , α is variable				
α	0.32 ±0.01	0.28 ±0.01	0.33 ±0.01	0.57 ±0.02 0.52 ±0.02
D_p	0.96 ±0.03	0.84 ±0.03	1.00 ±0.03	1.71 ±0.06 1.56 ±0.06
N	∞	∞	∞	∞
k_1, s^{-1}	617 ±6	1280 ±20	410 ±160	1010 ±20 840 ±40
k_2, s^{-1}	20800 ±200	9100 ±160	18650 ±250	33700 ±1300 12900 ±500
$T_{1\rho}$, s	0.013 ±0.001	0.010 ±0.001	0.0025 ±0.0005	0.013 ±0.003
R^2/χ^2	0.999/$1.4\cdot10^{-5}$	0.999/$2.5\cdot10^{-5}$	0.999/$4.8\cdot10^{-5}$	0.992–0.971 $(2\text{-}7)\cdot10^{-4}$

Part 2

	Glycine	Other amino acids	Gly-Pro-Gly Gly-Gly-Gly
Isotropic spin diffusion (Eq. (4.12))			
N	∞	~ 1.5–∞	∞
k_2, s^{-1}	950 ± 20	~ 650–3000	4100 ±200 2390 ±90
T_2, μs	140 ± 30	~ 140–300	130 ±20 214 ± 15
$T_{1\rho}$, s	∞	~ 0.004–∞	∞ 0.025 ±0.001
R^2/χ^2	0.995/1.5·10^{-4}		0.971/6.5·10^{-4}
Anisotropic spin diffusion with thermal equilibration (Eq. (4.29)), α = 1			
N	15 ± 11		
k_1, s^{-1}	1070 ± 50		
k_2, s^{-1}	6200 ± 500		
$T_{1\rho}$, s	∞		
R^2/χ^2	0.995/1.6·10^{-4}		
Anisotropic spin diffusion with thermal equilibration, α is variable			
α	0.73 ±0.03	~ 0.66–1	0.89 ±0.07
D_p	2.19 ±0.09	~ 2–3	2.67 ±0.21
N	7.3 ±1.5	~ 1–4	∞
k_1, s^{-1}	1110 ± 30	~ 400–1500	4900 ±300 3320 ±160
k_2, s^{-1}	18000 ±700	~ 6500–11000	16700 ±700 10000 ±300
$T_{1\rho}$, s	∞	~ 0.004–∞	∞ 0.032 ±0.001
R^2/χ^2	0.998/6.0·10^{-5}		0.976/5.4·10^{-4}

Firstly, it is important to note that spin diffusion rate is $k_1 << k_2$ when thermal equilibration is assumed. It suggests that this process is indeed much faster than initial CP build-up. Magic angle spinning, however, slightly reduces this discrepancy since some remote spin-pairs are then "disconnected" from the overall CP process by rapid sample spinning.

Another notable difference going towards the last model is goodness of fit. This suggest that isotropic spin diffusion indeed does not fully explain the cross-polarization behavior. Furthermore, parameter R^2 reaches maximum in all cases of weakly coupled spins when stretched exponent is incorporated. Unfortunately, this could signify overparameterization since number of

variables is increased. This is why using additional model system of pVPA where low dimensions for proton transfer is known, is especially useful.

Rather welcome result was achieved in the latter material. Non-linear fit indicates that thermal equilibration in sub-system of protons is driven in single dimension. This is reinforced by calculated fractal dimension of CaHA, where it was shown that proton diffusion also flows in one channel. All results regarding fractal dimensionality can be summarized in the picture below.

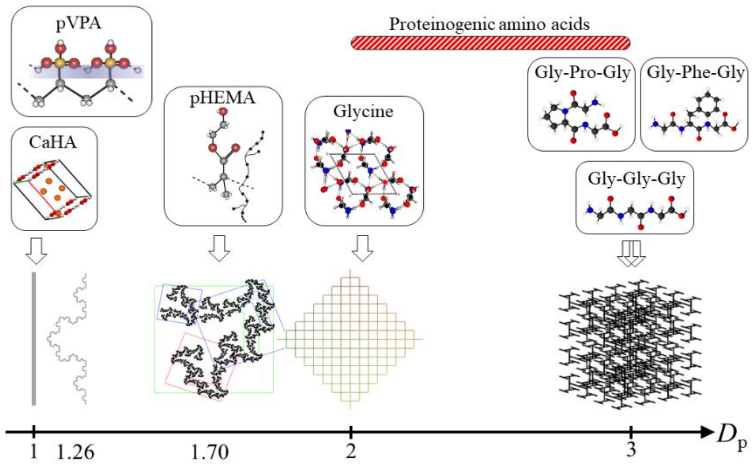

Figure 4.42. Fractal dimension of analysed materials obtained through processing of CP kinetics of weakly coupled spin pairs. Pictures of known fractals shown below for a comparison. More comments in the text.

Other materials seem to yield higher dimensionality. Firstly, fractal dimensions of iterated function systems are typically low (see figure above), usually below 2. This is within a good agreement with the results obtained for pHEMA since polymer side-chain can link to the back-bone chain repeating the same pattern due to strong hydrogen bonding at the end of the side-chian. Thus, the result can be considered as the evidence of structure obtained. Secondly, going further to proteinogenic amino acids and peptides, D_p increases. As glycine is a small molecule it can form a robust structure with intrinsic fractal behavior. In contrast to that, self-aggregating molecules like tripeptides can form bulky structure where thermal equilibration is not restricted to any directions. Also results regarding the second part of Table 6 indeed indicate that isotropic spin diffusion model fit the data with high values of $R^2 = 0.971$. The increase of this parameter is best observed in the cases where fractal dimension is low. Lastly, processing results of other

proteinogenic amino acids covers the large range of fractal dimensions from 2 to 3 which implies that this parameter could be very specific property of the intrinsic structure.

Conclusions of section 4.4

- The resolution and quality of dipolar coupling spectra was enhanced when additional interactive apodization in the processing route was introduced.

- Rapidly rotating methyl groups were used as internal molecular standard as criterion for completeness of apodization.

- High resolution in dipolar coupling spectra allowed to monitor local order parameters in chemical groups going from rigid amino acids towards soft peptides and polymer. This allows to compete with the most common techniques where information is only one-dimensional.

- For the first time it was demonstrated that spin diffusion rate in amino acids increases with the density of interacting nuclei.

- The S-I*-I model with isotropic spin-diffusion is appropriate to describe the $^{1}H \rightarrow ^{13}C$ cross-polarization kinetics in typical strongly coupled chemical groups in organics where dipolar coupling is large.

- The anisotropic spin-diffusion found to be convenient approximation regarding $^{1}H \rightarrow ^{13}C$ cross-polarization in the glycine COO^{-} groups where interacting spins are remote.

- The data for remote spins was best fitted including thermal equilibration in I spin reservoir since I-I couplings are significantly stronger then I-S. This opens a possibility to probe thermal equilibration. The use of stretched exponent approach implies a possibility of non-Debye process during thermal equilibration.

- Assuming non-Debye process in thermal equilibration of I spins fractal dimension was deduced for a series of compounds. The observed line-up corresponds well with fractal images of analysed structures, thus it opens a new possibility to use cross-polarization as a tool to probe structures with fractal dimensions.

4.5 Additional topics

The objective of this section is to slightly emphasize on few issues or thoughts that may have occurred reading this work. Since these topics are not at the main focus of this dissertation or also have been explicitly discussed in the dissertation of dr. V. Klimavičius, they are separated from the rest of the work. The first topic underlines the flow of non-linear fitting using many variables. It has come to the attention many times that it is typically hard to trust non-linear fitting with many free variables. Hence the part of this section will discuss this problem on the basis of the dissertation. The second topic demonstrates the missing link of I-I*-S and I-S models. These models originate from very different approaches: one is come from pure quantum mechanics and the other from thermodynamics. The question is whether there is a transition point from one to the other.

4.5.1 The convergence multi-parameter fitting to global minumum

There is a main obstacle working with non-linear fitting procedures that require large set of parameters is trying to find the "true" (global) minimum in multi-parameter space of χ^2, i.e. the sum of weighted squares of deviations of the chosen theoretical model curve from the experimental points. However, during the fitting several or even many local minima can be found on χ^2 surface depending on complexity of the model, precision and completeness of the experimental data set. These local minima would misrepresent non-linear fit. In the present work the Levenberg - Marquardt method of minimization was applied. It is implemented in many widely used computing packages, e.g. Microcal Origin, Mathcad, etc. The following example is an example of data fitting in the ammonium dihydrogen phosphate case (see section 4.3).

The acquired experience in the fitting of CP kinetic curves allows to give some criterions and recommendations to recognize the false minima and to search for the proper initial values set. The false minimum can be easily recognized by following: i) apparent systematic (non-random) deviations (see red curve in Fig. 4.42); ii) relative values of R^2; iii) the physical sense of obtained values (*e.g.* $T_2 < 0$). In order to find the right path toward the global minimum it is recommended for the first iteration to keep fixed the values of some parameters that can be *a priori* approximately determined from other experimental data. For instance, the spin-spin relaxation time T_2 can be evaluated from the full width at half maximum (FWHM) of ^{31}P signal for the static sample using the "uncertainty" relation FWHM$\times T_2$= 0.375 that is valid for the Gauss functions. Moreover, Eq. (4.20) parameters I_0 can be roughly set

as 0.7 - 0.9 of maximal intensity value and exp(–$t/T_{1\rho}$) can be found with logarithm of the end in CP kinetics. Keeping these values fixed the remaining parameters are refined during the first iteration and then taken as zero-order set in the next run. If the correct minimization path is found, then all parameters can be varied getting the stable flow to the same minimum without restrictions.

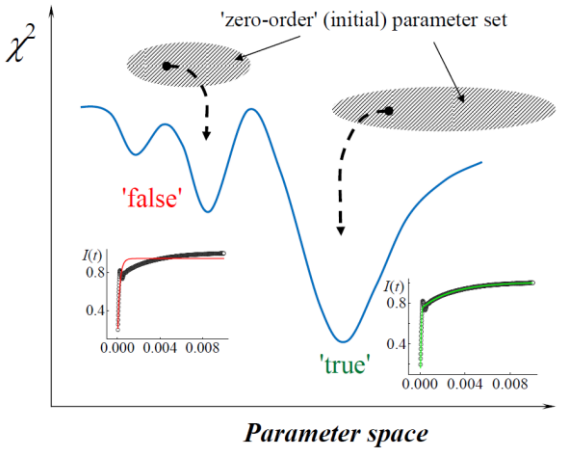

Figure 4.43. Non-linear multi-parameter fitting: the problem of flow towards the 'true' (global) minimum. More comments in text.

In order to study the effect of random errors on the stability of flow and on the values of adjusted parameters the CP kinetic curve (Fig. 4.14) was artificially disturbed adding the noise of various levels (2 -10 %, see Fig. 4.44 a - c) and the sequent repeat of all steps of processing. The results are shown in figures 4.44d and 4.45.

It is clearly seen that the most sensitive parameters to the noise level are k_1, and $p_1 = (N–1)/(N+1)$. This could be the major source of error of non-linear fit. The effect of noise on the spatial distribution of protons surround ^{31}P nuclei $P(r)$ is of particular interest. These results are shown in Fig. 4.45. It can be concluded that the random errors can affect $P(r)$ at longer distances (r > 0.3 nm) significantly if the nose level exceeds 5 % whereas the position of the first peak remains to be quite stable.

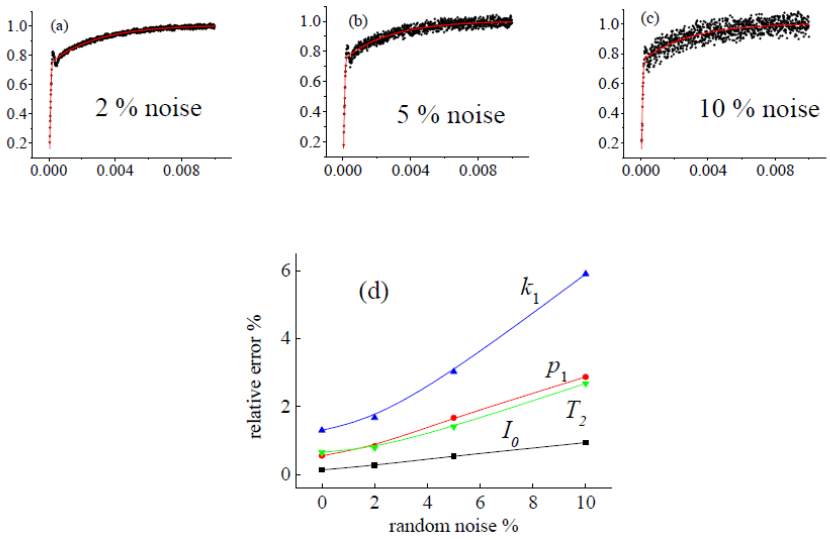

Figure 4.44. Effect of random noise on the CP kinetics (a-c) and on the precision of adjusted parameters (d): I_0, k_1, $p_1 = (N - 1)/(N + 1)$ and T_2 (Eq. (4.12)). The relative error (%) means the standard error put out by the computing routine divided by the value of corresponding parameter.

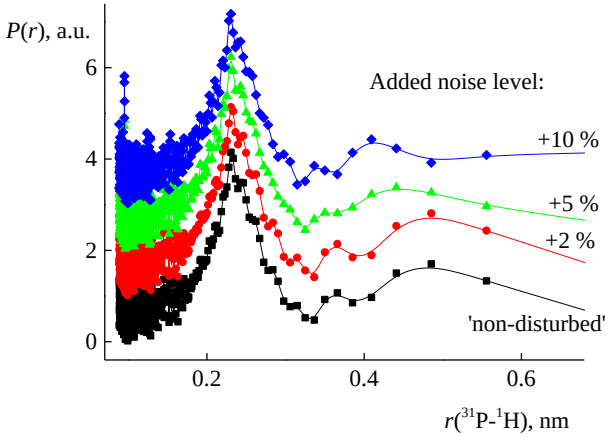

Figure 4.45. Effect of random noise on the spatial distribution of protons surround ^{31}P nuclei.

In conclusion, the high experimental data point density on CP kinetic curves used in the present work makes the minimization procedure quite stable

with respect to the random errors. This big data set reduces the excess degrees of freedom in the non-linear fitting procedure targeting its flow towards the global minimum on the multi-parameter surface. It makes possible more rigorous decision concerning the validity of the hypothetic models and more fitting parameters can be used and determined unambiguously.

4.5.2 Convergence of I-I*-S and I-S models

As two cross-polarization models are originating from different perspectives, it is not surprising that the general outcome is a large discrepancy between them. However, it was demonstrated in section 4.4.1 that under correct assumptions equations describing one model can converge into another. The demonstration was done in remotely interacting spin pairs in glycine. Unfortunately, this have not resulted in improvement of fit meaning that I-S model is not valid for that spin pair. As mathematically these models can be connected, perhaps, nano-structured or crystalline material is not the typically environment where this convergence would be seen. Thus, completely different system of room temperature ionic liquid (RTIL) [bmim][BF_4] has been investigated. The compound was impregnated in meso-porous silica commonly known as MCM-41 and SBA-15 as to work in solid-state environment and to dilute the abundant spin numbers. The latter will be explained later.

The complex shaped ^{11}B CP-MAS signals were observed in MCM-41 and SBA-15 (Fig. 4.46). They were decomposed into two Lorentz components denoted as “narrow” and “broad”. This points to the possibility of bimodal distribution of [bmim][BF_4] in mesostructured silica, similarly, as it was observed in the case of water as a guest molecule[136]. The CP kinetics data were processed using two spin coupling models for each kinetic curve separately.

Now, recall how equation (4.12) was rewritten into (4.20) which converts to Eq. (3.24) if diffusion rates are much faster than relaxation, then parameter λ is rewritten into (4.21). The relation (4.12) has the advantage not only because it elucidates the physical sense of the parameter λ, but also because it provides the way to follow the convergence between isolated spin pair and thermodynamical spin coupling regimes without any *a priori* discrimination, which of those should be valid for the system in this study. It is quite logical to suppose that at the infinite enlargement of the spin cluster size the non-classical I–I*–S model has to convert to the classical I–S one. And indeed, the

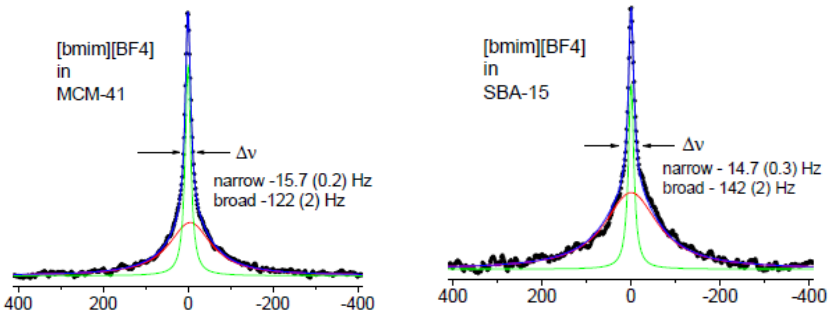

Figure 4.46. ^{11}B CP-MAS line shapes of [bmim][BF_4] as a guest compound in MCM-41 and SBA-15. The errors determining the line widths are given in the brackets.

requirement for high dilution of spin *S* among spins *I* is certainly fulfilled, i.e. $N_S/N_I \rightarrow 0$. Furthermore, if the I–S heteronuclear coupling is sufficiently reduced by high spin mobility, the CP kinetics should obey the thermodynamical I–S model.

Let us assume infinite cluster size *N*, then (4.20) turns into:

$$I(t) = 2I_0\left\{e^{-\frac{t}{T_{1\rho}}} - \frac{1}{2}\left(e^{-\left(k_1 t + \frac{t^2}{2T_2^2}\right)} + e^{-k_2 t}\right)\right\} \qquad (4.30)$$

Then the principal question that arises carrying out the non-linear curve fitting is – can the expression in the internal brackets (...) be recognized by the computing as the sum of two exponents, or such behaviour is merged to a single exponential decay as shown in expression (4.26). The answer certainly depends on the experimental precision as well as on the parameters k_2, $k_1 = 3k_2/2$ and T_2. This was checked taking the set of some "realistic" k_2 and T_2, *i.e.* those often met in the CP kinetics experiments. The results are depicted in figure 4.46. The perfect fit the was obtained in the case of "narrow" as well as "broad" *b*-spectrum, (short- and long T_2, respectively), varying only one parameter – the rescaling factor *a*. This means that at the present regime of CP transfer, which is determined by k_2 and T_2 values, the two- and single exponential decay functions are undistinguishable. Thus, it can be stated that for the large spin clusters at present conditions the two models are practically undistinguishable.

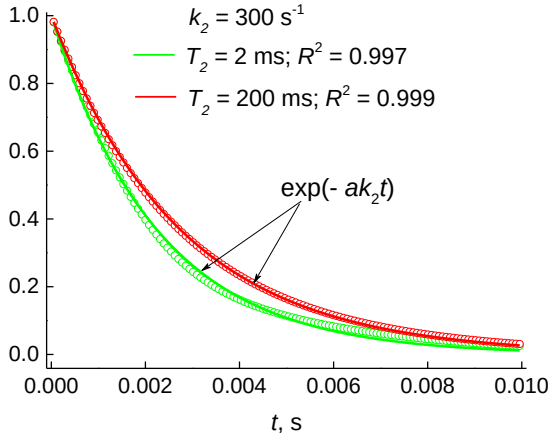

Figure 4.47. The imitation of two exponential term (brackets (…) in Eq. (4.30)) by the single exponent with the rescaled spin diffusion rate $a \cdot k_2$ (solid lines). The different T_2 values correspond to "broad" and "narrow" distributions of the dipolar splitting. The adjusted a values are within 1.2 - 1.5. Computer generated points shown by open circles.

As measured CP-MAS signals of ^{11}B were decomposed into two Lorentz-shaped "narrow" and "broad" components, the CP kinetics were studied for each signal separately. The results are presented in Fig. 4.48. Indeed, both spin coupling models, discussed above, can be identically good fitted (getting almost the same R^2 values) to the experimental curves and thus classical (thermodynamical) and non-classical CP (isolated spin pair) transfer regimes are for the studied systems practically undistinguishable. However, the non-classical model seems to be preferable because it directly provides spin diffusion rates which originates from the exact microscopic quantum mechanical model whereas T_{IS} was firstly introduced in more phenomenological way. Despite the adjusted rescaling factor values a were found to be close to 1, hence $T_{IS} \approx T_{dif}$. The non-classical treatment allows to avoid the need to elucidate the physical sense of such rescaling. The fit parameters of CP kinetic curves obtained using Eq. (4.12) are presented in Table 7.

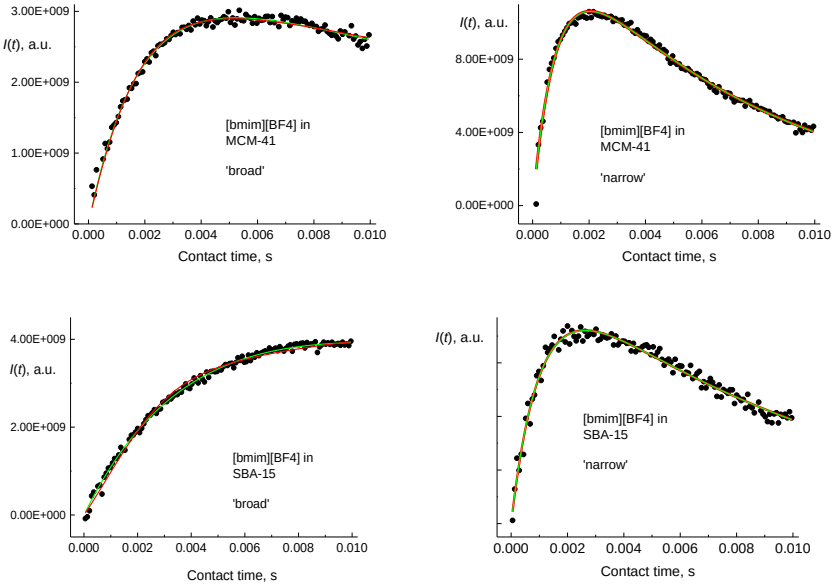

Figure 4.47. $^{1}H \rightarrow {}^{11}B$ CP kinetics upon 5 kHz MAS of [bmim][BF_4] confined in MCM-41 and SBA-15 pores. For both samples the I-S (red line) and I-I*-S (green line) CP transfer models are practically undistinguishable. The fit parameters are given in Table 7.

Table 7. The fit parameters of Eq. (4.12) for CP kinetic curves presented in figure 4.47.

	[bmim][BF_4] in MCM-41		**[bmim][BF_4] in SBA-15**	
	broad	narrow	broad	narrow
I_0, **a. u.**	$3.66 \cdot 10^9$ $\pm 0.07 \cdot 10^9$	$1.6 \cdot 10^{10}$ $\pm 0.2 \cdot 10^{10}$	$4.37 \cdot 10^9$ $\pm 0.04 \cdot 10^9$	$1.05 \cdot 10^{10}$ $\pm 0.02 \cdot 10^{10}$
N	∞	∞	∞	∞
k_2, s^{-1}	374±15	745±24	164±5	617±27
T_2, s	0.0026	0.02	0.0022	0.022
$T_{1\rho}$, s	0.03 ±0.002	0.0072±0.0001		0.01±0.003
R^2	0.984	0.988	0.992	0.971

Without going into details, two signal components were deduced to be originating from [bmim][BF_4] placed in the layers on the pore surfaces ("broad" component) and in the inner layers ("narrow" component), respectively[58]. This means that RTIL behaves quite differently from nano-

structured systems, where the spin systems exhibit definitely isolated spin pair behaviour. Such difference can be caused by several factors: i) the requirement for high dilution of spin *S* among spins *I* is certainly fulfilled (^{11}B is "diluted" among 15 protons in each $[bmim]^+$ cation and those tentatively supposed to be on the pore surfaces); ii) high mobility, i.e. relatively weakly hindered displacement of BF_4^- anion respect to the cation and dynamics of anion along the pore surfaces deletes the borders between spin clusters, thus the spin cluster size $N \rightarrow \infty$. Under these conditions, a tight convergence between two CP models can be observed, however the I-I*-S model seems to more preferable because it directly provides the information on the spin diffusion rate that is originated from the exact microscopic quantum mechanical model.

Conclusions of section 4.5

- Recommendation for processing cross-polarization kinetics using multi-variate non-linear fitting were introduced to guarantee the convergence to the global minimum in parameter space. Results indicate that convergence is stable under effect of random noise with minimal loss of information regarding dipolar coupling.

- A tight convergence between isolated spin pair and thermodynamical cross-polarization regime was demonstrated with ionic liquid confined in mesoporous silica. The use of I-I*-S model instead of I-S one is more preferable since the information on the spin diffusion rate that is originated from the exact microscopic quantum mechanical model is not lost.

RESUMÉ

In the present work cross-polarization – a tool for material research was employed in the large structural manifold of functional materials. Many obstacles in material research can be met when spatial distribution of light elements is masked by complex nature of functional materials or lack of long-range order. Thus, CP could be highly favourable, as it allows to probe dipolar interaction between hydrogen nucleus and other spin species revealing structural complexity in solid matter.

Firstly, the goal of the first part was to demonstrate that important details like chemical composition, time-scale of ongoing processes that can be acquired using 1D NMR techniques. Namely, it was shown how morphology of complex structure of calcium hydroxyapatite affects the spectra, hydrogen content and dynamical features. Then a transition to cross-polarization method was made to reveal structural features with respect to different morphologies. The conclusion has been made that advanced processing of CP kinetics can provide with multiple structural parameters. Therefore, deeper investigation of used CP models was carried out.

With the use of ammonium dihydrogen phosphate, the precision of the spatial distribution of interacting spins was improved and tested. Results have shown that it can be done when model where angular averaging of dipolar coupling in rotating solid is taken into account, is used. The routine to obtain internuclear distances distribution was significantly simplified by including few assumptions. Comparison with the data gathered with XRD and ND indicates very welcoming precision of the developed method, which implies that it can be a tool to measure spatial distribution of light atoms.

Regarding to the most of results, CP investigations then were carried out in organics for their diversity and functionality. Investigation in a large samle of chemical groups revealed significant differences of cross-polarization dynamics going from strongly to weakly coupled systems. The dipolar coupling in weakly coupled systems was enhanced by using apodization method during advanced processing of CP kinetics. Finally, additional equilibration process in abundant spin system was incorporated in CP models which uncovered the possibility to sense fractal dimension in the lattice.

The results of the whole dissertation show that although CP may not seem as trivial method for structural analysis since spin dynamics driving cross-polarization is a complex mechanism, the developed method provides with insightful and accurate results. Moreover, the present work overviews possibilities of using this tool in large variety of structures and thus refined routine can be practically implemented. The advanced processing of CP

kinetics can give direct and precise structural information like spatial distribution of light elements which is at great importance with respect to methods like XRD and ND. Furthermore, CP can be also used to probe local-order, spin-diffusion and even fractal dimension of the abundant spin system. These findings prove that CP is a powerful and perspective tool for material research.

CONCLUSIONS OF THE DISSERTATION

1. Fine details regarding composition, organisation as well as time-scale of dynamical processes in amorphous and nano-structured solids such as calcium hydroxyapatite can be obtained employing ^{1}H and ^{31}P NMR coupled with magic angle spinning.

2. Structural features can be obtained processing initial coherent part of cross-polarization by reverse-calculation as the macroscopic parameters of cross-polarization such as relaxation and spin diffusion times are invariant to spatial distribution function chosen during non-linear fitting

3. The proper mathematical treatment for initial coherent part of cross-polarization has been refined which allows to reduce the Fourier- Bessel (Hankel) transform to the routine Fourier transform calculating the angularly averaged and purely distance-depending interacting spin distribution. This led to consistent and accurate results with respect to those obtained with ND and XRD techniques.

4. Resolution of dipolar coupling spectra, especially for weakly coupled system, can be significantly enhanced using interactive apodization method applied during processing routine. This enables cross-polarization to distinctly probe local order within a molecule.

5. Significant differences between weakly to strongly coupled system were observed. I-I*-S model was found to be valid approximation for strongly coupled spin systems, in contrast to weakly coupled spins where perfect fit has been obtained by introducing the possibility of anisotropic spin diffusion and thermal equilibration in the bath of abundant spins. Very reasonable sequence of the compounds have been lined-up according their fractal dimensions, which followed from thermal equilibration analysis. It allows to state that the treatment of CP transfer between remote spins and equilibration therein can indeed reproduce the fractal images of the studied compounds.

REFERENCES

1. Goesmann, H. & Feldmann, C. Nanoparticulate Functional Materials. *Angew. Chemie* **49,** 1362–1395 (2010).
2. Neel, E. A. A., Pickup, D. M., Valappil, S. P., Newport, J. & Knowles, J. C. Bioactive functional materials: a perspective on phosphate-based glasses. *J. Mater. Chem.* **19,** 690–701 (2009).
3. Chowdhury, E. H. & Akaike, T. Bio-Functional Inorganic Materials: An Attractive Branch of Gene-Based Nano-Medicine Delivery for 21st Century. *Curr. Gene Ther.* **5,** 669–676 (2005).
4. Knowles, T. P. J. & Buehler, M. J. Nanomechanics of functional and pathological amyloid materials. *Nat. Nanotechnol.* **6,** 469–479 (2011).
5. Putnam, C. D., Hammel, M., Hura, G. L. & Tainer, J. A. X-ray solution scattering (SAXS) combined with crystallography and computation: defining accurate macromolecular structures, conformations and assemblies in solution. *Q. Rev. Biophys.* **40,** 191–285 (2007).
6. Flack, H. D. & Bernardinelli, G. The Use of X-ray Crystallography to Determine Absolute Configuration. *Chirality* **20,** 681–690 (2008).
7. Brunger, A. T. *et al.* Crystallography & NMR System: A New Software Suite for Macromolecular Structure Dermination. *Acta Crystallogr. Sect. D* **54,** 905–921 (1998).
8. Harris, R. K., Wasylishen, R. E. & Duer, M. J. *NMR crystallography*. (Wiey, 2009).
9. Martineau, C., Senker, J. & Taulelle, F. NMR Crystallography. *Annu. Reports NMR Spectrosc.* **82,** 1–57 (2014).
10. Zhao, X. S., Lu, G. Q., Whittaker, A. K., Millar, G. J. & Zhu, H. Y. Comprehensive Study of Surface Chemistry of MCM-41 Using CP/MAS NMR , FTIR , Pyridine-TPD, and TGA. *J. Phys. Chem. B* **101,** 6525–6531 (1997).
11. Dagys, L. *et al.* Solid-State 1H and 31P Nmr and FTIR Spectroscopy Study of Static and Dynamic Structures in Sol-Gel Derived Calcium Hydroxyapatites. *Lith. J. Phys.* **55,** 1–9 (2015).
12. Kareiva, S. *et al.* Sol-gel synthesis, phase composition, morphological and structural characterization of Ca10(PO4)6(OH)2: XRD, FTIR, SEM, 3D SEM and solid-state NMR studies. *J. Mol. Struct.* **1119,** 1–11 (2016).
13. Katona, G. *et al.* Raman-Assisted Crystallography Reveals End-on Peroxide Intermediates in a Nonheme Iron Enzyme. *Science.* **316,** 449–454 (2007).
14. Rehman, I. & Bonfield, W. Characterization of hydroxyapatite and

carbonated apatite by photo acoustic FTIR spectroscopy. *J. Mater. Sci. Mater. Med.* **8,** 1–4 (1997).

15. Bryce, D. L. NMR crystallography: Structure and properties of materials from solid-state nuclear magnetic resonance observables. *IUCrJ* **4,** 350–359 (2017).
16. Asakura, T., Kuzuhara, A., Tabeta, R. & Saito, H. Conformation Characterization of Bombyx mori Silk Fibroin in the Solid State by High-Frequency 13C Cross Polarization-Magic Angle Spinning NMR , X-ray Diffraction , and Infrared Spectroscopy. *Macromolecules* **18,** 1841–1845 (1985).
17. Brouwer, D. H. A structure refinement strategy for NMR crystallography : An improved crystal structure of silica-ZSM-12 zeolite from 29Si chemical shift tensors. *J. Magn. Reson.* **194,** 136–146 (2008).
18. Kolodziejski, W. & Klinowski, J. Kinetics of cross-polarization in solid-state NMR: A guide for chemists. *Chem. Rev.* **102,** 613–628 (2002).
19. Müller, L., Kumar, A., Baumann, T. & Ernst, R. R. Transient oscillations in NMR cross-polarization experiments in solids. *Phys. Rev. Lett.* **32,** 1402–1406 (1974).
20. Dagys, L., Klimavicius, V., Gutmann, T., Buntkowsky, G. & Balevicius, V. Quasi-Equilibria and Polarization Transfer Between Adjacent and Remote Spins : 1H -13C CP MAS Kinetics in Glycine. *J. Phys. Chem. A* **122,** 8938–8947 (2018).
21. Klimavicius, V., Dagys, L. & Balevicius, V. Subnanoscale Order and Spin Diffusion in Complex Solids through the Processing of Cross-Polarization Kinetics. *J. Phys. Chem. C* **120,** 3542–3549 (2016).
22. Eliaz, N. & Metoki, N. Calcium phosphate bioceramics: A review of their history, structure, properties, coating technologies and biomedical applications. *Materials (Basel).* **10,** (2017).
23. Suchanek, W. & Yoshimura, M. Processing and properties of hydroxyapatite-based biomaterials for use as hard tissue replacement implants. *J. Mater. Res.* **13,** 94–117 (1998).
24. Duer, M. J. The contribution of solid-state NMR spectroscopy to understanding biomineralization: Atomic and molecular structure of bone. *J. Magn. Reson.* **253,** 98–110 (2015).
25. Gentile, P., Wilcock, C. J., Miller, C. A., Moorehead, R. & Hatton, P. V. Process optimisation to control the physico-chemical characteristics of biomimetic nanoscale hydroxyapatites prepared using wet chemical precipitation. *Materials (Basel).* **8,** 2297–2310 (2015).

26. Milovac, D., Gallego Ferrer, G., Ivankovic, M. & Ivankovic, H. PCL-coated hydroxyapatite scaffold derived from cuttlefish bone: Morphology, mechanical properties and bioactivity. *Mater. Sci. Eng. C* **34,** 437–445 (2014).
27. Bogdanoviciene, I. *et al.* pH impact on the sol-gel preparation of calcium hydroxyapatite, Ca10(PO4)6(OH)2, using a novel complexing agent, DCTA. *Cent. Eur. J. Chem.* **8,** 1323–1330 (2010).
28. Panda, R. N., Hsieh, M. F., Chung, R. J. & Chin, T. S. X-ray diffractometry and X-ray photoelectron spectroscopy investigations of nanocrytalline hydroxyapatite synthesized by a hydroxide gel technique. *Japanese J. Appl. Physics, Part 1 Regul. Pap. Short Notes Rev. Pap.* **40,** 5030–5035 (2001).
29. Nikogosyan, D. N. *Nonlinear Optic Crystals: A Complete Survey*. (Springer-Vergal New York, 2005).
30. Muncherian, H. M. *Lasers and Optoelectronics Devices*. (Hemisphere Publishing, 1991).
31. Xue, D. & Ratajczak, H. Effect of hydrogen bonds on physical properties of ammonium dihydrogenphosphate crystals. *J. Mol. Struct. THEOCHEM* **716,** 207–210 (2005).
32. Xu, D. & Xue, D. Chemical bond analysis of the crystal growth of KDP and ADP. *J. Cryst. Growth* **286,** 108–113 (2006).
33. Dagys, L., Klimavicius, V. & Balevicius, V. Processing of CP MAS kinetics: Towards NMR crystallography for complex solids. *J. Chem. Phys.* **145,** (2016).
34. Ilardo, M., Meringer, M., Freeland, S., Rasulev, B. & Cleaves, H. J. Extraordinarily Adaptive Properties of the Genetically Encoded Amino Acids. *Sci. Rep.* **5,** 1–6 (2015).
35. Arthur, I. N. *et al.* In situ deprotection and incorporation of unnatural amino acids during cell-free protein synthesis. *Chem. - A Eur. J.* **19,** 6824–6830 (2013).
36. Wu, G. Amino acids: metabolism, functions, and nutrition. *Amino Acids* **37,** 1–17 (2009).
37. Fichtner, M., Voigt, K. & Schuster, S. The tip and hidden part of the iceberg: Proteinogenic and non-proteinogenic aliphatic amino acids. *Biochim. Biophys. Acta - Gen. Subj.* **1861,** 3258–3269 (2017).
38. O'Reilly, E., Pes, L., Ortin, Y., Müller-Bunz, H. & Paradisi, F. Synthesis of a conformationally constrained δ-amino acid building block. *Amino Acids* **44,** 511–518 (2013).
39. Ung, P. & Winkler, D. A. Tripeptide Motifs in Biology : Targets for Peptidomimetic Design. *J. Med. Chem.* **54,** 1111–1125 (2011).

40. Seebach, D., Beck, A. K. & Bierbaum, D. J. The World of beta- and gama-Peptides Comprised of Homologated Proteinogenic Amino Acids and Other Components. *Chem. Biodivers.* **1,** 1111–1239 (2004).
41. Garcia, A. M. *et al.* Chirality Effects on Peptide Self-Assembly Unraveled from Molecules to Materials Chirality Effects on Peptide Self-Assembly Unraveled from Molecules to Materials. *CHEM* **4,** 1–15 (2018).
42. Dehsorkhi, A., Castelletto, V. & Hamley, I. W. Self-assembling amphiphilic peptides. *J. Pept. Sci.* **20,** 453–467 (2014).
43. Sadatmousavi, P., Soltani, M., Nazarian, R., Jafari, M. & Chen, P. Self-Assembling Peptides: Potential Role in Tumor Targeting. *Curr. Pharm. Biotechnol.* **12,** 1089–1100 (2011).
44. Giannis, A. & Kolter, T. Peptidomimetics for Receptor Ligands - Discovery, Development, and Medical Perspectives. *Angew. Int. Ed. Chemie* **32,** 1244–1267 (1993).
45. Morita, S. Hydrogen-bonds structure in poly (2-hydroxyethyl methacrylate) studied by temperature-dependent infrared spectroscopy. *Front. Chem.* **2,** 1–5 (2014).
46. Roointan, A., Farzanfar, J., Mohammadi-samani, S. & Behzad-behbahani, A. Smart pH responsive drug delivery system based on poly (HEMA-co- DMAEMA) nanohydrogel. *Int. J. Pharm.* **552,** 301–311 (2018).
47. Liu, Q., Wijn, J. R. De & Blitterswijk, C. A. Van. Covalent bonding of PMMA, PBMA, and poly (HEMA) to hydroxyapatite particles. *J. Biomed. Mater. Res.* **40,** 21–24 (1997).
48. Schexnailder, P. & Schmidt, G. Nanocomposite polymer hydrogels. *Colloid Polym. Sci.* **287,** 1–11 (2009).
49. Brunsveld, L., Folmer, B. J. B., Meijer, E. W. & Sijbesma, R. P. Supramolecular Polymers. *Chem. Rev.* **101,** 4071–4097 (2001).
50. Moad, G., Rizzardo, E. & Thang, S. H. Radical addition - fragmentation chemistry in polymer synthesis. *Polymer (Guildf).* **49,** 1079–1131 (2008).
51. Edmondson, S., Osborne, V. L. & Huck, W. T. S. Polymer brushes via surface-initiated polymerizations. *Chem. Soc. Rev.* **33,** 14–22 (2004).
52. Flanders, M. J. & Gramlich, W. M. Reversible-addition fragmentation chain transfer (RAFT) mediated depolymerization of brush polymers. *Polym. Chem.* **9,** 2328–2335 (2018).
53. Radzevicius, P., Krivorotova, T. & Makuska, R. Synthesis by one-pot RAFT polymerization and properties of amphiphilic pentablock copolymers with repeating blocks of poly(2-hydroxyethyl

methacrylate) and poly(butyl methacrylate). *Eur. Polym. J.* **87,** 69–83 (2017).
54. Hammond, M. R. *et al.* Molecular Order in High-Efficiency Polymer / Fullerene Bulk Heterojunction Solar Cells. *Am. Chem. Soc. Nanomater.* **5,** 8248–8257 (2011).
55. Gali, M., Lewandowski, A. & St, I. Ionic liquids as electrolytes. **51,** 5567–5580 (2006).
56. Welton, T. Room-Temperature Ionic Liquids. Solvents for Sythesis and Catalysis. *Chem. Rev.* **99,** 2071–2083 (1999).
57. Peter, W. & Tom, W. *Ionic Liquids in Synthesis*. (Wiley-VCH, 2008).
58. Klimavicius, V., Dagys, L., Chizhik, V. & Balevicius, V. CP MAS Kinetics Study of Ionic Liquids Confined in Mesoporous Silica : Convergence of Non-Classical. *Appl. Magn. Reson.* **48,** 673–685 (2017).
59. Firestone, M. A., Thiyagarajan, P. & Tiede, D. M. Structure and Optical Properties of a Thermoresponsive Polymer-Grafted, Lipid-Based Complex Fluid. *Langmuir* **14,** 4688–4698 (1998).
60. Weingärtner, H. Ionic Liquids Understanding Ionic Liquids at the Molecular Level : Facts , Problems , and Controversies Angewandte. *Angew. Chemie* **47,** 654–670 (2008).
61. Noda, A. & Watanabe, M. Highly conductive polymer electrolytes prepared by in situ polymerization of vinyl monomers in room temperature molten salts. *Electrochim. Acta* **45,** 1265–1270 (2000).
62. Noda, A., Hayamizu, K. & Watanabe, M. Pulsed-gradient spin-echo 1H and 19F NMR ionic diffusion coefficient, viscosity, and ionic conductivity of non-chloroaluminate room-temperature ionic liquids. *J. Phys. Chem. B* **105,** 4603–4610 (2001).
63. Gómez-Cerezo, N. *et al.* Effects of a mesoporous bioactive glass on osteoblasts , osteoclasts and macrophages. *J. Colloid Interface Sci.* **528,** 309–320 (2018).
64. Monika, Š. Substituted hydroxyapatites for biomedical applications : A review. *Ceram. Int.* **41,** 9203–9231 (2015).
65. Kitagawa, S., Kitaura, R. & Noro, S. Coordination Polymers Functional Porous Coordination Polymers Angewandte. *Angew. Chemie - Int. Ed.* **43,** 2334–2375 (2004).
66. Hutmacher, D. W. *Scaffolds in tissue engineering bone and cartilage*. *The Biomaterials Silver Jubilee Compendium* **21,** (Woodhead Publishing Limited, 2000).
67. Sader, M. S., Lewis, K., Soares, G. A. & Legeros, R. Z. Simultaneous Incorporation of Magnesium and Carbonate in Apatite : Effect on

Physico-chemical Properties. *Mater. Res.* **16,** 779–784 (2013).
68. He, W. *et al.* Formation of bone-like nanocrystalline apatite using self-assembled liquid crystals. *Chem. Mater.* **24,** 892–902 (2012).
69. Hayakawa, S. *et al.* Heterogeneous structure and in vitro degradation behavior of wet-chemically derived nanocrystalline silicon-containing hydroxyapatite particles. *Acta Biomater.* **9,** 4856–4867 (2013).
70. Zhao, Y. *et al.* Hierarchically porous and heteroatom doped carbon derived from tobacco rods for supercapacitors. *J. Power Sources* **307,** 391–400 (2016).
71. Sukhishvili, S. A. & Granick, S. Layered, erasable polymer multilayers formed by hydrogen-bonded sequential self-assembly. *Macromolecules* **35,** 301–310 (2002).
72. Oh, S. Y. *et al.* Crystalline structure analysis of cellulose treated with sodium hydroxide and carbon dioxide by means of X-ray diffraction and FTIR spectroscopy. *Carbohydr. Res.* **340,** 2376–2391 (2005).
73. Stončius, S. *et al.* An approach to helical tubular self-aggregation using C2- symmetric self-complementary hydrogen-bonding cavity molecules. *J. Am. Chem. Soc.* **128,** 8272–8285 (2006).
74. Burge, S., Parkinson, G. N., Hazel, P., Todd, A. K. & Neidle, S. Quadruplex DNA: Sequence, topology and structure. *Nucleic Acids Res.* **34,** 5402–5415 (2006).
75. Arachchige, R. J. *et al.* Article Solid-State NMR Identification of Intermolecular Interactions in Amelogenin Bound to Hydroxyapatite. *Biophys. J.* **115,** 1666–1672 (2018).
76. Dill, J. *et al.* Lack of OH in nanocrystalline apatite as a function of degree of atomic order : implications for bone and biomaterials. *Biomaterials* **25,** 229–238 (2004).
77. Lei, S., Shi, Y., Qiu, Y., Che, L. & Xue, C. Science of the Total Environment Performance and mechanisms of emerging animal-derived biochars for immobilization of heavy metals. *Sci. Total Environ.* **646,** 1281–1289 (2019).
78. Li, Y., Reid, D. G., Duer, M. J. & Chan, J. C. C. Solid state NMR - An indispensable tool in organic-inorganic biocomposite characterization; refining the structure of octacalcium phosphate composites with the linear metabolic di-acids succinate and adipate. *Solid State Nucl. Magn. Reson.* **95,** 1–5 (2018).
79. Senol, S. & Akyol, E. Biomaterials Synthesis and characterization of hydrogels based on poly (2-hydroxyethyl methacrylate) for drug delivery under UV irradiation. *J. Mater. Sci.* **53,** 14953–14963 (2018).
80. Rivas, M., Valle, J., Armelin, E., Bertran, O. & Turon, P.

Hydroxyapatite with Permanent Electrical Polarization : Preparation, Characterization, and Response against Inorganic Adsorbates. *J. Chem. Phys. Phys. Chem.* **19,** 1746–1755 (2018).

81. Ostadhossein, F., Benig, L., Tripathi, I., Misra, S. K. & Pan, D. Fluorescence Detection of Bone Microcracks Using Monophosphonated Carbon Dots. *ACS Appl. Mater. Interfaces* **10,** 19408–19415 (2018).
82. David, G. *et al.* Squalene/polyethylenimine based non-viral vectors: synthesis and use in systems for sustained gene release. *Polym. Chem.* **9,** 1072–1081 (2018).
83. Iline-vul, T. *et al.* Current Opinion in Colloid & Interface Science Understanding the roles of functional peptides in designing apatite and silica nanomaterials biomimetically using NMR techniques. *Curr. Opin. Colloid Interface Sci.* **33,** 44–52 (2018).
84. Manatunga, D. C., Silva, R. M., Silva, K. M. N., Silva, N. & Premalal, E. V. A. Metal and polymer-mediated synthesis of porous crystalline hydroxyapatite nanocomposites for environmental remedation. *R. Soc. Open Sci.* **5,** 17557 (15) (2018).
85. Usami, K. & Okamoto, A. Hydroxyapatite: catalyst for a one-pot pentose formation. *Org. Biomol. Chem.* **15,** (2017).
86. Soss, S. E. *et al.* Measuring and Modeling Highly Accurate 15 N Chemical Shift Tensors in a Peptide . *J. Chem. Phys. Phys. Chem.* **18,** 2225–2232 (2017).
87. Manu, V. S. & Veglia, G. Optimization of identity operation in NMR spectroscopy via genetic algorithm : Application to the TEDOR experiment. *J. Magn. Reson.* **273,** 40–46 (2016).
88. Gibbs, E. B. & Kriwacki, R. W. Direct detection of carbon and nitrogen nuclei for high-resolution analysis of intrinsically disordered proteins using NMR spectroscopy. *Methods* **138–139,** 39–46 (2018).
89. Davies, E. *et al.* Citrate bridges between mineral platelets in bone. *Proc. Natl. Acad. Sci.* **111,** 1–10 (2014).
90. Ben Osman, M. *et al.* Discrimination of Surface and Bulk Structure of Crystalline Hydroxyapatite Nanoparticles by NMR. *J. Phys. Chem. C* **119,** 23008–23020 (2015).
91. Martineau-Corcos, C. NMR Crystallography: A tool for the characterization of microporous hybrid solids. *Curr. Opin. Colloid Interface Sci.* **33,** 35–43 (2018).
92. Levitt, M. H. *Spin dynamics*. (John Wiley and Sons, 2008).
93. Keeler, J. *Understanding NMR spectroscopy*. (Wiley-Blackwell, 2010).

94. Haeberlen, U. *High Resolution NMR in Solids. Selective Averaging*. (Academic Press, 1976).
95. Callaghem, P. T. *Principles of Nulcear Magnetic Resonance Microscopy*. (Oxford University Press, 1993).
96. Duer, M. J. *Solid-State NMR spectroscopy. Principals and application.* (Blackwell science, 2002).
97. Hartmann, S. R. & Hahn, E. L. Nuclear double resonance in the rotating frame. *Phys. Rev.* **128,** 2042–2053 (1962).
98. Naito, A. & McDowell, C. A. Anisotropic behavior of the 13C nuclear spin dynamics in a single crystal of L-alanine. *J. Chem. Phys.* **84,** (1998).
99. Levitt, M. H., Suter, D. & Ernst, R. R. Spin dynamics and thermodynamics in solid-state NMR cross polarization. *J. Chem. Phys.* **84,** 4243–4255 (1986).
100. Alemany, L. B., Grant, D. M., Alger, T. D. & Pugmire, R. J. Cross Polarization and Magic Angle Sample Spinning NMR Spectra of Model Organic Compounds. 3. Effect of the 13C-1H Dipolar Interaction on Cross Polarization and Carbon-Proton Dephasing. *J. Am. Chem. Soc.* **105,** 6697–6704 (1983).
101. Bengs, C. & Levitt, M. H. SpinDynamica: Symbolic and numerical magnetic resonance in a Mathematica environment. *Magn. Reson. Chem.* **56,** 374–414 (2018).
102. Klimavicius, V., Kareiva, A. & Balevicius, V. Solid-State NMR Study of Hydroxyapatite Containing Amorphous Phosphate Phase and Nanostructured Hydroxyapatite: Cut-Off Averaging of CP-MAS Kinetics and Size Profiles of Spin Clusters. *J. Phys. Chem. C* **118,** 28914–28921 (2014).
103. Vyalikh, A. *et al.* Intergrowth and Interfacial Structure of Biomimetic Fluorapatite − Gelatin Nanocomposite: A Solid-State NMR Study. (2014). doi:10.1021/jp410299x
104. Thrippleton, M. J., Cutajar, M. & Wimperis, S. Magic angle spinning (MAS) NMR linewidths in the presence of solid-state dynamics. *Chem. Phys. Lett.* **452,** 233–238 (2008).
105. Ando, S., Harris, R. K. & Reinsberg, S. A. Analysis of Cross-Polarization Dynamics between Two Abundant Nuclei , 19F and 1H , Based on Spin Thermodynamics Theory. *J. Ma* **141,** 91–103 (1999).
106. Kaflak-Hachulska, A., Samoson, A. & Kolodziejski, W. Calcified Tissue International 1H to 31P CP / MAS NMR Study of Human Bone Mineral. *Calcif. Tissue Int.* **73,** 476–486 (2003).
107. Kolmas, J., Jablonski, M., Slosarczyk, A. & Kolodziejski, W. Solid-

State NMR Study of Mn2+ for Ca2+ Substitution in Thermally Processed Hydroxyapatites. *J. Amrecian Ceram. Soc.* **98,** 1265–1274 (2015).
108. Klimavičius, V. Solid state NMR spectroscopy of complex innovative materials. (Vilnius University, 2017).
109. Mali, G. & Kaučič, V. Determination of distances between aluminum and spin-1/2 nuclei using cross polarization with very weak radio-frequency fields. *J. Chem. Phys.* **117,** 3327–3339 (2002).
110. Holland, G. P. *et al.* NMR Characterization of Phosphonic Acid Capped SnO 2 Nanoparticles. *Chem. Mater.* **19,** 2519–2526 (2007).
111. Kolmas, J. *et al.* Incorporation of carbonate and magnesium ions into synthetic hydroxyapatite : The effect on physicochemical properties. *J. Mol. Struct.* **987,** 40–50 (2011).
112. Welzel, T., Meyer-zaika, W., Epple, M. & Christian, J. A solid-state NMR investigation of the structure of nanocrystalline hydroxyapatite. 573–580 (2006). doi:10.1002/mrc.1774
113. Welzel, T., Meyer-zaika, W., Epple, M. & Christian, J. A solid-state NMR investigation of the structure of nanocrystalline hydroxyapatite. *Magn. Reson. Chem.* **44,** 573–580 (2006).
114. Fyfe, C. A., Lewis, A. R. & Chezeau, J. M. A comparison of NMR distance determinations in the solid state by cross polarization, REDOR, and TEDOR techniques. *Can. J. Chem. Can. Chim.* **77,** 1984–1993 (1999).
115. Tenzer, L., Frazer, B. C. & Pepinsky, R. A neutron structure analysis of tetragonal NH4(H2PO4). *Acta Crystallogr.* **11,** 505–509 (1958).
116. Pérès, N. *et al.* Neutron diffraction study of the paraelectric phase of ammonium dihydrogen phosphate (ADP): hydrogen bonding of. *J. Phys. Condens. Matter* **9,** 6555–6562 (1999).
117. Groot, C. P. De, Ladizhansky, V., Vega, S. & Groot, H. J. M. De. A Method for Measuring Heteronuclear (1H - 13C) Distances in High Speed MAS NMR. *J. Am. Chem. Soc.* **122,** 3465–3472 (2000).
118. Aree, T. & Bu, H. Dynamics and Thermodynamics of Crystalline Polymorphs : α - Glycine , Analysis of Variable-Temperature Atomic Displacement Parameters. *J. Phys. Chem. A* **116,** 8092–8099 (2012).
119. Lorieau, J. L. & Mcdermott, A. E. Conformational Flexibility of a Microcrystalline Globular Protein: Order Parameters by Solid-State NMR Spectroscopy. *J. Am. Chem. Soc.* **128,** 11505–11512 (2006).
120. Moggach *et al.* Effect of pressure on the crystal structure of L-serine-I and the crystal structure of L-serine-II at 5.4GPa. *Acta Crystallogr. Sect. B* **61,** 58–68 (2005).

121. Suresh, S., Padmanabhan, S. & Vijayan, M. DL-Glutamine. *Acta Crystallogr. Sect. C* **52,** 1313–1316 (1996).
122. Yamada, K., Hashizuma, D., Shimizu, T. & Yokoyama, S. L-Asparagine. *Acta Crystallogr. Sect. E* **63,** 3802–3803 (2007).
123. Dunitz, J. D. & Schweizer, W. B. Anhydrous DL-Glutamic Acid. *Acta Crystallogr. Sect. C* **51,** 1377–1379 (1995).
124. Madden, J. J., McGandy, E. L., Seeman, N. C., Harding, M. M. & Hoy, A. The crystal structure of the monoclinic form of L-histidine. *Acta Crystallogr. Sect. B* **28,** 2382–2389 (1972).
125. Dalhus, B. & Görbitz, C. H. Triclinic Form of DL-Valine. *Acta Crystallogr. Sect. C* **52,** 1759–1761 (1996).
126. Janczak, J., Zobel, D. & Luger, P. L-Threonine at 12K. *Acta Crystallogr. Sect. C* **52,** 1901–1904 (1997).
127. Moggach *et al.* High-pressure polymorphism in L-cysteine: the crystal structures of L-cysteine-III and L-cysteine-IV. *Acta Crystallogr. Sect. B* **62,** 296–309 (2006).
128. Dalhus, B. & Görbitz, C. H. Molecular aggregation in crystalline 1:1 complexes of hydrophobic D- and L-amino acids. I. The L-isoleucine series. *Acta Crystallogr. Sect. B* **55,** 424–431 (1999).
129. Sunnie, M., Maren, P., Baik, M. H. & Clemmer, D. E. DL-Proline. *Acta Crystallogr. Sect. C* **61,** 506–508 (2005).
130. Tumanov, N. A., Boldyreva, E. V., Kolesov, B. A. & Cabrera-Quesada, R. Pressure-induced phase transitions in L-alanine, revisited. *Acta Crystallogr. Sect. B* **66,** 458–471 (2010).
131. Saalwächter, K. & Spiess, H. W. *Solid-State NMR of Polymers*. *Polymer Science: A Comprehensive Reference, 10 Volume Set* **2,** (Elsevier B.V., 2012).
132. Hediger, S. Improvement of Heteronuclear POlarization Transfer in Solid-State NMR. (ETH-Zurich, 1997).
133. Feldman, Y., Puzenko, A. & Ryabov, Y. Non-Debye dielectric relaxation in complex materials. *Chem. Phys.* **284,** 139–168 (2002).
134. Raya, J. & Hirschinger, J. Sensitivity enhancement by multiple-contact cross-polarization under magic-angle spinning. *J. Magn. Reson.* **281,** 253–271 (2017).
135. Yashima, M. *et al.* Diffusion Path and Conduction Mechanism of Porotns in Hydroxyapatite. *J. Phys. Chem. C* **118,** 5180–5187 (2014).
136. Grünberg, B. *et al.* Hydrogen Bonding of Water Confined in Mesoporous Silica MCM-41 and SBA-15 Studied by 1H Solid-State NMR. *Chem. - A Eur. J.* **10,** 5689–5696 (2004).

APPENDIX

Table A1. Main NMR parameters for time kinetics measurements of cross-polarization in various samples.

Sample	D1 (s)	^{1}H RF (kHz)	CP contact pulse power setting for ^{1}H/X channels (W)	Number of scans	MAS rate (kHz)	CP contact time range (μs)	Number of CP contact time points
ADP	0.5	~100	Var. (X = ^{31}P)	1	7/10	50–10000	~500
CaHA	4	~90	Var. (X = ^{31}P)	2	0/5/9	50–10000	~500
GFG	2	~68	48.9/120.0 (X = ^{13}C)	128	12	10–3000	~300
GGG	1.5	~68	48.9/120.0 (X = ^{13}C)	32	12	10–3000	~300
L-Ala	1	~71	44.2/156.7 (X = ^{13}C)	4	10	10–10000	~1000
L-Arg	12	~71	48.3/150.0 (X = ^{13}C)	8	10	10–10000	~1000
L-Asn	15	~71	50.4/120.0 (X = ^{13}C)	6	10	10–10000	~1000
L-Cys	4	~71	48.6/156.7 (X = ^{13}C)	4	10	10–10000	~1000
L-Gln	40	~71	50.5/150.0 (X = ^{13}C)	4	10	10–10000	~1000
L-Gln	15	~71	48.4/120.0 (X = ^{13}C)	4	10	10–10000	~1000
Gly	Var	~71	Var. (X = ^{13}C)	4	7/10/12	10–10000	~1000
L-His	4.5	~71	50.4/120.0 (X = ^{13}C)	16	10	10–10000	~1000
L-Ile	3	~71	50.4/110.8 (X = ^{13}C)	8	10	10–10000	~1000
L-Leu	1.5	~71	48.6/135.4 (X = ^{13}C)	16	10	10–10000	~1000
L-Met	2	~71	47.4/145.2 (X = ^{13}C)	4	10	10–10000	~1000
L-Pro	7	~71	50.4/150.0 (X = ^{13}C)	16	10	10–10000	~1000
L-Ser	2	~71	47.7/120.0 (X = ^{13}C)	2	10	10–10000	~1000
L-Thr	1	~71	47.4/107.6 (X = ^{13}C)	8	10	10–10000	~1000
L-Tyr	10	~71	58.5/156.7 (X = ^{13}C)	16	10	10–10000	~1000
L-Val	1	~71	41.4/110.8 (X = ^{13}C)	16	10	10–10000	~1000
pHEMA	2.7	~71	46.2/120.0 (X = ^{13}C)	128	10	20–10000	~500
pVPA	3	~71	44.5/104.2 (X = ^{31}P)	4	10	10–10000	~1000
RTIL	2	~80	– (X = ^{11}B)	256	5	50–10000	~128

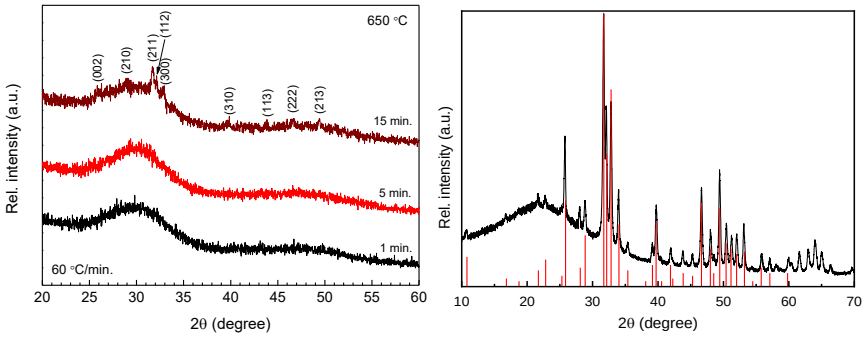

Figure A1. XRD patterns of ACP-CaHA depending on the sintering time at 650˚C – on the left. Nano-CaHA XRD pattern on the right.

SANTRAUKA

S1. ĮŽANGA

Funkcinių medžiagų tyrimai ir taikymai yra neatsiejami nuo medžiagotyros mokslų, tokių kaip kristalografija, kuriais analizuojama struktūra ir su ja susijusios savybės[2–4]. Todėl, vis didėjantis susidomėjimas naujomis medžiagomis taip pat reikalauja lygiaverčio metodų tobulėjimo.

Pagrindiniais kristalografijos auksiniais standartais yra laikomi tokie difrakciniai metodai kaip Rentgeno spindulių difrakcija ar neutronų difrakcija, kadangi šiais metodais nustatomi atstumai tarp objektų yra itin maži, angstremų eilės – tai leidžia gana paprastai nustatyti struktūrą medžiagos kristalinėje gardelėje. Nepaisant to, šiais metodais tiriant lengvųjų atomų pasiskirstymą ir ypač netvarkiose medžiagose yra sutinkamos fizikinės ribos, kuomet bangų difrakcija paranda pranašumą. Tokiu atveju naudojant spektroskopinius įrankius papildomai galima nusakyti medžiagos sudėtį ir dinaminius vyksmus bei idealiai tvarkios medžiagos dažnai nėra būtinybė [5–7].

Branduolių magnetinis rezonansas (BMR) turbūt yra bene lanksčiausias spektrometrinis įrankis, leidžiantis tirti medžiagas įvairiais jų aspektais. Nagrinėjant medžiagas kristalografijos rėmuose, BMR spektrometrija neretai siejama su metodais, kuriuose panaudojama dipolinė sąveika, kadangi pastaroji glaudžiai susijusi su atstumu tarp sąveikaujančių branduolių sukinių. Vienas iš tokių eksperimentų yra kryžminė poliarizacija (cross-polarization – CP). Paprastai ši metodika naudojama sustiprinti mažiau jautresnių izotopų signalus, tačiau jos vidinė laikinė dinamika yra kompleksinis reiškinys, nulemtas medžiagos struktūrinių sąvybių[8,15,91].

Šio kompleksinio reiškinio matematinis aprašymas yra bene svarbiausias uždavinys analizuojant laikines CP kinetikas, ypač jas aprašant plačioje struktūrinėje įvairovėje. Pagrindiniai net ir dabar naudojami modeliai aprašantys CP jau buvo pristatyti septintame dešimtmetyje, tačiau dažnai jie yra per daug supaprastinti ir modeliavimais jais gali lemti nekorektišką interpretaciją[8,18]. Taigi, geresnis modelių supratimas didelėje struktūrinėje įvairovėje būtų svarbus indėlis šio BMR metodo plėtojimui kristalografijoje, suteiktų daugialypės informacijos apie reiškinius medžiagose ir taip išpildytų vis tobulėjančių analizės metodų funkcinių medžiagų moksle poreikį.

Disertacijos tikslas ir keliami uždaviniai

Įžangoje pabrėžti iššūkiai susiję su kryžminės-poliarizacijos naudojimu skirtose kietojo kūno struktūrose kildina šio darbo tikslą – išplėtoti CP kinetikų apdorojimą didelėje funkcinių medžiagų įvairovėje. Šiam tikslui pasiekti keliamos užduotys:

1. Ištirti ^{1}H ir ^{31}P BMR taikymo galimybes analizuojant kompleksinių medžiagų, tokių kaip kalcio hidroksiapatitas, struktūras.
2. Pritaikyti kryžminės poliarizacijos kinetikų tyrimus kompleksinėse medžiagose.
3. Palyginti CP kinetikų modeliavimo tikslumą su plačiai naudojamų kristalografijos metodų rezultatais
4. Pritaikyti kinematinį modeliavimą organinėse medžiagose bei kitiems CP (sukininiams) partneriams.
5. Surasti tinkamus modelius aprašančius CP dinamiką didelėje struktūrinių medžiagų įvairovėje bei stebimame laikiniame diapazone.

Ginamieji teiginiai

1. ^{1}H ir ^{31}P BMR taikymas su magiškojo kampo sukimo technika yra metodas atskleidžiantis kompleksinių medžiagų sandarą ir struktūrinę sąrangą.
2. Kryžminės poliarizacijos makroskopiniai parametrai gali būti apskaičiuoti naudojant bendrinius CP modelius, tuo tarpu detali struktūrinė informacija yra prieinama analizuojant pradines (koherentines) CP osciliacijas.
3. *Fourier-Bessel* transformacijos taikymas leidžia įskaityti dipolinės sąveikos kampinį vidurkinimą, kuris privalomas norinti apskaičiuoti tik nuo atstumo priklausantį dipolinės sąveikos pasiskirstymą.
4. Silpnai ir stipriai surišti sukiniai pasižymi itin skirtinga kryžmine poliarizacija, vadinasi taikomi modeliai turi būti lankstūs.
5. Sukinių difuzijos nulemtas terminis nusistovėjimas paplitusių sukinių posistemėje daro įtaką tolimųjų sąveikaujančių sukinių kryžminei poliarizacijai.

Mokslinis naujumas

1. Pasinaudojus keliomis prielaidomis buvo atlikta *Fourier-Bessel* transformacija, kuri leido įskaityti dipolinės sąveikos kampinį vidurkinimą. Tai leido apskaičiuoti visiškai tik nuo atstumo priklausantį dipolinės sąveikos pasiskirstymą.
2. Šiame darbe buvo išplėtoti kryžminės poliarizacijos modeliai aprašantys dinamiką plačioje struktūrinėje įvairovėje taip pat visame stebimame laikiniame diapazone.
3. Sukinių difuzijos spartos priklausomybė nuo protonų tankio kristalinėje gardelėje buvo stebėta pirmą kartą.
4. Žymus signalo ir triukšmo santykio sustiprinimas buvo pasiektas pritaikius naują interaktyvios apodizacijos kinetikų analizės metu metodą.
5. Visiškas CP modelio sutapimas buvo pasiektas tolimųjų sąveikaujančių sukinių atveju, kuomet buvo įtrauktos papildomos prielaidos aprašančios sukinių difuziją paplitusių sukinių posistemėje. Tai leido pritaikyti kryžminės poliarizacijos matavimus tiriant struktūrų fraktališkumą.

Autoriaus indėlis

Kalcio hidroksiapatito ir polimerinio hidrogelio sintezė taip pat SEM ir XRD matavimai buvo atlikti Vilniaus universiteto Chemijos fakultete, tuo tarpu tripeptidai buvo sintetinami Darmštato Technikos universitete, Vokietijoje. Kalcio hidroksiapatito virpesiniai spektrai buvo užregistruoti kolegų iš Cheminės fizikos instituto. Darbe bei publikacijose naudojami DFT skaičiavimai atlikti dr. Kestučio Aido. Visi BMR matavimai naudojami šiame darbe buvo atlikti autoriaus su pradiniu dr. Vytauto Klimavičaus kuravimu. Duomenų analizė, apdorojimas, matematiniai išvedimai buvo atlikti tiek savarankiškai tiek kartu su darbo vadovu. Publikacijos buvo parengtos darnioje komandoje su bendraautoriais. Autorius pabrėžia, jog šis rašto darbas dalinai persikloja su dr. V.Klimavičiaus disertacija, kadangi pagrindinės idėjos buvo plėtojamos toje pačioje grupėje. Nepaisant to, šis darbas gali būti laikomas pirminės disertacijos išplėtojimu didelėje imtyje naujų medžiagų.

S2. DISERTACIJOS REZULTATAI

Charakterizavimas naudojant 1D spektrometriją

Pirminės šio darbo idėjos atsirado tiriant kalcio hidroksiapatito (CaHA), kaip funkcinės medžiagos, struktūrą bei sandarą[11]. Šiame darbe yra išskiriami du apatito bandiniai, kurie pasižymi skirtinga morfologija. Vienas jų yra amorfinių fosfato grupių turintis (ACP) apatitas, kitas – nano-struktūrizuotas (nano-). Šioms medžiagoms buvo užrašyti ^{1}H BMR bei FTIR spektrai (S.1 pav.).

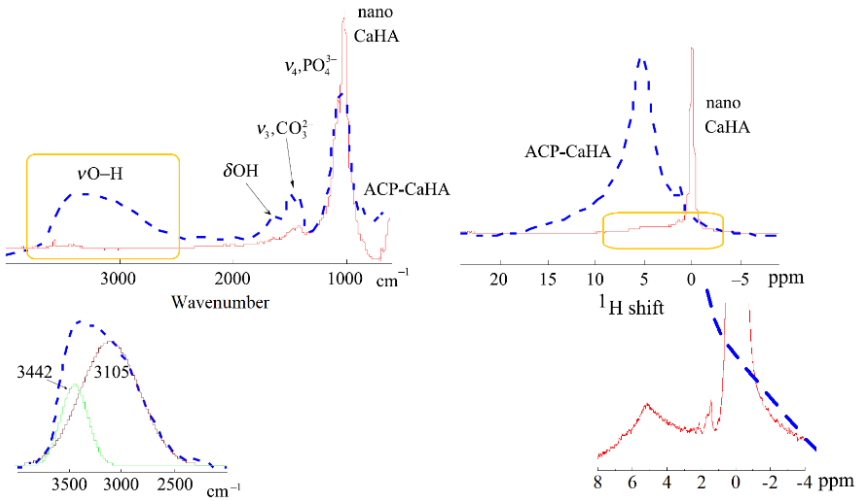

S.1 pav. FTIR bei ^{1}H BMR spektrų palyginimas dviejų bandinių: ACP-CaHA ir nano-CaHA atveju. Geltoni rėmeliai žymi išdidintas sritis matomas apačioje. FTIR spektrinių juostų priskyrimas atliktas šaltinyje [11].

Pirmiausia, yra pastebimi dideli skirtumai susiję su laisvojo vandens signalais. FTIR spektre yra matoma, jog ties ~3300 cm^{-1} valentiniai OH virpesiai sudaro didelę dalį amorfinio kalcio hidroksiapatito juostų, kuomet šios juostos nebuvimas nano-struktūrizuotame CaHA leidžia aptikti struktūrinių (P-OH) grupių valentinius virpesius ties 3572 cm^{-1}. Laisvojo arba ant paviršiaus adsorbuoto vandens kiekis taip pat gali būti patvirtintas iš BMR spektrų, kuriuose tipinė tūrinio vandens juosta ties 4.5 ppm yra beveik nepastebima nano-struktūrizuotojo CaHA.

Kita vertus, taip pat tinkamas būdas tirti šias kompleksines medžiagas yra ^{31}P BMR – galima rasti nemažai darbų, kuriuose šie izotopai tirti panašiose fosfatinėse grupėse[69,103]. Paprastai, pagrindinė spektrinė BMR juosta atsiranda dėl PO_4^{3-} grupių, tuo tarpu juostos plotis yra sąlygotas amorfinių fosfato grupių

dalelių paviršiuje. Šios grupės ne tik nulemia didelį juostos plotį, tačiau ir turi nemažą įtaką jos simetriškumui. Santykinai didelis ^{31}P juostos plotis buvo nustatytas ACP-CaHA bandiniui. Juostos puspločio priklausomybė nuo magiškojo kampo sukimo greičio yra pavaizduota S.2 paveiksle.

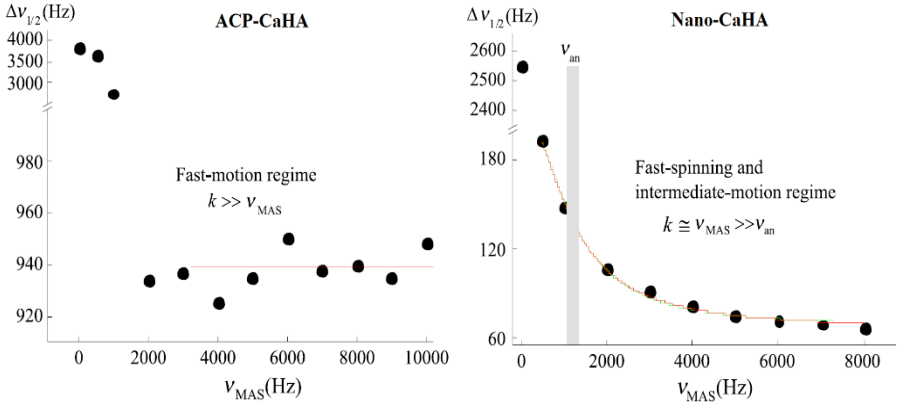

S.2 pav. Fosforo BMR juostos puspločio priklausomybė nuo magiškojo kampo sukimo greičio. Pilkas brūkšnys žymi ν_{an} vertę, kuomet sukimas tampa efektyvus.

Magiškojo kampo sukimas (MAS) efektyviai gali suvidurkinti įvairias nepageidaujamas sąveikas, tačiau jeigu sąveika nulemia vienalytiškai išplitusią juosta, ją susiaurinti tampa techniškai sudėtinga[104]. Deja, visi medžiagos paviršiuje esantys netolygumai nulemia Gausinį išplitimą, kurio plotis priklauso nuo sąveikų stiprumo.

Minėtos sąveikos sukelia chaotinius persiorientavimus, kurių sparta nulemia Gausinio išplitimo priklausomybę nuo MAS dažnio. Dėl staigaus puspločio pasikeitimo ACP-CaHA bandinyje galima teigti, jog chaotinių persiorientavimų sparta yra daug didesnė už sukimo dažnį, kai nano-CaHA bandinyje ji yra palyginama.

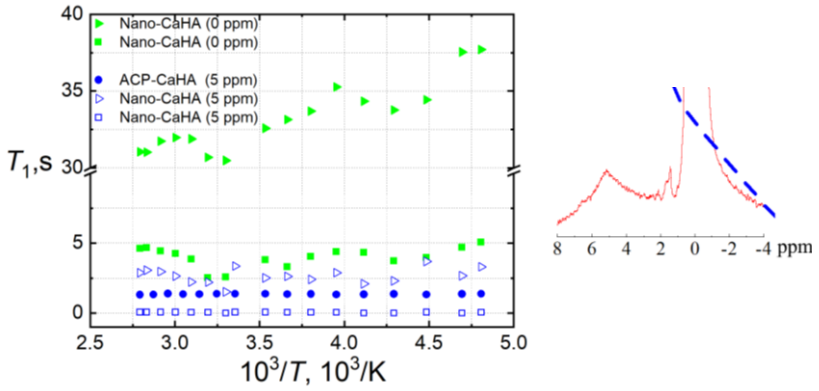

S.3 pav. Išilginės ^{1}H branduolių relaksacijos trukmės priklausomybė nuo atvirkštinės temperatūros. Dėl eksponentinės relaksacijos nano-struktūrizuotame bandinyje atskirai pavaizduotos dedamosios (trikampiais ir kvadratais). Dešinėje – spektras kuriame matomos atskiros juostos.

Chaotinių procesų sparta taip pat gali būti susieta su išilgine branduolių relaksacija. Šiai spartai esant didesnei, didėja tikimybė, jog sparta atitiks rezonansinį sukinių dažnį, o tai lemtų spartų artėjimą prie pusiausvyros būsenos. Todėl, iš S.3 paveikslo galima patvirtinti, jog amorfiniame bandinyje vykstantys chaotiniai persiorientavimai yra susiję su adsorbuoto vandens molekulėmis ir žymiai spartesni nei fluktuacijos vykstančios struktūrinėse -OH grupėse.

Išvados

- BMR bei FTIR juostų priskyrimas rodo, jog amorfiniame kalcio hidroksiapatite didžioji dalis vandens yra adsorbuota paviršiuje, tuo tarpu dominuojantis kiekis struktūrinės -OH grupės buvo aptiktas nano-struktūrizuoto apatito atveju.
- Magiškojo kampo sukimo technika bei relaksacijos spartų matavimai patvirtina, jog amorfiniame apatite vyksta spartūs chaotiniai persiorientavimai.
- Rutininė BMR spektrometrija gali suteikti informacijos susijusios su kompleksinių medžiagų sandara bei dinaminių vyksmų spartomis.

Kryžminė poliarizacija kalcio hidroksiapatite

Kryžminės poliarizacijos kinetinės kreivės kalcio hidroksiapatite pavaizduotos S.4 bei S.5 paveiksluose. Pirmas pastebimas kryžminės poliarizacijos skirtumas nano-struktūrizuotame bandinyje yra pradinės osciliacijos, kurios nepastebimos amorfinio bandinyje. Šios osciliacijas galima paaiškinti pasinaudojus I-I*-S modeliu, kuris buvo išvestas paaiškinti CP osciliacijas kietuose kristaluose[19,98]. Jis aprašomas tokia funkcija:

$$M(t) = \mathrm{e}^{-t/T_{1\rho,I}} \frac{\mathcal{B}}{4}\left(1 - \frac{1}{2}\mathrm{e}^{-R\,t} - \frac{1}{2}\mathrm{e}^{-3R\frac{t}{2}}\cos\frac{b_{IS}\,t}{2}\right) \qquad \text{(S.1)}$$

kur R yra sukinių difuzija, b_{IS} – dipolinė sąveika tarp dviejų skirtingų sukinių, $T_{1\rho}$ – sukinių išilginė relaksacija besisukančioje koordinačių sistemoje bei B yra *Boltzmann* faktorius. Žinoma, jog darbe tyrinėtais atvejais medžiagos laikyti idealiu kristalu yra neįmanoma.

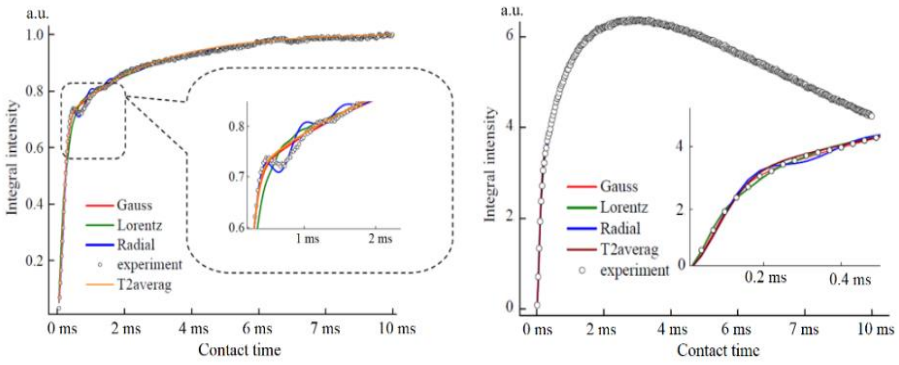

S.4 pav. $^{1}H \rightarrow ^{31}P$ CP kinetika (integrinio intensyvumo priklausomybė nuo kontaktinio impulso trukmės) statiniuose nano-CaHA (kairėje) ir ACP-CaHA (dešinėje) bandiniuose. Kreivių modeliavimas buvo atliktas naudojant bendrines $P(b/2)$ formas: Gauso, Lorenco, spindulinė bei T2-vidurkio. Daugiau detalių aprašyta tekste.

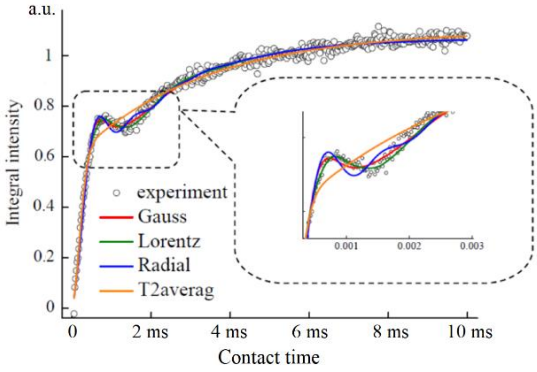

S.5 pav. $^{1}H \rightarrow ^{31}P$ CP-MAS (9 kHz) kinetika nano-struktūrizuotame hidroksiapatite. Kreivės buvo aproksimuojamos tokiomis pačiomis funkcijomis kaip S.4 paveiksle.

Todėl, atsižvelgus į galimybę, jog bandinyje esama įvairiais atstumais pasiskirsčiusių sąveikaujančių sukinių, dipolinės sąveikos nulemtos osciliacijos (kosinuso funkcija) bus visų dažnių vidurkis. Išraiškoje tai galima išreikšti taip:

$$I(t) = I_0 \mathrm{e}^{-t/T_{1\rho,I}} \left(1 - \lambda \mathrm{e}^{-R\,t} - (1-\lambda)\mathrm{e}^{-3R\frac{t}{2}} \cdot \sum P\left(\frac{b_i}{2}\right) \cos\left(\frac{2\pi\, b_i\, t}{2}\right)\right) \quad \text{(S.2)}$$

Čia $P(b/2)$ yra nežinomos formos pasiskirstymas, kuris gali būti pasirenkamas modeliavimo metu. Vienas iš galimų pasiskirstymų yra spindulinis pasiskirstymas (angl. *radial* – R), kuris tikimybiškai nusako kiek galimų sukinių yra aplinkui vieną centrą. Kiek paprastesnė prielaida (net už Gauso ir Lorenco paskirstymą) yra laikytis artėjimo, jog bandinys yra tiek netvarkus, jog jame kosinuso funkcijų suma artėja prie gausinio skirstinio. Tai buvo pademonstruota *L.B Alemany* ir vėliau papildyta *W. Kolodzieski* publikacijoje[18,100]. Tuomet išraišką galima perrašyti kiek paprasčiau:

$$I(t) = I_0 \mathrm{e}^{-t/T_{1\rho,I}} \left(1 - \lambda \mathrm{e}^{-R\,t} - (1-\lambda)\mathrm{e}^{-3R\frac{t}{2}} \cdot \mathrm{e}^{\frac{-t^2}{2\,T_2^2}}\right) \quad \text{(S.3)}$$

čia T_2 laikytinas $b_{IS}/2$ kvadratų vidurkiu, o $\lambda = 1/(N+1)$ nusako klasterio dydį, kai N yra ne-ekvivalenčių sąveikaujančių sukinių skaičius. Aproksimavimo rezultatai naudojant minėtas funkcijas yra pateikti 1 lentelėje.

S1 lentelė. CP kinetikų netiesinio aproksimavimo rezultatai grafiškai pavaizduoti S.4 bei S.5 paveiksluose[12].

Nano-struktūrizuotas kalcio hidroksiapatitas								
	Statiškas bandinys				MAS, 9 kHz			
$P(b)$	R	G	L	T_2-v.	R	G	L	T_2-v.
λ	0.39	0.30	0.39	0.33	0.61	0.60	0.60	0.47
R_{diff}, 1/s	455	385	455	400	476	455	455	313
b_0, Hz		0	320			800	885	
w, Hz		1920	1290			850	590	
T_2, ms				0.24				0.28
b_{max}, Hz	3500				2200			
b_{min}, Hz	330				740			
$T_{1\rho}$	∞							
χ^2, ‰	7	14	7	8	18	16	15	20
Amorfinis kalcio hidroksiapatitas								
	Statiškas bandinys				MAS, 5 kHz			
$P(b)$	R	G	L	T_2-v.	R	G	L	T_2-v.
λ	0.69	0.64	0.65	0.69	0.8	0.73	0.75	0.70
R_{diff}, 1/s	769	715	715	715	1111	1111	1111	1000
b_0, Hz		0	0			0	0	
w, Hz		4600	2500			2500	1400	
T_2, ms				0.12				0.34
b_{max}, Hz	7600				2400			
b_{min}, Hz	470				540			
$T_{1\infty}$	0.015 s				0.011 s			
χ^2, ‰	7	5	6	7	4	3	3	3

Lentelėje matyti, jog makroskopiniai parametrai (nesusiję su vidiniu sąveikaujančių sukinių porų pasisskirstymu, pavyzdžiui, R_{diff}) beveik nepriklauso nuo naudotos $P(b/2)$ formos, nors vizualiai vertinant yra matyti, jog spindulinis pasiskirstymas atkartoja kinetikas geriausiai.

Reikia pastebėti, jog norint apskaičiuoti tikrąjį $P(b/2)$ skirstinį, vertėtų taikyti kitokią apdorojimo strategiją. Jeigu makroskopiniai parametrai nepriklauso nuo kosinuso vidurkio, tai juos galima matematiškai išprastinti. Tuomet likęs kosinuso vidurkis taps ne kuo kitu, kaip $P(b/2)$ funkcijos *Fourier* vaizdu. Šitą apdorojimo kelią galima išreiškti taip:

$$P\left(\frac{b}{2}\right) \sim \left|\widehat{FT}^{-1}\frac{1-\lambda f_1 - I(t)/I_0 f_3}{(1-\lambda)f_2}\right| \qquad \text{(S.4)}$$

kur $f_1 = \exp(-R\,t)$, $f_2 = \exp(-1.5\,R\,t)$, ir $f_3 = \exp(-t/\,T_{1\rho})$. Dipolinės sąveikos konstanta su atstumu turi tokį sąryšį:

$$b_{jk} = -\frac{\mu_0}{4\pi}\frac{\gamma_j\gamma_k}{{r_{jk}}^3} \quad \text{(S.5)}$$

Vadinasi, po apdorojimo galima perskaičiuoti dipolinės sąveikos pasiskirstymą į sąveikaujančių sukinių porų atstumo pasiskirstymą. Apdorojimo rezultatas ir perskaičiavimas pavaizduoti 6 paveiksle.

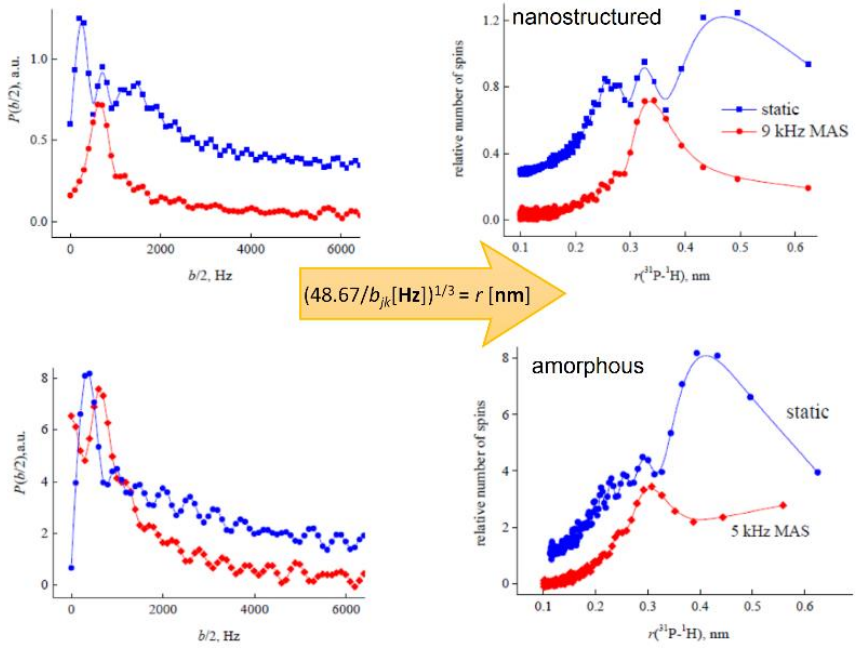

S.6 pav. Atbuline eiga apskaičiuotas $P(b/2)$ pasiskirstymas bei erdvinis sukinių aplink ^{31}P izotopus pasiskirstymas amorfiniame bei nano-struktūrizuotame kalcio hidroksiapatite.

Erdviniuose ^{1}H-^{31}P pasiskirstymuose yra matyti 3 maksimumai, iš kurių 0.21-0.25 nm yra tipinis P-OH atstumas aptinkamas įvairiuose fosfatiniuose kompozituose, nanodalelėse bei divandenilio fosfatuose[32,107,110]. Visgi kalcio hidroksiapatite vandenilis nėra fosfatinėje grupėje, tačiau jo galime rasti paviršiuje esančiose grupėse[113]. Dėl šios priežasties stebimas skirtumas yra esminis tarp amorfinio ir nano-struktūrizuoto apatito. Priešingai nei pirmasis, antrasis maksimumas yra žymus abiem atvejais, todėl gali būti siejamas su pagrindine ^{1}H-^{31}P sukinių pora kristalinėje gardelė. Magiškojo kampo sukimas nesuvidurkina šios, pagrindinės, sukinių poros, todėl galima teigti, jog MAS taikymas leidžia atsieti netvarkias bei tolimąsias sukinių poras, tokiu būdu sąveikaujančių porų skaičius (arba parametras λ) yra žymiai

apribojamas, todėl galima stebėti lokalius struktūrinius ypatumus kompleksinėse medžiagose.

Išvados

- Didelio taškų tankio kryžminės poliarizacijos matavimai atskleidė struktūrinius amorfinio bei nano-struktūrizuoto kalcio hidroksiapatito skirtumus sub-nano dydžių eilėse.
- Buvo pastebėta, jog tokie makroskopiniai parametrai kaip sukinių difuzijos sparta, klasterio dydis, relaksacijos sparta nuo pasirinktos bendrinės dipolinės sąveikos pasiskirstymo formos modeliuojant nepriklauso, nepaisant jog spindulinis pasiskirstymas atitiko rezultatus geriausiai. Ši savybė buvo panaudota apskaičiuoti tikrąjį pasiskirstymą bei nustatyta, jog spindulinis pasiskirstymo funkcija sumažina tolimosios tvarkos efektus.
- Tipiniai tarpbranduoliniai ^{1}H-^{31}P atstumai buvo nustatyti tiek amorfinio tiek nano-struktūrizuoto kalcio hidroksiapatito atvejais. Atstumo 0.26 nm nebuvimas amorfinio apatito atveju byloja apie pagrindinį dviejų medžiagų morfologinį skirtumą.

- Buvo pademonstruota, jog magiškojo kampo sukimas nutraukia tolimųjų adsorbuoto vandens sukinių bei netvarkiųjų paviršiaus grupių sąveiką. Vadinasi, MAS taikymas su kryžmine poliarizacija leidžia tirti lokalias sukinių poras ir taip sumažina sąveikaujančių sukinių klasterio dydį.

Kampinis vidurkinimas atliekant magikojo kampo sukimą

Reikia pridurti, jog pristatytas apdorojimo kelias turi vieną svarbų trūkumą. Dipolinė sąveika kietąjame kūne iš tiesų priklauso ne tik nuo atstumo.

$$b = -\frac{\mu_0}{4\pi}\frac{\gamma_j\gamma_k}{r_{jk}{}^3}\,\frac{3\cos^2\theta-1}{2} = b_{jk}\,\frac{3\cos^2\theta-1}{2} \qquad \text{(S.6)}$$

Kaip yra matyti iš išraiškos viršuje, ji priklauso tiek nuo atstumo tarp sąveikaujančių sukinių, tiek nuo kampo, kurį sukinių pora sudaro su išoriniu magnetiniu lauku.

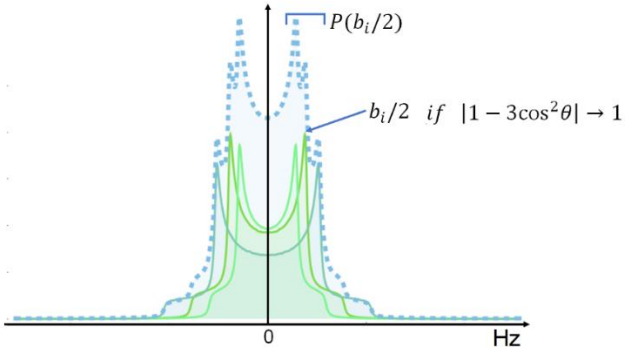

S.7 pav. Apskaičiuoti dipolinės sąveikos spektrai kelioms skirtingoms sukinių poroms. Skaičiavimai atlikti su atviros prieigos programa *SpinDynamica*[101].

Šio ryšio rezultatas yra toks, jog smulkių miltelių spektre susiformuoja vadinamas *Pake* skirstinys, vaizduojamas S.7 paveiksle. Vadinasi, prieš tai aptartas apdorojimo metodas galioja tik vienai konkrečiai orientacijai, o ne visam skirstiniui: tai gali lemti ne visiškai tiksliai apskaičiuotą erdvinį pasiskirstymą.

Taigi, vertėtų remtis CP modeliu, kuriame kampinis vidurkinimas yra įskaičiuotas bei naudoti modelinę medžiagą su žinomu erdviniu pasiskirstymu. Šiame darbe tokia medžiaga yra amonio divandenilio fosfatas (ADP), o I-I*-S modelis aprašantis magiškuoju kampu besisukančiuose milteliuose vykstančią CP dinamiką yra aprašomas tokia išraiška[109,114]:

$$I(t) = \frac{1}{2}\left[\mathrm{e}^{\frac{-t}{T_{1\rho}}} - \mathrm{e}^{-k_1 t} g(t)\right] + \left(\frac{\langle S\rangle_{qe}}{\omega_{0,\mathrm{I}}} - \frac{1}{2}\right)\left[\mathrm{e}^{\frac{-t}{T_{1\rho}}} - \mathrm{e}^{-k_2 t}\right] \quad \text{(S.7)}$$

čia S_{qe} kvazi-pusiausvyros būsenos poliarizacija, kurį gali būti nusakoma:

$$\langle S\rangle_{qe} = \frac{N}{N+1}\omega_{0,\mathrm{I}} \quad \text{(S.8)}$$

Konstantos k_1 ir k_2 yra ne kas kitas kaip R ir $1.5R$ išraiškose (S.2) ir (S.3) nusakančios sukinių difuzijos spartą. Taigi, vėl naudojant *Alemany* prielaidą galima perrašyti modeliai netvarkioms struktūroms:

$$I(t) = \left[\mathrm{e}^{\frac{-t}{T_{1\rho}}} - \mathrm{e}^{-k_1 t} \cdot \mathrm{e}^{\frac{-t^2}{2T_2^2}}\right] + \left(\frac{N-1}{N+1}\right)\left[\mathrm{e}^{\frac{-t}{T_{1\rho}}} - \mathrm{e}^{-k_2 t}\right] \quad \text{(S.9)}$$

Šis prielaida yra, žinoma, netinkama aprašyti CP kinetikas ADP atveju kaip yra matyti iš S.8 paveikslo, tačiau tai leidžia apskaičiuoti reikiamus parametrus, reikalingus atbuline eiga perskaičiuoti vyraujančias osciliacijas (10 pav.).

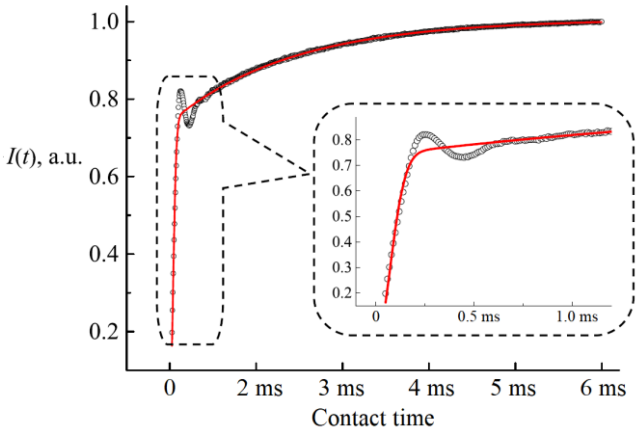

S.8 pav. $^{1}H \rightarrow {}^{31}P$ CP-MAS kinetika amonio divandenilio fosfate (MAS dažnis – 7 kHz, *Hartman-Hahn* sąlyga $n = 1$). Parametrai apskaičiuoti naudojantis (S.9): k_1=539±7 s^{-1}, (N-1)/(N+1) = 0.362±0.002, T_2 = 7.65±0.05, $T_{1\rho} \rightarrow \infty$, $k_1 = 3/2\ k_2$ ryšys buvo fiksuotas.

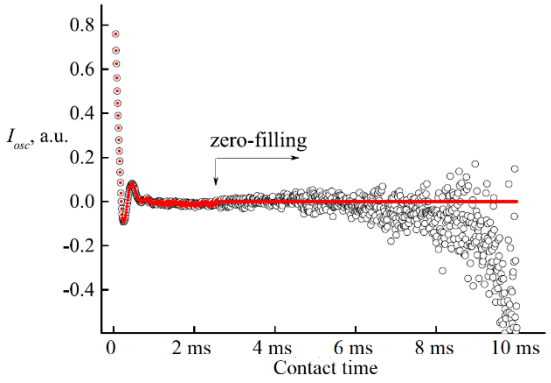

S.9 pav. Kryžminės poliarizacijos amonio divandenilio fosfate koherentinė dalis atbulai perskaičiuota naudojant S.8 paveiksle pateiktus parametrus. Triukšmingi taškai buvo pakeisti nuliais nuo 3 ms.

Šios osciliacijos yra koherentinė funcija $g(t)$, kuri matematiškai yra kampinis dipolinės sąveikos vidurkis priklausantis nuo *Hartmann-Hahn* sąlygos. Šiame darbe visos (apart statinio bandinio atveju) kinetikos buvo matuojamos galiojan $n = 1$ sąlygai, kuriai atitinkama $g(t)$ funkcija yra:

$$g_{\pm 1}(t) = 1/2 \int_0^{\pi} \cos\left(\frac{\pi b_{jk} t}{\sqrt{2}} \sin 2\theta\right) \sin(\theta)\, \mathrm{d}\theta = J_0\left(\frac{\pi b_{jk} t}{\sqrt{2}}\right) + 2\sum_{k=1}^{\infty}\left[\frac{1}{1-4(2k)^2} J_{2k}\left(\frac{\pi b_{jk} t}{\sqrt{2}}\right)\right] \quad \text{(S.10)}$$

Visi galimi funkcijos variantai yra pateikti literatūroje[114]. Akivaizdu, jog pastaroji išraiška yra per sudėtinga paprastam jos taikymui, todėl verta priimti kelias prielaidas, kurių esmė pavaizduota S.10 paveiksle.

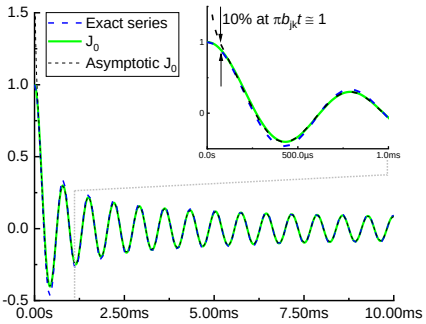

S.10 pav. Pilna (S.10) funkcija įskaičiuojant pilną *Bessel* eilutę, tik pirmasis narys bei asimptotinis $J_0(x)$ artinys, kai $x = \frac{\pi b_{jk} t}{\sqrt{2}}$ ir $b_{jk} = 4000$ Hz.

Pirmiausia, *Bessel* fukcijų eilutėje galima atmesti aukštesnių eilių narius, kadangi jokio žymaus skirtumo nematyti – taip lieka tik J_0 narys, kurio asimptotinė forma yra hiperbolinio kosinuso funkcija. Deja, asimptotinė forma nesutampa su tikrąja eilute ties $g(t)$ pradžia, tačiau ši pradžia normaliomis eksperimentinėmis sąlygomis tenusako kelis pirmus taškus. Nepaisant to, šios prielaidos ženkliai supaprastina išraišką, kuomet koherentines CP osciliacijas (10 pav.) galima išreikšti taip:

$$I_{osc}(t) = \int_0^{\infty} \mathrm{d}b_{jk}\, P(b_{jk}) J_0\left(\frac{\pi b_{jk} t}{\sqrt{2}}\right) = \int_0^{\infty} \mathrm{d}x\, \frac{P(b_{jk})}{b_{jk}} b_{jk} J_0\left(\frac{\pi b_{jk} t}{\sqrt{2}}\right) \quad \text{(S.11)}$$

Dešinioji išraiškos pusė yra perrašyta taip, jog primintų *Hankel* transformaciją. Tuomet pasinaudojant jos savybę galima pademonstruoti, jog tikrasis erdvinis sąveikaujančių sukinių pasiskirstymas yra:

$$P\left(\frac{\frac{b_{jk}}{\sqrt{2}}}{2}\right) \sim \sqrt{b_{jk}} \int_0^{\infty} [I_{osc}(t)\sqrt{t}] \cos\left(2\pi \frac{\frac{b_{jk}}{\sqrt{2}} t}{2}\right) \mathrm{d}t \rightarrow$$

$$\sqrt{b_{jk}}\, Re\{\widehat{FT}[I_{osc}(t)\sqrt{t}]\} \qquad \text{(S.12)}$$

Vadinasi, visiškai tik nuo atstumo priklausantį erdvini pasiskirstymą galima apskaičiuoti atliekant *Fourier* transformaciją pradinėms kryžminės-poliarizacijos osciliacijoms su papildomu faktoriumi. Galutinis šio apdorojimo rezultatas amonio divandenilio fostato atveju pateiktas S.11 paveiksle bei 2 lentelėje.

S2 lentelė. Atstumų tarp fosforo ir jų supančių vandenilių pasiskirstymo maksimumai amonio divandenilio fosfate bei kitais kristalografiniais metodais apskaičiuotos vertės. Matavimo vienetai – nanometrai.

Apdorojimo būdas	1 atstumas	2 atstumas	3 atstumas
7 kHz MAS, r-vidurkis*	0.239	0.376	0.507
10 kHz MAS, r-vidurkis*	0.237	0.376	0.507
7 kHz MAS, pilnas vid.	0.234	0.364	0.476
10 kHz MAS, pilnas vid.	0.236	0.357	0.479
Neutronų difrakcija [115,116]	0.219-0.22	0.330-0.344	0.476-0.444
Rentgeno difrakcija [31,32,116]	0.235-0.244	0.329-0.335	0.430-0.441

*pristatytas praeitame skyriuje

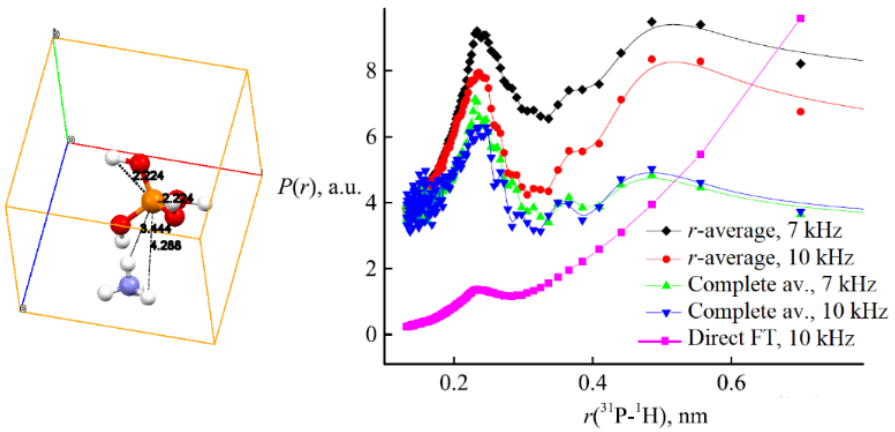

S.11 pav.Kairėje – kristalinė ADP gardelė bei pagrindiniai P-H atstumai, dešinėje – skirtingais CP kinetikų apdorojimo keliais apskaičiuotas erdvinis sąveikaujančių P-H porų pasiskirstymas.

Taigi, yra matyti, jog ADP kristale yra trys skirtingos P-H porų. Pagrindinė (trumpiausioji) pora pagal kristalografinius duomenis yra apskaičiuota tiksliausiai ir ją galima aptikti taikant tiesioginę *Fourier* transformaciją CP kinetinėms kreivėms. Kita vertus, kitų charakteringų atstumų verčių tikslumas

priklauso nuo pasirinkto apdorojimo būdo. Kaip ir buvo tikimąsi, apdorojimas, kuriame buvo įskaičiuotas pilnas kampinis vidurkinimas, buvo tiksliausias. Tą patvirtina neblogas sutapimas su difrakcinių metodų rezultatais. Todėl, galima daryti išvadą, jog taikomas apdorojimas yra pakankamai tikslus tirti kristalinių gardelių struktūrą.

Išvados

- Erdvinis bei kampinis vidurkinimai buvo atlikti pasinaudojus *Hankel-Fourier* transformacija, kuri leido apskaičiuoti tik nuo atstumo priklausantį dipolinės sąveikos pasiskirstymą.
- Gautos tarp-branduolinių atstumų amonio divandenilio fosfate vertės puikiai dera su kitais kristalografiniais duomenimis. Vadinasi, naudotas metodas yra pakankamai tikslus, jog būtų naudojamas išgauti papildomos kristalografinės informacijos.

2.4 Kryžminė poliarizacija organinėse medžiagose

Kryžminė poliarizacija ir joje vykstantis terminis nusistovėjimas paprastai laikomas procesu vykstantis atviroje sukinių sistemoje. Nepaisant to, šios prielaidos tikslumas gali priklausyti nuo sąveikaujančių sukinių. Iš tiesų, žymus skirtumas yra paprastai stebimas, pavyzdžiui, tarp stipriai ir silpnai surištų ^{13}C-^{1}H porų[117]. Dėl to, organinėse medžiagose galima aptikti įvairių skirtingų sistemų, kuriose ši prielaida nebegalioja. Deja, tai reikalauja patikslinti CP modelius, atsižvelgiant į kiekvieną atskirą atvejį.

Stipriai surištos sukinių sistemos, pavyzdžiui, CH_2 grupė paprastai pasižymi stipria dipoline sąveika. Glicino atveju kryžminės poliarizacijos kinetinėse kreivėse koherentinės osciliacijos yra aiškiai matomos ir išskiriamos, jeigu magiškojo kampo sukimo dažnis yra pakankamai didelis (S.12 pav.).

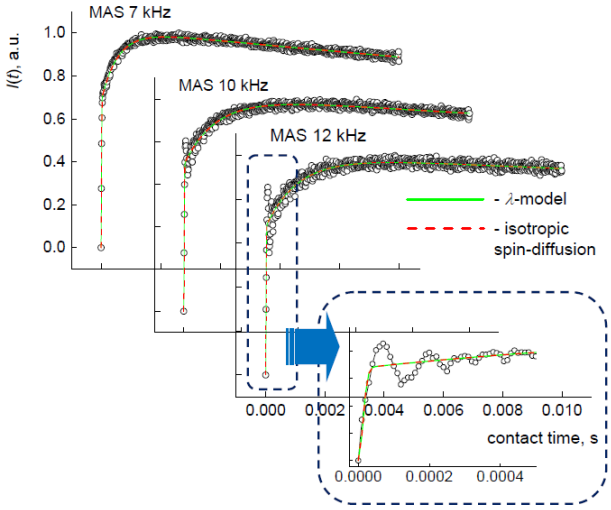

S.12 pav. Metileno $^{1}H \rightarrow ^{13}C$ CP-MAS kinetinės kreivės glicino milteliuose keičiant MAS dažnį. Žalia linija yra λ-modelis aprašomas (S.3) funkcija, o raudona – aproksimavimas (S.9) išraiška, laikančia sukiniu difuziją izotropine.

Praeitame skyriuje aptartas I-I*-S modelis yra dar kitaip vadinamas izoliuotos sukinių poros modeliu, kuriame sukinių difuzija yra laikytina izotropinė. Ji laikoma izotropinė, kol galioja sąryšis $k_1=3/2\ k_2$. Sukinių difuzija paprastai yra nulemta dipolinės sąveikos tarp tokių pačių branduolių (šiuo atveju ^{1}H-^{1}H), vadinasi, trumpesni atstumai lemtų greitesnę sukinių difuziją. CP-MAS matavimai buvo atlikti serijai kitų aminorūgščių, kuriose apskaičiuota sukinių difuzijos sparta leido surišti su jų kristaline struktūra. Iš tiesų, sukinių difuzijos sparta visose aminorūgštyse, išskyrus valiną, priklauso nuo vandenilio atomų tankio (S.13 pav.). Ši išimtis gali būti siejama su dideliu kiekių mobilių CH_3 grupių, kurios lygiai taip pat gali suprastinti dipolinę sąveiką ir taip prailginti sukinių difuzijos laiką.

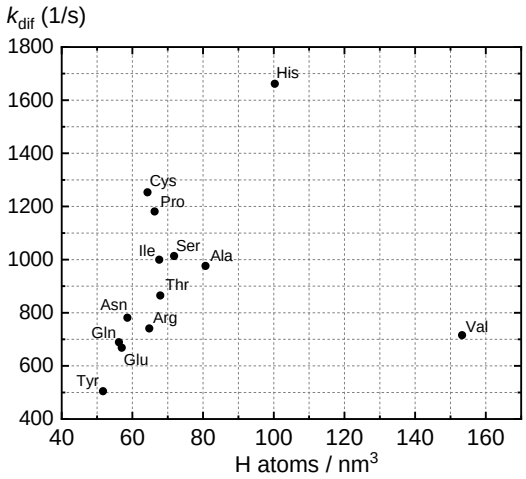

S.13 pav. Sukinių difuzijos spartos priklausomybė nuo vandenilio atomų tankio amino rūgščių kristalinėse gardelėse.

Vadinasi, izotropinės sukinių difuzijos modelis gerai aprašo didžiąją dalį grupių (žr. S.12 pav.), tačiau grupių mobilumas gali nulemti visuminę CP kinetikos formą. Mobilumo įtaką galima pastebėti net ir glicino atveju. Iš eksperimentinių duomenų matyti, jog yra svarbu ne tik atsižvelgti į MAS dažnį, tačiau ir į vandens kiekį bandinyje. Pastarojo buvimas, kaip yra matyti iš kryžminės poliarizacijos osciliacijų dažnio sumažina dipolinės sąveikos stiprį. Tai galima paaiškinti atsirandančiais papildomais laisvės laipsniais cheminėse grupėse, kurios šiek tiek suprastina (S.6) priklausomybę ir taip pat stebimą dažnį.

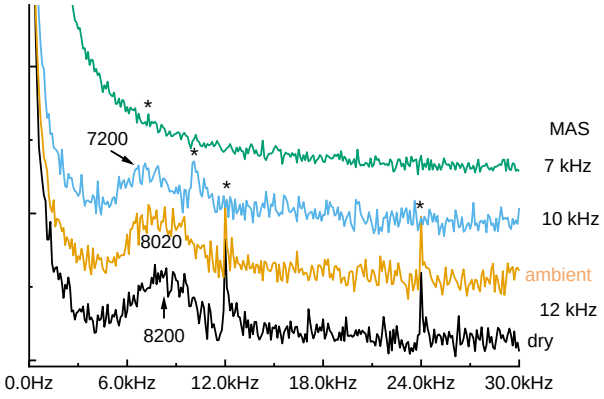

4.24 pav. CP osciliacijų (matomų S.12 pav.) dažnis apskaičiuotas naudojant *Fourier* transformaciją.

Verta paminėti, jog metilo grupėse paprastai vyksta persiorientavimai aplink C_3 simetrijos ašį. Tai galima laikyti sukimusi skėtiniu kampu (70,5°), kurį įstačius į (S.6) gaunama, jog tikroji dipolinės sąveikos konstanta yra padauginama iš 0,333. Šis pastebėjimas leidžia naudoti metilo grupes kaip vidinį standartą, kuris pašalintų papildomus efektus, pavyzdžiui, dėl nepakankamo bandinio sukimosi dažnio. Deja, taip pat tai reikštų, jog stebimas CP osciliacijų dažnis bus itin mažas, o tai iškelia sunkumus juos apskaičiuojant.

Žymiai geresnė dipolinės sąveikos dažnio raiška pasiekiama naudojant jau pristatytą CP kinetikų apdorojimą (žr. į S.9 pav.), tačiau ji gali būti nepakankama. Taip pat buvo pademonstruota 11 paveiksle, jog triukšmo šalinimas gali būti atliekas pildymu nuliais. Visgi, tokiu būdu raiška nepadidėja. Vietoje to, galima atlikti spektroskopijoje gerai žinomą apodizavimo procedūrą (S.14 pav.).

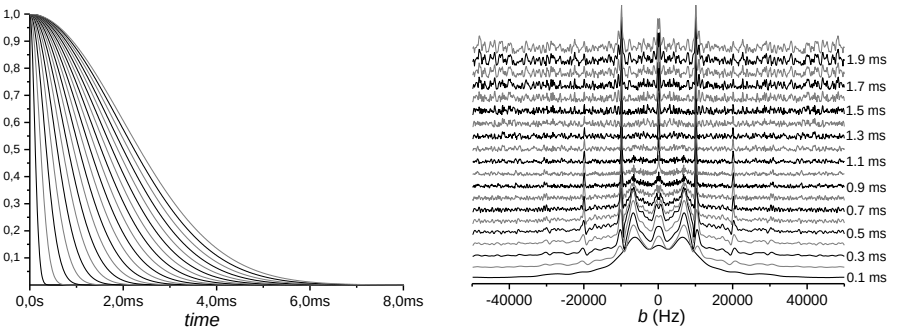

S.14 pav. Keičiamas apodizavimo funkcijos plotis (kairėje) bei jos taikymo efektas dipolinės sąveikos spektre. Pavyzdyje – CP kinetikos alanino H-C_α poroje duomenys.

Deja, tai reikalauja naudotojo kontrolės, kadangi skirtingi apodizavimo pločiai daro įtaką duomenims skirtingai. Nepaisant to, naudojant šiuolaikinius programavimo metodus, ši procedūra neprailgina apdorojimo spartos.

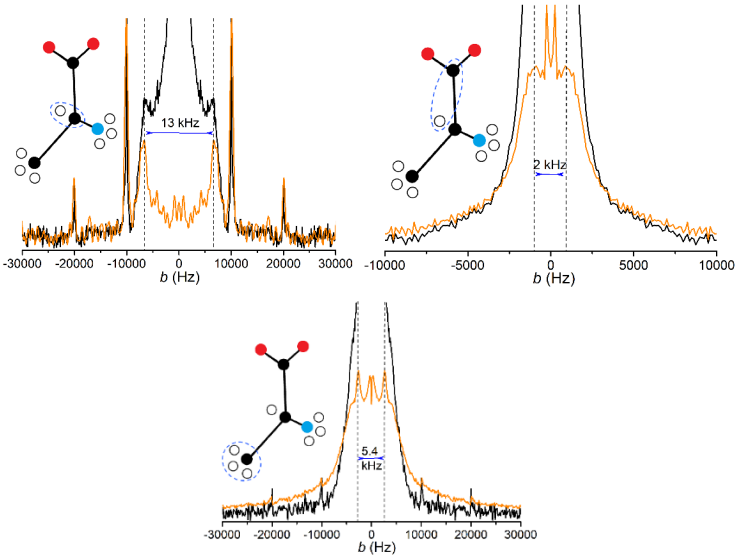

S.15 pav. Rezultatų palyginimas naudojant tiesioginę *Fourier* transformaciją (juoda linija) bei taikant apodizavimo procedūrą. Pavyzdys – alanino cheminės grupės ir sukinių poros.

Pateiktame pavyzdyje matyti, kad taikant apodizavimo procedūrą pagerėja ne tik dipolinės sąveikos spektro raiška, bet atsiranda galimybė išskirti net ir silpną dipolinę sąveiką. Matomas metilo grupės dipolinės sąveikos spektras atsikartoja visoms aminorūgštims (žiūrėti disertacijoje), vadinasi, metilo grupės gali būti naudojamos kaip apdorojimo standartas.

Kadangi šis būdas leidžia efektyviai išskirti ir aptikti silpnas dipolines sąveikas, jį galima taikyti lanksčių struktūrų tyrimuose, kuriuose pasireiškia cheminių grupių mobilumas. Tokia modelinė sistema šiame darbe yra poli-(hidroksietilmetakrilatas) (pHEMA). Jo dipolinės sąveikos spektrai pavaizduoti S.16 paveiksle.

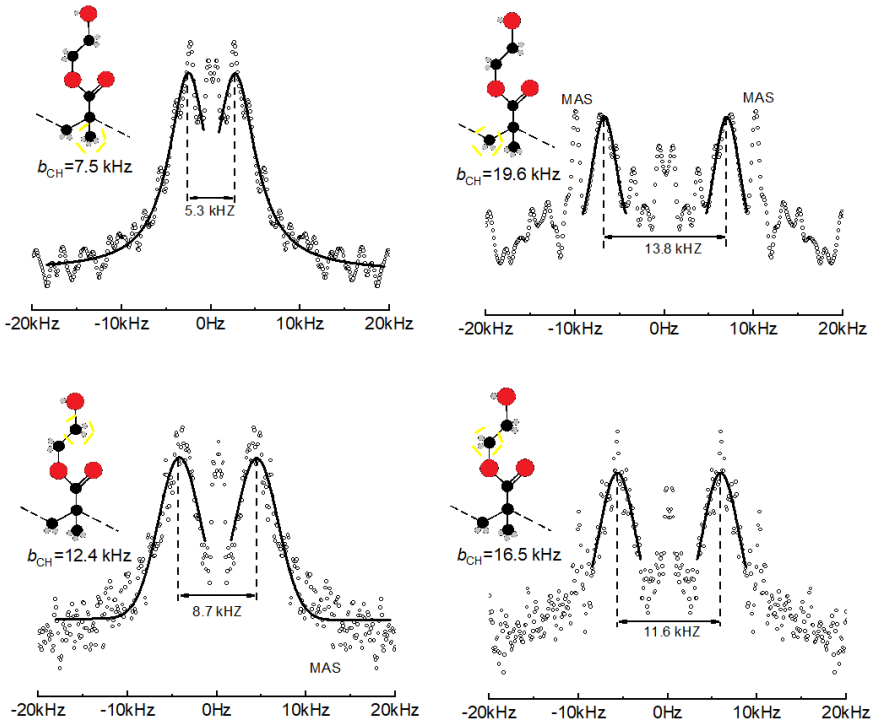

S.16 pav. ^{1}H-^{13}C dipolinės sąveikos spektras PHEMA polimero cheminėse grupėse apskaičiuotas panaudojus apodizavimo metodą. Dipolinės sąveikos konstantos apskaičiuotos pagal suskilimo dydį.

Dipolinės sąveikos vienguboje CH jungtyje stipris paprastai yra pastovus ir lygus 23 kHz, tuo tarpu pastarajame polimere vertės yra gerokai mažesnės. Metilo grupės vertė jau buvo aptarta ir turi būti lygi apie 7.7 kHz, vadinasi galima įskaityti pataisos faktorių į tolimesnius skaičiavimus, kuris yra lygus 1.02. Nepaisant to, rotacijos kitose cheminėse grupėse nėra galimos, tačiau mobilumas gali atsirasti ir kitokiais būdais. Pavyzdžiui, esant nemažoms virpesių amplitudėms arba atsirandant papildomiems laisvės laipsniams, CH jungtys gali šiek tiek chaotiškai persiorientuoti. Todėl, yra priimtas susitarimas santykį tarp išmatuojamos ir tikrosios dipolinės sąveikos laikyti orientaciniu tvarkos parametru. Jis taip pat taikomas tiriant netgi didelių molekulių, tokių kaip baltymai ar peptidai, lokaliąją tvarką[119]. Šioje molekulėje taip pat stebima logiška tvarkos parametro seka, kuomet pagrindinėje polimero grandinėje tvarkos parametras yra žymiai didesnis negu šoninėse grandinėse, kuriose tikėtinas padidėjęs laisvės laipsnis.

Praeituose pavyzdžiuose sąveikaujantys sukiniai buvo nutolę per CH jungties ilgį ir todėl pakankamai stipriai surišti, tačiau karboksilo (-COO^-) grupės atveju vandenilio atomai yra per kelias jungtis nuo anglies atomo, vadinasi, dipolinė sąveika irgi nebus stipri. Verta sugrįžti prie paprasto glicino atvejo ir jame esančios karboksilo grupės. Kryžminė poliarizacija iš vandenilio į anglis yra pavaizduota apačioje.

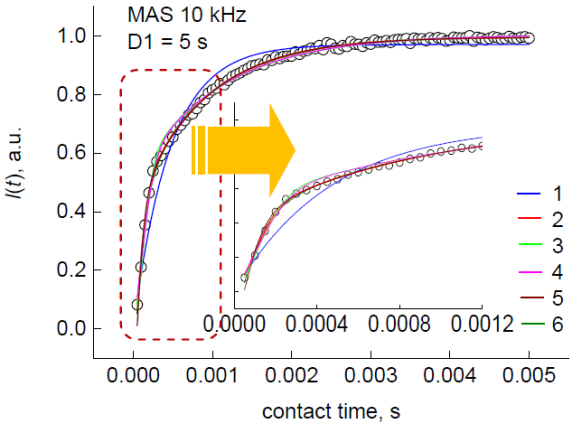

S.17 pav. $^1H \rightarrow {}^{13}C$ CP-MAS kinetinė kreivė glicino COO^- grupėje. Kinetika aproksimuota skirtingais modeliais (modeliai ir rezultatai pateikti 2 lentelėje).

Literatūroje buvo pademonstruota: jeigu (I-I) sąveika I-I*-S modelyje yra lygi arba stipresnė negu (I*-S) sąveika, kryžminė poliarizacija tampa eksponentine priklausomybe[132]:

$$\langle S_z\rangle(t) = \langle S\rangle_{qe}(1 - e^{-2W_{IS}t}) \qquad \text{(S.13)}$$

čia W_{IS} yra efektyvioji dipolinė sąveika tarp sąveikaujančių sukinių. Deja, tai gana prastai aprašo pastarąją kinetiką, todėl geriau yra atsispirti nuo modelio gerai aprašančio stipriai surištų sukinių CP kinetikas. Taip pat galima papildomai įskaityti papildomą procesą I-I sukinių posistemėje, t.y. poliarizacijos nusistovėjimą kvazi-pusiausvyros būsenoje[133]:

$$\langle S\rangle_{qe} = \frac{N}{N+1}\omega_{0I}(1 - \exp(-k_T\, t)^{\alpha}) \qquad \text{(S.14)}$$

kur k_T yra terminio nusistovėjimo konstanta bei α rodiklis leidžiantis nusistovėjimui nebūtinai būti *Debye* tipo procesui. Laikant, jog dipolinė sąveika silpna ir dipolinės sąveikos pasiskirstymas yra gana siauras, tuomet

T_2 išraiškoje (S.6) bus lygi 0, ir tada $g(t) \rightarrow 1$. Tai palengvina modeliavimo užduotį eliminuojant papildomą parametrą.

S3 lentelė. Modeliai naudoti aproksimuojant $^1H \rightarrow ^{13}C$ CP-MAS kinetikas glicino COO^- grupėje ir apskaičiuoti parametrai. $T_{1\rho} \rightarrow \infty$ prielaida buvo taikant dėl nestebimos relaksacijos.

MAS dažnis	**7 kHz**	**10 kHz**	**12 kHz**
1 mod.	Viena eksponentė (S.13); $T_{IS} = 1/(2W_{IS})$)		
T_{IS}, µs	540 ± 10	460 ± 10	*
R^2/χ^2	0.984/6.2·10^{-4}	0.965/1·10^{-3}	
2 mod.	λ-modelis (S.6)		
λ	0.712 ± 0.007	0.598 ± 0.006	0.43 ± 0.01
T_{dif}, µs	810 ± 10	860 ± 10	1180 ± 20
T_2, µs	140 ± 30	120 ± 20	130 ± 3
R^2/χ^2	0.999/3·10^{-5}	0.998/4·10^{-5}	0.9997/5·10^{-5}
3 mod.	Izotropinė sukinių difuzija (S.9), bei $k_1/k_2 = 3/2$		
N	∞	∞	*
k_2, s^{-1}	890 ± 25	950 ± 20	
T_2, µs	220 ± 70	140 ± 30	
R^2/χ^2	0.991/3.3·10^{-4}	0.995/1.5·10^{-4}	
4 mod.	Anizotropinė sukinių difuzija (S.9) kai k_1 ir k_2 laisvai varijuoja; Papildoma $1/T_2 \rightarrow 0$ prielaida, tada $g(t) \rightarrow 1$		
	$k_1 > k_2$		
N	∞	∞	*

k_1, s^{-1}	4200 ± 200	2600 ± 400	
k_2, s^{-1}	980 ± 20	950 ± 20	
R^2/χ^2	0.997/$1.1\cdot10^{-4}$	0.995/$1.4\cdot10^{-4}$	
	$k_1 << k_2$		
N	4.0 ± 0.7	15 ± 11	*
k_1, s^{-1}	1130 ± 30	1070 ± 50	
k_2, s^{-1}	5100 ± 300	6200 ± 500	
R^2/χ^2	0.998/$7\cdot10^{-5}$	0.995/$1.6\cdot10^{-4}$	
5 mod.	Terminis nusistovėjimas ((S.9) + (S.14) ir α = 1); Papildomos prielaidos: $k_T = k_2$, g(t) → 1		
N	1.8 ± 0.1	5.0 ± 0.5	*
k_1, s^{-1}	1360 ± 30	1160 ± 25	
k_2, s^{-1}	27300 ± 1500	16500 ± 500	
R^2/χ^2	0.995/$1.9\cdot10^{-4}$	0.997/$9\cdot10^{-5}$	
6 mod.	Terminis nusistovėjimas ((S.9) + (S.14) ir α laisvai varijuojamas); Papildomos prielaidos: $k_T = k_2$, g(t) → 1		
N	2.44 ± 0.2	7.3 ± 1.5	*
k_1, s^{-1}	1230 ± 20	1110 ± 30	
k_2, s^{-1}	29800 ± 1300	18000 ± 700	
α	0.7 (fixed)	0.73 ± 0.03	
R^2/χ^2	0.984/$6.27\cdot10^{-4}$	0.998/$6\cdot10^{-5}$	

*uždelsimo laikas reikalingas pasiekti stabilią kinetą buvo per ilgas išmatuoti daug taškų.

Dėl paprastumo, galima sumažinti laisvų parametrų skaičių dar vienu. Dar visai neseniai buvo pademonstruota, jog į skaičiavimus turėtų būti įtrauktas kiek tikslesnis sukinių difuzijos superopatorius[134]:

$$\hat{\Gamma}(\rho) = R_{dp}\left[\hat{I}_z,\left[\hat{I}_z,\rho\right]\right] + R_{df}\left\{\left[\hat{I}_x,\left[\hat{I}_x,\rho\right]\right] + \left[\hat{I}_y,\left[\hat{I}_y,\rho\right]\right]\right\} \quad \text{(S.15)}$$

Čia sukinių difuzijos spartą nusakantys skirtingi parametrai: R_{dp} – spektrinė difuzijos sparta, bei R_{df} yra erdvinės difuzijos sparta lygi parametrui k_2 išraiškoje (S.6). Parametras k_1 tokiu atveju yra $k_1 = R_{df} + R_{dp}/2$. Jeigu naujieji dėmenys yra lygus (izotropiniu atveju), bus grįžtama prie $k_1 = 3/2k_2$ atvejo. Kadangi erdvinė difuzija būtent ir vyksta I-I posistemėje, galima laikyti, jog terminis nusistovėjimas bus nulemtas jos, o tada konstanta $k_T = R_{df} = k_2$.

Lentelėje svarbu atkreipti dėmesį į modelio atitikimą R^2, kuris geriausiai atitinka λ-modelio atveju, tačiau parametras $\lambda > 0.5$ ($\lambda=1/(N-1)$) yra logiškai neįmanomas. Kitas aproksimavimo pagerėjimas buvo pastebėtas, kuomet buvo leidžiamas anizotropinės sukinių difuzijos atvejis. Vadinasi, spektrinė bei erdvinė sukinių difuzijos yra gerokai skirtingose laikiniuose masteliuose. Nepaisant to, geriausias rezultatas buvo pasiektas įtraukiant terminį ne *Debye* tipo nusistovėjimą I-I sukinių posistemėje. Rodiklis išraiškoje (S.14) yra surištas su fraktaline dimensija $D_p=3\alpha$, tačiau toks teiginys reikalauja patikrinimo serijoje bandinių[133].

Visoje disertacijoje yra nemaža imtis bandinių, kurie buvo išdėstyti į logišką tvarką. Pradžioje minėtas kalcio hidroksiapatitas pasižymi įdomia savybe – protonai kristalinėje gardelė sudaro linijinį kanalą. Tuomet, modeliavimas turėtų atspindėti žemo fraktališkumo struktūrą. Kita, specialiai parinkta, medžiaga yra polimeras – poli-(vinilfosfono rūgštis), kuriame vandenilio atomai taip pat yra išsidėstę į vieną liniją. Modeliavimo rezultatų lentelė yra pateikta disertacijoje, tačiau rezultatus galima pavaizduoti 4.41 iliustracijoje.

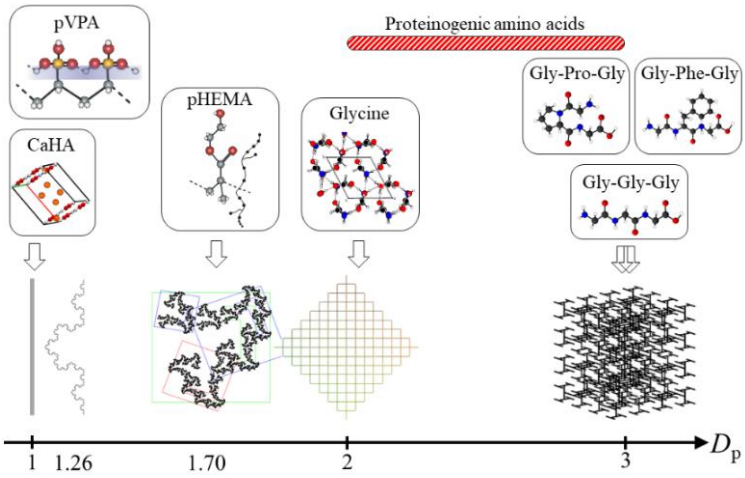

S.18 pav. Diagrama, apibendrinanti fraktalines dimensijas tirtuose bandiniuose. Fraktalinės dimensijos buvo apskaičiuotos naudojant 6 modelį S2 lentelėje. Apatinėje eilė - fraktalinių struktūrų pavyzdžiai.

Matyti, jog minėtieji bandiniai iš tiesų pasižymi žemu fraktališkumu, kas leidžia atmesti atsitiktinumo atvejį. Toliau sekoje yra matyti žinomas hidrogelis pHEMA polimeras, kuriame vandeniliniai ryšiai dalinai sujungia šonines grandines, todėl fraktalinė dimensija yra kiek didesnė. Paveiksle taip pat pavaizduota, jog aminorūgščių kristalinė struktūra, ypač nedidelių molekulių atvejų, taip pat gali įgyti ne pilnai tūrinį protonų išsidėstymą, kuris pasiekiamas didesnių molekulių kaip peptidai, dariniuose. Šis rezultatas leidžia teigti, jog terminio nusistovėjimo dinamika atkartoja struktūrų fraktališkumą.

Iš šių rezultatų galima daryti išvadą, jog CP-MAS metodas gali būti taikomas ne tik tirti struktūrinius parametrus kaip atstumas, tačiau gali aprašyti dinaminius procesus bei suteikti žinių apie struktūros fraktalines savybes. Vadinasi, taikomas metodas ir jo analizės būdas atskleidžia daugialypės informacijos apie tiriamas medžiagas bei gali būti pilnai taikomas nagrinėjant funkcines medžiagas.

- Dipolinės sąveikos spektro signalo ir triukšmo santykis buvo itin sustiprintas panaudojus papildomą apodizavimo procedūrą duomenų apdorojimo metu.
- Gretai besisukančios metilo grupės ir šios dinamikos nulemta dipolinė sąveika buvo panaudota kaip vidinis standartas nusakantis apodizacijos kokybę.
- Didelė dipolinės sąveikos spektrų raiška leido stebėti lokalųjį tvarkos parametrą pereinant nuo standžių amino rūgščių struktūrų prie lankstesnių peptidų bei polimerų. Tai suteikia kryžminės-poliarizacijos matavimams pranašumo lyginant su metodais, kurie suteikia tik vienalypę informaciją.
- Sukinių difuzijos spartos priklausomybė nuo sąveikaujančių sukinių tankio buvo stebėta pirmą kartą.
- Nustatyta, jog stipriai surištų sukinių CP dinamiką geriausiai aprašo I-I*-S modelis, kai cheminė grupėje vyrauja stipri dipolinė sąveika.
- Anizotropinė sukinių difuzija yra tinkamas artėjimas nusakantis kryžminę-poliarizaciją silpnai surištų sukinių, tokių kaip COO^- grupė, atveju.
- Terminio nusistovėjimo paplitusių sukinių posistemėje įskaičiavimas atvejo, kai I-S sąveika yra gerokai silpnesnė už I-I sąveikas, modeliavime lėmė geriausią atitikimą. Tai suteikė galimybę tirti terminį nustovėjimą, kuomet ištemptos eksponentės įskaičiavimas iškėlė ne-Debajaus proceso galimybę.
- Fraktalinė dimensija buvo sustatyta serijai bandinių pasinaudojus ne-Debajaus proceso prielaida. Apskaičiuotos fraktalinės dimensijos gerai atitiko tikėtiną bandinių struktūrą. Vadinasi, tai atveria naują kryžminės-poliarizacijos metodikos taikymą tiriant fraktalines medžiagų struktūras.

S3. DISERTACIJOS IŠVADOS

1. BMR ^{1}H bei ^{31}P tyrimai naudojant magiškojo kampo sukimą atskleidžia detalią informaciją susijusią su amorfinių ar nano-struktūrizuotų medžiagų sandara, sąranga bei dinaminių vyksmų sparta.

2. Makroskopiniai parametrai apskaičiuojami modeliuojant kryžminės-poliarizacijos kinetikas nepriklauso nuo bendrinės dipolinės sąveikos pasiskirstymo funkcijos. Tuo pasinaudojus galima atbuline tvarka apskaičiuoti tikrąjį dipolinės sąveikos pasiskirstymą.

3. Tinkamas būdas apdoroti pradines koherentines CP osciliacijas buvo išplėtotas perėjus iš *Fourier-Bessel* į įprastinę *Fourier* transformaciją pasitelkus keliomis prielaidomis. Šis metodas leidžia apskaičiuoti tik nuo tarpbranduolinio atstumo priklausantį sąveikaujančių sukinių porų pasiskirstymą, kurio tikslumas yra palyginimas su ND ir XRD technikomis.

4. Dipolinės sąveikos pasiskirstymo (ypač silpnai surištų sukinių) signalo ir triukšmo santykis gali būti reikšmingai sustiprint pritaikant interaktyvų apodizavimo metodą CP kinetikų apdorojimo metu. Tai atveria galimybes tirti lokalųjį tvarkos parametrą įvairiose cheminėse grupėse.

5. Kryžminės poliarizacijos tyrimai atskleidė ženklų skirtumą tarp CP vykstančios stipriai ir silpnai surištų sukinių porų. Jeigu I-I*-S modelis gerai aprašo stipriai surištas sukinių poras, tokios papildomos prielaidos kaip anizotropinė sukinių difuzija bei terminis nusistovėjimas paplitusių sukinių posistemėje, turi būti įtraukos silpnai sąveikaujančių sukinių atveju. Labai tikslus fraktalinių struktūrų atitikimas su terminio nusistovėjimo analize leidžia teigti, jog CP kinetikos tarp tolimųjų (silpnai surištųjų) sukinių porų gali atkartoti fraktalinę medžiagos struktūrą.

TRUMPOS ŽINIOS APIE DISERTANTĄ

Vardas, Pavardė: Laurynas Dagys
Gimimo data: 1992-12-15
Gimimo vieta: Vilnius
Kontaktai:
mob.tel.: +37065451856
el. paštas: laurynas.dagys @ff.vu.lt

Išsilavinimas:

2015-2017 fizikos magistras, Vilniaus universitetas
2011-2015 fizikos bakalauras, Vilniaus universitetas

Darbinė veikla:

2014-2016 laborantas, Vilniaus universitetas
2016-2017 lektorius, Vilniaus universitetas
2018- ITN bendradarbis, *University of Southampton*

Visuomeninė veikla:

2014-2015 Valdybos narys, Studentų mokslinė draugija (Fizikos fakultetas)
2011-2015 Narys, Studentų mokslinė draugija (Fizikos fakultetas)

Dalyvavimas projektuose:

2014 „Studentų mokslinės veiklos skatinimas.“ (Registracijos Nr. SMT2014RA027)
2018 Lietuvos-Ukrainos dvišalio bendradarbiavimo mokslo ir technologijų srityje programa (TAP-LU-15-017)
2018 „Modern trends in solid-state NMR and spin dynamics: towards non-destructive polarizing agents“ (HYPERSPIN)

Apdovanojimai, stipendijos:

2016-2017 Vardinė prezidento A. Stulginskio stipendija už mokslo pasiekimus
2015-2017 Skatinamoji stipendija (magistrantūros studijos)
2014-2015 Stipendija už studentų mokslinius tyrimus

Mokyklos, stažuotės:

2018 Vasaros mokykla „BMR teorija, hiperpoliarizacija“, Vokietija
2018 Vasaros mokykla „AMPERE vasaros mokykla“, Lenkija
2018 Stažuotė Darmštado techinkos universitete, Vokietija
2018 Stažuotė Southampton‘o universitete, Jungtinė Karalystė

ACKNOWLEDGEMENTS

I would mostly like to acknowledge my parents Regina and Rimantas, my brothers Marius, Jonas, my lovely fiancée Eglė and rest of my family for the patience and unprecedented support throughout the study years.

I am also most grateful for the excellent supervision of prof. Vytautas Balevičius who has gave me incredible freedom and opportunities to explore the complex world of NMR. This also would not had been possible without caring support of dr. Vytautas Klimavičius who was first to teach me experimental and technical subtleties.

I feel very enchanted by the number of co-authors that have contributed to this work, especially dr. Kęstutis Aidas, prof. Aivaras Kareiva, dr. Valdemaras Aleksa, Jonas Kausteklis, dr. Torsten Gutmann, prof. Gerd Buntkowsky and others. I thank for collaborators prof. Ričardas Makuška, Vaidas Klimkevičius and dr. Martin Brodrecht who have carried out the chemical synthesis for the used compounds significantly improving this work.

Very warm appreciation goes to prof. Gediminas Niaura who have shared his samples as well as scientific views which enriched my personal perspectives on professional life. The same goes to all Institute of Chemical Physics members for creating the homely atmosphere during work as well as special thanks to PhD students Martynas, Rasa, Dovilė, Kristina for they have shared the adventure of being a PhD student.

I want to express my gratitude towards prof. Janez Plavec for warm welcome at Slovenian NMR centre during my master studies and also prof. Gerd Buntkowsky for allowing me to perform experiments at TU-Darmstadt last year. Finally, I am honoured to be a part of prof. Malcolm Levitt group in University of Southampton. I hope that current stay will bring many collaborations to our Faculty of Physics which I will always cherish.

And finally, I want to give a big toast to all of my friends, especially for the healthy amount of irony which I found to be useful trait for researcher.

PUBLICATIONS

Publications used in the dissertation

1. Dagys, L. *et al.* Solid-State 1H and 31P NMR and FTIR Spectroscopy Study of Static and Dynamic Structures in Sol-Gel Derived Calcium Hydroxyapatites. *Lith. J. Phys.* **55,** 1–9 (2015).

2 Klimavicius, V., Dagys, L. & Balevicius, V. Subnanoscale Order and Spin Diffusion in Complex Solids through the Processing of Cross-Polarization Kinetics. *J. Phys. Chem. C* **120,** 3542–3549 (2016).

3. Kareiva, S. *et al.* Sol-gel synthesis, phase composition, morphological and structural characterization of Ca10(PO4)6(OH)2: XRD, FTIR, SEM, 3D SEM and solid-state NMR studies. *J. Mol. Struct.* **1119,** 1–11 (2016).

4. Dagys, L., Klimavicius, V. & Balevicius, V. Processing of CP MAS kinetics: Towards NMR crystallography for complex solids. *J. Chem. Phys.* **145**, (2016).

5. Klimavicius, V., Dagys, L., Chizhik, V., Balevicius, V. CP MAS Kinetics Study of Ionic Liquids Confined in Mesoporous Silica : Convergence of Non-Classical. *Appl. Magn. Reson.* **48**, 673–685 (2017).

6. Dagys, L., Klimavicius, V., Gutmann, T., Buntkowsky, G. & Balevicius, V. Quasi-Equilibria and Polarization Transfer Between Adjacent and Remote Spins: 1H − 13C CP MAS Kinetics in Glycine. *J. Phys. Chem. A* **122** (2018).

Other publications

7. Kristinaitytė K. *et al.* NMR and FTIR studies of clustering of water molecules: From low-temperature matrices to nano-structured materials used in innovative medicine, *J. Mol. Liq.* **235,** 1-6 (2016).
8. Kristinaitytė K. *et. al.*, NMR, Raman, and DFT Study of Lyotropic Chromonic Liquid Crystals of Biomedical Interest: Tautomeric Equilibrium and Slow Self-Assembling in Sunset Yellow Aqueous Solutions, *J. Phys. Chem. B* **122,** 3047–3055 (2018).

9. Šimėnas M. *et. al.* Spectroscopic Study of [(CH3)2NH2][Zn(HCOO)3] Hybrid Perovskite Containing Different Nitrogen Isotopes, *J. Phys. Chem. C* **122,** 10284–10292 (2018).

10. Maršalka A. *et. Al.* 1H and 17O NMR study of H-bond dynamics in picolinic acid N-oxide solutions in acetonitrile-h3 and acetonitrile-d3: Novel aspects of old casus, *Chem. Phys.* **24,** 17-22 (2018).

11. Balevicius V. *et. al.* NMR and XRD Study of Hydrogen Bonding in Picolinic Acid N-Oxide in Crystalline State and Solutions: Media and Temperature Effects on Potential Energy Surface, *J. Phys. Chem. A* **122**, 6894–6902 (2018).

Conferences

1. Dagys. L. Quadrupolar interaction in solid-state NMR spectroscopy, Open readings (2014).

2. Klimavičius V., Dagys L. & Balevičius V., Kalcio hidroksi apatitų kietojo kūno BMR tyrimas, Lietuvos Nacionalinė Fizikos Konferencija (2015).

3. Dagys L. *et. al.* BMR relaksacijos tyrimas kietuosiuose NASICON elektrolituose, Lietuvos Nacionalinė Fizikos Konferencija, (2015).

4. Balevicius V., Dagys L. & Klimavicius V. 1H and 31P NMR spectroscopy of dynamic structures in nano-and mesostructured hydroxyapatites, Journal of Materials Sciences and Engineering (2015).

5. Balevicius V., Dagys L. & Klimavicius V. 1H and 31P NMR spectroscopy of dynamic structures in nanomesostructured hydroxyapatites, International Conference and Exhibition on Mesoscopic and Condensed Matter Physics (2015).

6. Balevicius V., Klimavicius V. & Dagys L. Solid state NMR study of materials for innovative medicine: sub-nano structure and dynamics of spin clusters containing hydroxyl groups, XXI International conference on horizons in hydrogen bond research (2015).

7. Dagys L. *et. al.* NMR and FTIR spectroscopy of materials for innovative medicine: sol-gel derived calcium hydroxyapatites, XXII Galyna Puchkovska International School-Seminar Spectroscopy of Molecules and Crystals (2015).

8. Klimavicius V. *et. al.* Solid State NMR study of calcium hydroxyapatites: cut-off averaging of dipolar coupling, spin clusters, CP beating and relaxation effects, Functional Materials and Nanotechnologies (2015).

9. Dagys.L, Klimavicius V. & Balevicius. V. NMR cross-polarization in ammonium dihydrogen phosphate, Open readings (2016).

10. Klimavicius V. *et. al.* Solid State NMR study of complex solids, Pittcon (2016).

11. Kristinaityte K. *et. al.* NMR and FTIR studies of clustering of water molecules: from low-temperature matrices to nano-structured materials used in innovative medicine, PLMMP (2016).

12. Klimavicius V., Dagys L. & Balevicius V. Solid State NMR study of complex solids mimicking biological ones, Ampere Biological Solid-State NMR School (2016).

13. Kristinaitytė K. *et. al.* Spectroscopy of States of Water in Advanced Nano-Structured Materials for In novative Medicine, American Advanced Materials Congress (2016).

14. Dagys L., Klimavicius V. & Balevicius V. Advanced processing of CPMAS kinetics in Ammonium Dihydrogen Phosphate, Spinus (2016)

15. Klimavicius V. *et. al.* Water and other molecular systems in confinements: NMR and FTIR study, Water and Other Partially Ordered Liquids (2017).

16. Klimavcius V., Dagys L. & Balevicius V. XXII Galyna Puchkovska International School-Seminar Sepctroscopy of molecules and Crystals (2017).

17. Dagys L. & Balevicius V. CP MAS Kinetics Study in Glycine Powder Sample, XXII Galyna Puchkovska International School-Seminar Sepctroscopy of molecules and Crystals (2017).

18. Dagys L. & Balevicius V. Kryžminės poliarizacijos kinetikos glicino milteliuose tyrimas, 42-oji Nacionalinė Lietuvos fizikos konferencija (2017).

19. Dagys L. & Balevicius V. NMR cross-polarization transfer in the powdered hema polymer and glycine, AMPERE summer school (2018)

20. Valevičienė N. R. *et. al.* NMR, raman and DFT study of tautomeric equilibrium and slow self-assembling in lyotropic chromonic liquid crystal SSY aqueous solutions, International Symposium on Molecular Spectroscopy (2018).

21. Kristinaityte K. *et. al.* EUROMAR Nantes (2018).

NOTES

Vilniaus universiteto leidykla
Saulėtekio al. 9, LT-10222 Vilnius
El. p. info@leidykla.vu.lt,
www.leidykla.vu.lt
Tiražas 15 egz.